Characterisation of Tomographic Adaptive Optics Performance in Realistic Atmospheric Conditions

OLIVER JAMES DASHWOOD FARLEY

Characterisation of Tomographic Adaptive Optics Performance in Realistic Atmospheric Conditions

Oliver J. D. Farley

A thesis presented for the degree of

Doctor of Philosophy

Centre for Advanced Instrumentation

University of Durham

United Kingdom

September 2020

For Grampie

1930 – 2020

Characterisation of Tomographic Adaptive Optics Performance in Realistic Atmospheric Conditions

Oliver J. D. Farley

Abstract

In ground based astronomy at optical and near infrared wavelengths, the Earth's turbulent atmosphere results in aberration of light before it reaches the telescope. Adaptive optics (AO) allows astronomers to partially correct this aberration, resulting in improved resolution and sensitivity. Tomographic AO techniques have been developed that enable correction over large fractions of the sky, or over a wide field of view. These techniques are employed on current world-leading telescopes and are a key part of the instrumentation for future Extremely Large Telescopes (ELTs). An important piece of information for any tomographic AO system is the vertical distribution (profile) of optical turbulence in the atmosphere. The profile is specific to an observing site and varies temporally on timescales from minutes to seasons.

This thesis is concerned with quantifying the effect of changing profile on tomographic AO by using a large dataset of turbulence profiles from ESO Paranal, Chile. Using a novel clustering method, we extract 18 reference profiles from this dataset. These reference profiles can be used in slow Monte Carlo simulation to give a realistic description of the variability of the profile at Paranal.

We validate these profiles alongside other common reference profiles using a fast Fourier tomographic AO simulation. We find that reference profiles composed of the average of many profiles give worse than expected performance in simulation. Using the same simulation and dataset we also assess the impact of sub-optimal tomographic reconstruction, where the profile is sampled with a small number of layers and is temporally evolving.

Finally we present simulation and on-sky measurements from a SCIDAR turbulence profiler operating on a relatively small 0.5 m aperture. These preliminary results show that a small telescope SCIDAR may be viable for site characterisation and monitoring in the context of ELT-scale tomographic AO.

Supervisors: Richard Wilson , James Osborn and Tim Morris

Acknowledgements

I need to thank my supervisory team of Richard, James and Tim for putting up with my endless stream of bad ideas for three and a half years and sifting out the slightly less bad ones. I would also like to extend thanks to Thierry, Benoît and Carlos at LAM for their help with the simulation work and funding my travel to Marseille several times.

To the author list of Osborn et al. (2018) and everyone else who has operated the Stereo-SCIDAR at Paranal: thank you for putting up with the quirks of the software for long enough to gather the dataset that is the foundation of this thesis. Even if one of you did fall asleep on the job.

I'm indebted to everyone I have shared an office with both past (David, Abi, Amrit, Dougie, Saavi and, occasionally, Mark) and present (Xuewen, Katy, Lai and, occasionally, Vlad) as well as all the other students for making CfAI such an incredible place to do a PhD. Thanks to Matt, Tim B and the rest of the postdocs for stimulating discussions, both academic and non-academic, some even occurring whilst not in the pub. Weekly pizza with John and Abby has also been hugely important in maintaining optimal performance during the write-up.

I'd like to thank my Mum and Dad for their support and regular visits during my PhD. Kimi and Danny, your support was conditional on a continuous supply of seeds, but was also appreciated.

The biggest thanks must go to Lucy. Writing our theses from home under lockdown during a global pandemic has not been an experience I ever want to repeat, but I am so lucky that we've been in this together.

Contents

Declaration

The work in this thesis is based on research carried out at the Centre for Advanced Instrumentation, Department of Physics, University of Durham, England. No part of this thesis has been submitted elsewhere for any other degree or qualification, and it is the sole work of the author unless referenced to the contrary in the text.

Publications

Some of the work presented in this thesis has been published in journals and conference proceedings - the relevant publications are listed below.

O. J. D. Farley, J. Osborn, T. Morris, M. Sarazin, T. Butterley, M. J. Townson, P. Jia, and R. W. Wilson. Representative optical turbulence profiles for ESO Paranal by hierarchical clustering. *MNRAS*, 4037:4030–4037, sep 2018. ISSN 0035-8711. doi: 10.1093/mnras/sty2536. URL `https://academic.oup.com/mnras/advance-article/doi/10.1093/mnras/sty2536/5101457`

O. J. D. Farley, J. Osborn, T. Morris, T. Fusco, B. Neichel, C. Correia, and R. W. Wilson. Identifying optical turbulence profiles for realistic tomographic error in adaptive optics. *MNRAS*, 488(1):213–221, sep 2019. ISSN 0035-8711. doi: 10.1093/mnras/stz1669. URL `https://academic.oup.com/mnras/article/488/1/213/5520823`

O. J. D. Farley, J. Osborn, T. Morris, T. Fusco, B. Neichel, C. Correia, and R. W. Wilson. Limitations imposed by optical turbulence profile structure and evolution on tomographic reconstruction for the ELT. *MNRAS*, 494(2):2773–2784, may 2020. ISSN 0035-8711. doi: 10.1093/mnras/staa795. URL `https://academic.oup.com/mnras/article/494/2/2773/5815102`

List of Figures

List of Tables

Nomenclature

AO adaptive optics

AT auxiliary telescope

ELT extremely large telescope

WFS wavefront sensor

DM deformable mirror

RTC real-time control

LGS laser guide star

PSD power spectral density

CCD charge coupled device

DIMM Differential Image Motion Monitor

SLODAR SLOpe Detection and Ranging

GSM Generalized Seeing Monitor

SCIDAR SCIntillation Detection and Ranging

MASS Multi Aperture Scintillation Sensor

GS guide star

LGS laser guide star

NGS natural guide star

LTAO laser tomographic AO

MOAO multi object AO

MCAO multi-conjugate AO

GLAO ground layer AO

PSF point spread function

SCAO single-conjugate AO

MMSE minimum mean square error

RMS root mean square

FWHM full width at half maximum

E2E end-to-end

pt5m point-5 m

ORM Observatorio Roque de los Muchachos

INT Isaac Newton telescope

WHT William Herschel telescope

SRTC soft real time control

SNR signal-to-noise ratio

NNLS non-negative least squares

TNG Telescopio Nazionale Galileo

RMSE root mean square error

1

Introduction

Astronomy, in its simplest form, may be reduced to the study of light from far away objects that appear very faint and very small, in many cases as unresolved point-like sources. Light from these objects is captured and manipulated in order to measure some properties of the objects. Fundamentally we may measure only two properties: the object's position (astrometry) and brightness (photometry), the latter of which can be measured at different wavelengths of light (spectroscopy). However by fitting physical models to these simple properties we may draw profound conclusions as to the nature of these objects and the universe they inhabit.

Unfortunately, the human eye limits us in this endeavour. With a pupil aperture of less than 1 cm, even those with the best vision may hope to observe a tiny fraction of only the brightest objects in the night sky. Additionally, our wide field of view means we are not able to measure positions of objects in the sky with any great degree of accuracy.

With the advent of telescopes in the 17th century, astronomers were able to augment their eyes with devices that magnified the night sky, allowing precise measurements of celestial objects for the first time. As well as magnification, telescopes allowed observation of fainter objects since the size of the light collecting area could now be larger than the pupil of the eye.

Telescopes with circular apertures are limited by their diameter D in two ways. Firstly, the amount of light collected in an exposure is proportional to the area of the entrance aperture which scales as D^2. Secondly, point sources are imaged through a circular aperture as Airy disks due to diffraction. The angular size of these disks is proportional to λ/D with λ the imaging wavelength (Adams and Hughes, 2018). Hence, a larger diameter telescope allows not only fainter targets to be observed but also improves the diffraction limited angular resolution.

This diffraction limit, however, was difficult to attain as telescope apertures became larger. Firstly, the optical quality of components used had to be as high as possible so as not to induce any unnecessary static aberrations to the light as it passes through the telescope. However, as the science of telescope building progressed and optical quality improved, it became clear that dynamic aberrations induced by the Earth's turbulent atmosphere limited the achievable resolution. Looking at a star through a small telescope, one observes a rapid random motion of the target around a small patch of the sky. Through a larger telescope, the star may also break up into a random speckle pattern. Both Newton (Newton, 1730) and Herschel (Hardy, 1998) remarked on this in the 18th century, observing that on some nights this atmospheric effect was worse than others.

As astronomers pushed the limits of technology in the 19th and 20th centuries, human observers at the focus of the telescope were replaced with photographic plates. This allowed long exposures lasting several hours to be taken and fainter targets to be observed. Over these long exposures the random motion and speckling observed on short timescales average out, producing stellar images that appear as disks with sizes much larger than λ/D. This became known as the "seeing", which became an accepted limitation of astronomy at optical wavelengths. Value began to be placed in siting telescopes in areas of good seeing, such as high altitude mountaintops where the atmosphere was thinner. Despite the seeing problem, advances in sensitivity allowed some very precise measurements to be performed, perhaps most famously the first measurements of the expanding universe using

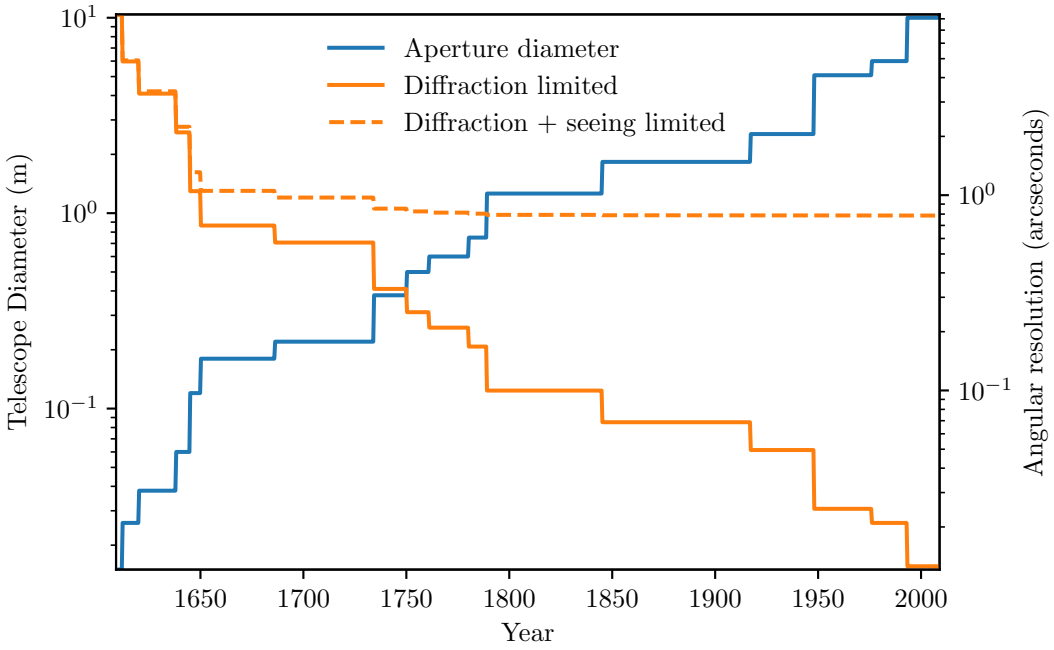

Figure 1.1: Evolution of the diameter (blue) of the world's largest telescope from Galileo's first (1609, 1.5 cm) to the Gran Telescopio Canarias (2009, 10.4 m), with corresponding theoretical advances in angular resolution (orange). Note that in the diffraction + seeing limited calculation only the effect of the turbulent atmosphere with 0.6 arcsecond seeing at an imaging wavelength of $\lambda = 500$ nm is considered. Any other effects such as abberations from poor quality optics are not included. All telescopes apertures are assumed circular.

the 100-inch ($D = 2.5$ m) Hooker telesocpe at Mount Wilson, California (Hubble, 1929). However, the angular resolution was still fundamentally limited by the atmosphere to that of telescopes built 200 years previously. We illustrate in Fig. 1.1 the progression of telescope primary mirror diameter and theoretical angular resolution, both with and without seeing, over the past 400 years. By the 19th century the angular resolution in the diffraction and seeing limit are separated by approximately an order of magnitude. At present, they are separated by almost two orders of magnitude.

1.1 Measuring the turbulent atmosphere

As the seeing became an important aspect of observatory site location, measuring and characterising the turbulence at a site became of great interest. At first the

measurement of the seeing could only occur after an exposure was taken, by analysing the full width at half maximum (FWHM) of the seeing disks in the image. This lead to the now common practice of quoting the seeing in arcseconds, the angular size of the seeing disk on the sky as measured in the focal plane of the telescope. Values in the optical range from less than 0.5 arcseconds in very good seeing to over 2 arcseconds in very bad seeing.

In the 1940s and 1950s a statistical mathematical model of turbulence (Kolmogorov, 1991, translation of the original 1941 paper) and its effect on the propagation of light (Tatarski, 1961) was developed. This theoretical framework allows estimates of atmospheric effects such as the seeing to be extracted from short exposure measurements that effectively freeze the effects of turbulence. This allows the seeing to be measured independently of the long science exposure, potentially using a much smaller and more portable telescope.

Real-time turbulence monitoring and charaterisation was not truly possible until the development of fast readout photoelectric devices such as photomultiplier tubes and later charge coupled devices (CCDs). This fast readout (compared to photographic plates) is essential since many independent short exposure measurements of the turbulent atmosphere must be used to produce an estimate of atmospheric parameters. By taking many thousands of these measurements over the shortest possible time (usually several minutes) it is more likely that the atmosphere does not change significantly during the observation.

Instruments to measure optical turbulence may be broadly separated into two categories. Those that measure stellar image motion (otherwise known as angle-of-arrival) fluctuations such as the Differential Image Motion Monitor (DIMM) (Sarazin and Roddier, 1990), SLOpe Detection and Ranging (SLODAR) (Wilson, 2002) and Generalized Seeing Monitor (GSM) (Ziad et al., 2000), and those that measure scintillation (twinkling) of starlight such as Multi Aperture Scintillation Sensor (MASS) (Kornilov et al., 2003) and SCIntillation Detection and Ranging (SCIDAR) (Vernin and Roddier, 1973).

Iterations of these instruments have been employed to characterise the atmosphere above most current major observing sites (see e.g. Dali Ali et al., 2010; Osborn et al., 2018; Racine and Ellerbroek, 1995; Avila et al., 2005; Vernin and Munoz-Tunon, 1994) as well as future sites (Vernin et al., 2011; Schöck et al., 2009) to ensure the optimal placement of optical telescopes to minimise the effect of the atmopshere. Data from these instruments is also used to monitor the turbulence during observations, and inform the decisions as to which instruments and observations would be most effective given the current atmospheric conditions.

An important distinction of some of these instruments such as SLODAR, MASS and SCIDAR is their ability to not only measure the integrated parameters such as the seeing but also the vertical distribution (profile) of turbulence in the atmosphere. This has become very important for systems attempting to correct for the effect of the atmosphere, as turbulence at high altitude limits their correctable field of view.

1.2 Correcting for the turbulent atmosphere

A concept to compensate for the seeing was first proposed by Babcock (1953). In this method, real-time measurement of the phase aberration of incoming starlight is used to provide correction using a deformable phase correcting element, running in a closed control loop. Whilst the hardware of the time was not capable of this real-time atmospheric measurement and correction, this concept included all of the main elements of the technique now known as adaptive optics (AO): the wavefront sensor (WFS) to measure the phase aberrations, the deformable mirror (DM) to correct the aberrations all controlled by the real-time control (RTC) system. A diagram of a classical closed loop AO system operating on this principle is shown in Fig. 1.2.

Throughout the 1960s, 1970s and 1980s the initial development of AO was lead by the US military, who (amongst other applications) wished to image Soviet satellites

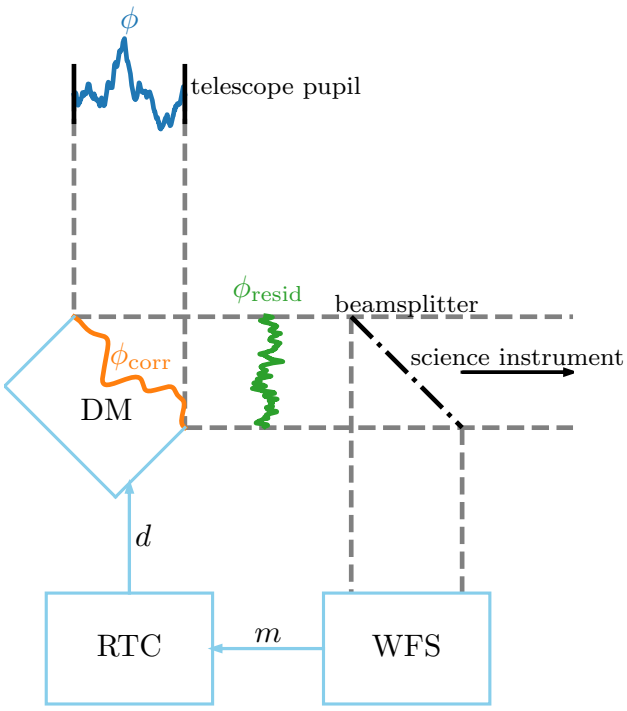

Figure 1.2: Basic layout of a classical closed loop AO system. Input atmospheric phase aberration ϕ is corrected by a correction phase ϕ_{corr} applied by the DM. The resulting beam still exhibits some high order residual aberrations ϕ_{resid}. The beam is split, with some light sent to a WFS which produces a measurement of ϕ_{resid} denoted m. This is sent to the RTC which converts m to DM command voltages d in order to apply the correction ϕ_{corr}. The remaining light from the beamsplitter is sent onwards to the science instrument, usually an imaging system or spectrograph.

from the ground through the Earth's atmospheric turbulence during the Cold War (Hardy, 1998). Since these developments were classified, it was not until the late 80s that the first demonstration of AO for astronomy was realised, with first light for the COME-ON system at the Observatoire de Haute-Provence in 1989 (Rousset et al., 1990).

AO has since become a key tool for astronomers, with its power to unlock the full potential of large 8 m-class telescopes in terms of resolving power and sensistivity. Partially removing the effects of the atmosphere on these large ground based telescopes has enabled them to compete with the increasing number of space telescopes, which for the time being are still limited in scale due to launch costs.

AO systems are currently in use at most major international observatories (see e.g. Esposito et al., 2016, 2012; Neichel et al., 2014; Jovanovic et al., 2016). These systems have enabled, for example, direct observations of stars orbiting the black hole at the centre of our galaxy (Gillessen et al., 2009) and structure in protoplanetary disks around young stars (Benisty et al., 2015).

As of 2020, we are currently in the design and building phase for the next generation extremely large telescopes (ELTs) with aperture diameters of between 25 and 40 m. These will be the first generation of telescopes with AO not only built into downstream instruments attached to the telescope (Neichel et al., 2016; Diolaiti et al., 2018; Herriot et al., 2014) but also an integral part of the telescope itself, e.g. the European ELT adaptive M4 secondary mirror (Vernet et al., 2012). These telescopes, coupled with their AO systems, promise to address a diverse array of science goals, including studies of extra-solar planets, galaxy formation, stellar populations, black holes and the nature of dark matter and dark energy (Skidmore et al., 2015).

1.2.1 Tomographic adaptive optics

Developments in AO since the 1990s have addressed fundamental problems of classical single-conjugate AO (SCAO). Turbulence at altitude results in angular decorrelation along different lines of sight, known as anisoplanatism. This means that AO correction with a single WFS and DM is limited to a small angle (of the order of several arcseconds in the visible) around the target, which leads to the problem of sky coverage. In order to function with minimal noise, the target of the WFS, known as the guide star (GS), must be bright. Therefore if the science target itself is too faint to be used as a GS, a star that is bright enough must be found close by. This limits the number of AO-correctable science targets to those in the vicinity of a bright star. The exact fraction of the sky that is observable with AO correction depends on many factors including the seeing conditions, GS magnitude, observing wavelength and the position of the target with respect to the galactic plane. A

generous estimate is approximately 10% sky coverage in the infrared (Ellerbroek and Tyler, 1998), which severely limits the effectiveness of SCAO.

These problems have been solved by the introduction of lasers as artifical guide stars for the WFS that may be pointed anywhere in the sky. While use of a laser guide star (LGS) theoretically solves the sky coverage problem, use of a single LGS raises its own problems such as focal anisoplanatism and tip-tilt indetermination (Rigaut and Neichel, 2018). Therefore, multiple LGS are usually used in combination with one or more natural guide star (NGS).

By combining measurements of multiple GS along different lines of sight with knowledge of the current optical turbulence profile, the three dimensional volume of turbulence can be tomographically ("in layers") reconstructed. This technique is common to a diverse family of tomographic AO flavours:

- laser tomographic AO (LTAO): turbulence is corrected with nearly full sky coverage but over a narrow field of view using multiple LGS and a single DM (see e.g. Rigaut and Neichel, 2018).
- multi-conjugate AO (MCAO): turbulence is reconstructed across a wide field of view and corrected with multiple DMs optically conjugated to turbulent layers at different altitudes (Beckers, 1988).
- multi object AO (MOAO): as LTAO, but the correction is performed with multiple dedicated DMs for different science target directions potentially over a very wide field (Vidal et al., 2010).
- ground layer AO (GLAO): WFS measurements are averaged over a wide field of view such that only turbulence close to the ground is corrected (Rigaut, 2002).

1.3 Thesis motivation and summary: tomographic adaptive optics and the optical turbulence profile

Instruments employing tomographic AO can already be found in observatories and will form an key part of the planned instrumentation for ELTs. The performance of these systems depends on the optical turbulence profile and therefore characterisation of the profile at a particular site is an important step in characterising AO performance.

This thesis is concerned primarily with the effect of the varying turbulence profile on these tomographic AO systems. More specifically, translating the statistical variability of the turbulence profile into an estimate of the variability of AO performance. This statistical variability of the profile can be sampled by large databases of profiles that span multiple years and many thousands of individual measurements. In this thesis we employ the 2018A database from the Stereo-SCIDAR at ESO Paranal, Chile, consisting of over 10,000 turbulence profiles measured over two years (Osborn et al., 2018).

An important step in the characterisation of the profile is the computation of reference profiles to be used in AO simulations. These simulations tend to be too slow for large databases with thousands of profiles to be used, therefore these reference profiles must describe the variability of the atmosphere in the full dataset with only a few measurements. If these profiles are inaccurate, the performance estimates obtained in simulation could be misleading. In chapter 3, we explore a novel method of extracting reference turbulence profiles from large datasets by employing cluster analysis to classify profiles according to their shape.

Building on this, in chapter 4 we explore how the AO performance estimates obtained from commonly used reference profiles compare to the full dataset. This is accomplished by the use of a fast analytical AO simulation code which enables us to obtain a performance estimate for each of the 10,000+ profiles and compare to

the reference profiles.

In chapter 5 we use the same analytical AO simulation to ascertain the impact that the structure and temporal evolution of the turbulence profile have on the quality of tomographic reconstruction. This is particularly important for next-generation tomographic systems for the ELTs, as they must maintain up to date knowledge of the profile in order to provide optimal correction.

Finally in chapter 6 we investigate in simulation and on-sky the possibility of measuring turbulence profiles using the SCIDAR technique on a relatively small ($D = 0.5$ m) telescope. This would lead to the possibility of a dedicated fully robotic turbulence profiler with the required vertical resolution for ELT-scale tomographic AO systems, which is not obtainable by current robotic site monitoring instruments. Robotic operations would also enable the collection of the large datasets that facilitate the other parts of this work at a small fraction of the cost of a SCIDAR operating on a larger ($D \approx 2$ m) class telescope.

2

Theory

2.1 Atmospheric turbulence

Turbulence refers to the phenomenon of chaotic flow in fluid dynamics. In contrast to laminar flow, in which fluid layers flow past one other smoothly, in turbulent flow fluid layers mix and disrupt one another at their interfaces, resulting in irregular, rapidly changing flow patterns. Whether flow falls into the turbulent or laminar regime is parameterised by the Reynolds number $\mathrm{Re} = vL/\nu$, where v and L are the characteristic velocity and length scale of the flow and ν is the kinematic viscosity of the fluid (Roddier, 1981). The exact value of Re for which laminar flow transitions into turbulent flow depends on the system and fluid in question, but in general very large values of Re are associated with fully developed turbulence.

The Earth's atmosphere is an example of a turbulent fluid: volumes of air of different temperatures and pressures move relative to each other, chaotically mixing at their interfaces. This movement of air is driven ultimately by solar heating of the atmosphere and results in phenomena on a global scale such as Hadley cells and jet streams, as well as more transient and random weather patterns on smaller scales (Hartmann, 2016).

Since the refractive index n of air is a function of its temperature and humidity (Tatarski, 1961; Roddier, 1981), this atmospheric turbulence gives rise to optical turbulence: chaotic refractive index fluctuations that result in the aberration of light propagating through the atmosphere. Typical values of Re for the atmosphere are of the order of 10^6 (Roddier, 1981), falling clearly into the fully devloped turbulence regime. However, it should be noted that there are some cases, such as air moving slowly inside and around telescope domes, in which the turbulence is not fully developed and hence the following theory does not apply.

Since turbulence is chaotic it is very difficult to model analytically, that is to know exactly how n will change spatially or temporally given some set of initial conditions. However, if we assume that the changes in n at any point are stationary random variables, we may derive some statistical parameters of the turbulent atmosphere. Specifically, we define the refractive index at any spatial point $\mathbf{R} = (x, y, z)$

$$n(\mathbf{R}) = 1 + n_1(\mathbf{R}), \tag{2.1}$$

where $n_1(\mathbf{R})$ is a Gaussian random variable with 0 mean.

In the Kolmogorov model of turbulence, energy is injected into the fluid at some largest length scale L_0, the outer scale, and these perturbations cascade down to some smallest length scale l_0, the inner scale. At the inner scale, the energy is dissipated into the fluid by viscous friction. Between these length scales the power spectrum of refractive index fluctuations follows a $-11/3$ power law

$$W_n^{\mathrm{Kol}}(f) = 9.7 \times 10^{-3}\, C_n^2 f^{-11/3}, \tag{2.2}$$

with $f = |(f_x, f_y, f_z)|$ the modulus of the spatial frequency vector and C_n^2 the refractive index structure constant, which defines the extent to which turbulence affects the changes in refractive index and has units of $\mathrm{m}^{-2/3}$ (Roddier, 1981). Note that here f has units of m^{-1}.

A related quantity is the refractive index structure function, which defines the average difference between refractive index values with some spatial separation

$\boldsymbol{\rho} = (\Delta x, \Delta y, \Delta z)$:

$$D_n(\boldsymbol{\rho}) = \langle |n(\mathbf{R}) - n(\mathbf{R} + \boldsymbol{\rho})|^2 \rangle = C_n^2 \rho^{2/3}, \tag{2.3}$$

where $\rho = |\boldsymbol{\rho}|$ (Roddier, 1981) and $\langle\rangle$ denotes an average. The dependence only on the magnitude ρ arises from the assumption of isotropic turbulence in the Kolmogorov model.

Eqs. 2.2 and 2.3 describe the variance in refractive index of any fluid with fully developed turbulence between length scales of $l_0 \ll \rho \ll L_0$, where $\rho \approx 1/f$. If we wish to include length scales larger than L_0 or smaller than l_0, we must modify our power spectrum to account for the saturation of fluctuations at length scales larger than L_0 and the decay of fluctuations at scales smaller than l_0. To account for the outer scale, the most widely used model is a von Kármán spectrum:

$$W_n^{\mathrm{VK}}(f) = 9.7 \times 10^{-3}\, C_n^2 \left[f^2 + \left(\frac{1}{L_0} \right)^2 \right]^{-11/6}. \tag{2.4}$$

For atmospheric turbulence, inner scale values ranging from 1 to 10 mm have been measured (Roddier, 1981), with outer scale values ranging from 10 to over 100 m (Ziad et al., 2004). Modifications to the von Kármán model to account for the inner scale exist however since we are considering telescope apertures of the order of metres, we may neglect the effect of the inner scale. We show examples of $W_n^{\mathrm{Kol}}(f)$ and $W_n^{\mathrm{VK}}(f)$ in Fig. 2.1.

2.1.1 Optical turbulence profiles

In the atmospheric case we must consider that the refractive index structure constant C_n^2 is not constant but is both spatially and temporally varying. In the astronomical (vertical propagation) regime we are concerned with the optical turbulence profile, $C_n^2(h)$. This describes the vertical distribution of turbulence with altitude h and is usually split into three distinct regions.

In the free atmosphere ($h > 1$ km) turbulence is caused by meterological effects such as the jet stream. Although the density of air at these altitudes is lower

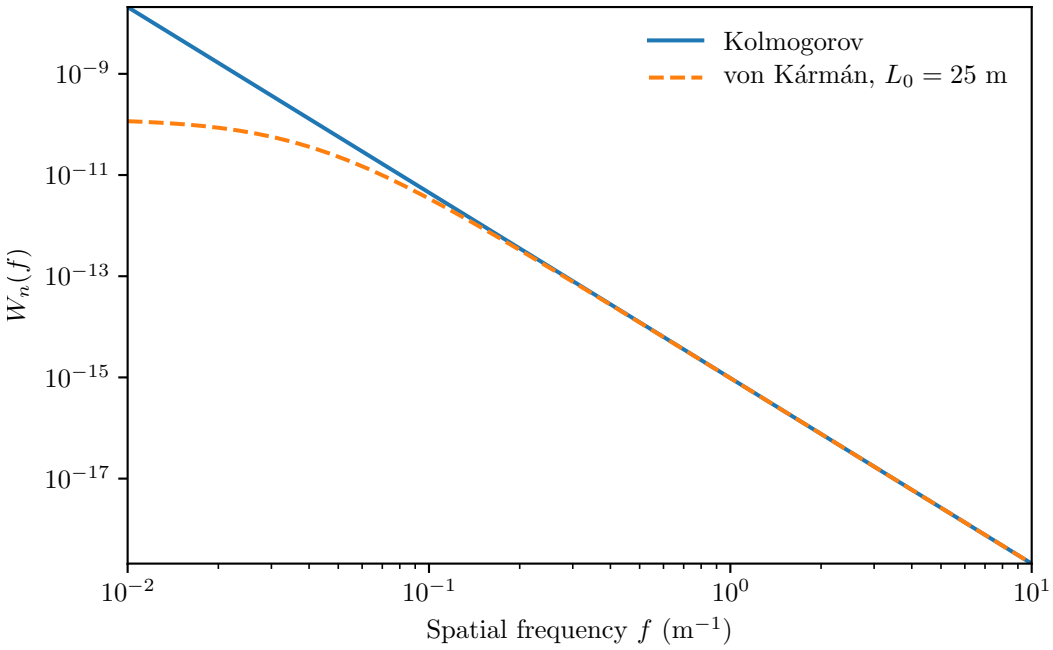

Figure 2.1: Refractive index power spectra for Kolmogorov and von Kármán turbulence. A C_n^2 value of 1×10^{-13} m$^{-2/3}$ is used. The von Kármán spectrum exhibits saturation at $f = 1/L_0$.

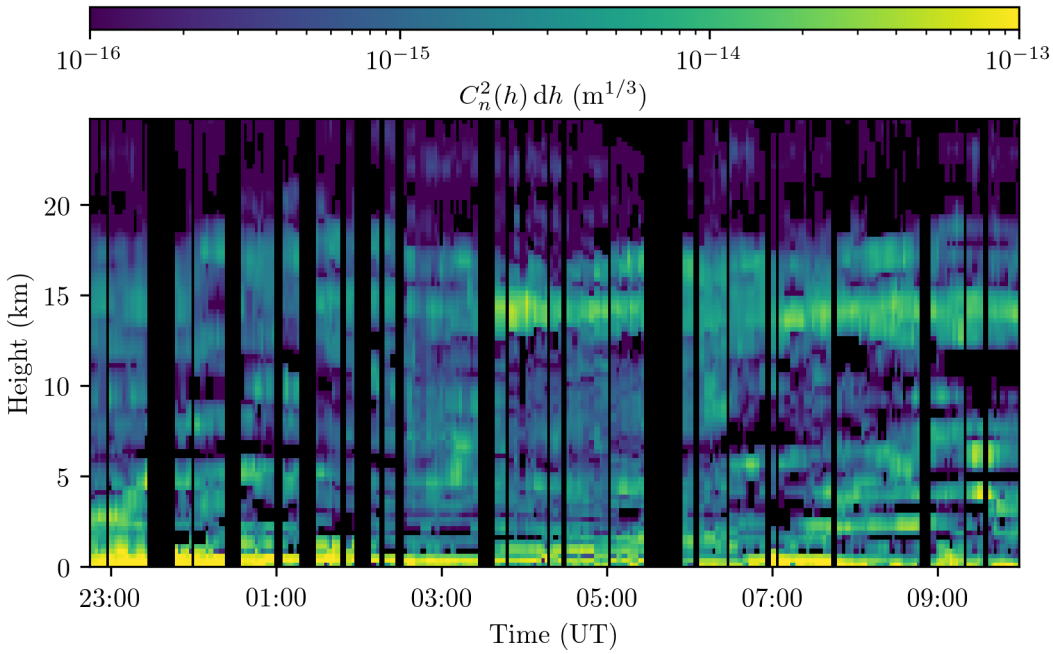

Figure 2.2: Example night of measured optical turbulence profiles from the Stereo-SCIDAR at ESO Paranal, Chile on the night of 6th August 2017. The data has a vertical resolution of 250 m.

than at the ground we observe some of the highest wind speeds, which can result in significant turbulence. As the troposphere transitions to the stratosphere at around 20 km, the turbulence becomes much weaker as the density of air drops further.

Secondly, the ground layer ($h < 1$ km), where the local topography of the Earth's surface (mountains, valleys, etc.) induce turbulence. This turbulence tends to be stronger as the air density is much higher than in the free atmosphere.

Finally, surface layer turbulence refers to turbulence occuring at altitudes of less than 100 m. Usually, surface layer turbulence is associated with man-made structures such as telescope domes or other buildings, and is often characterised by an non-Kolmogorov power spectrum, since the turbulence is not fully developed as it is in the free atmosphere.

The outer scale L_0 of atmospheric turbulence can be of the order of hundreds of metres at its greatest, which is small compared to the vertical propagation distance of light through the turbulent atmosphere (20+ km). Hence the C_n^2 profile in the vertical propagation regime is usually stratified into thin turbulent layers. Particularly in the free atmosphere, the turbulence profile evolves over time as layers become stronger or weaker relative to each other, occasionally vanishing altogether or appearing suddenly (see Fig. 2.2). The level of stratification in the profile can also change over time, and in some cases we observe thicker layers or smooth, continuous distributions of turbulence with altitude. In astronomical AO the atmosphere is usually modelled as discrete infinitesimally thin turbulent layers at different altitudes and therefore the applicability of this model depends on the current profile.

The turbulence profile is a characteristic of a particular astronomical observatory as each aspect, from the surface and ground layers to the free atmosphere, depends on local structures, surface topology and climate respectively. Sites at similar locations tend to share characteristics in the profile, for example at island sites such as Hawaii

and La Palma the turbulence in the ground layer tends to dominate. In areas where there is a strong jet stream such as Chile strong high altitude layers are observed in the range $h = 10$ - 15 km, especially during the winter.

2.2 Light propagation through turbulence

Light propagating through the turbulent atmosphere is described by the complex electric field $\Phi(\mathbf{r}, z) = |\Phi(\mathbf{r}, z)|e^{i\phi(\mathbf{r},z)}$ where $|\Phi(\mathbf{r}, z)|$ and $\phi(\mathbf{r}, z)$ denote the field amplitude and phase. Note we have split the 3 dimensional position vector $\mathbf{R}$ into two dimensional position vector $\mathbf{r} = (x, y)$ and vertical co-ordinate z.

In astronomy, the sources of this light are at such a great distance that the field incident at the top of the atmosphere $z_{\max}$ can be approximated as an infinite plane wave, i.e. both $|\Phi(\mathbf{r}, z_{\max})| = |\Phi|$ and $\phi(\mathbf{r}, z_{\max}) = \phi$ are constant.

After propagating to the telescope aperture at $z = 0$, the light intensity pattern produced at the focal plane of a monochromatic imaging system is proportional to the modulus squared of the Fourier transform of $\Phi(\mathbf{r}, 0)$ according to Fraunhofer diffraction

$$I(\mathbf{x}) \propto |\mathcal{F}[\Phi(\mathbf{r}, 0)P(\mathbf{r})]|^2 \tag{2.5}$$

where $\mathbf{x}$ denotes the position coordinate in the focal plane, $\mathcal{F}$ the Fourier transform and λ the imaging wavelength (Schmidt, 2010). $P(\mathbf{r})$ denotes the pupil function of the imaging system, usually a circle or annulus for a telescope. The response of the imaging system to a point source is known as the point spread function (PSF) and defines the image quality of the system. The image formed of any object, with corresponding incoherent spatial intensity pattern $I_{\text{obj}}(\mathbf{x})$, is given by the convolution with the PSF (Schmidt, 2010)

$$I_{\text{Image}}(\mathbf{x}) = I_{\text{obj}}(\mathbf{x}) \otimes I_{\text{PSF}}(\mathbf{x}). \tag{2.6}$$

In the absence of turbulence, for a circular aperture of diameter D the PSF is an

Airy pattern given by

$$I_{\mathrm{PSF}}(\mathbf{x}) = \left[\frac{\pi D^2}{4} \frac{J_1(\frac{\pi D x}{\lambda l_f})}{\frac{\pi D x}{\lambda l_f}} \right]^2, \tag{2.7}$$

where l_f is the focal length of the imaging system, $x = |\mathbf{x}|$ and J_1 is a Bessel function of the first kind of order 1 (Adams and Hughes, 2018). This is illustrated on the left of Fig. 2.3. The characteristic size of the Airy pattern, defined either by the FWHM or the first zero, is proportional to λ/D. The effect of turbulence can produce much larger PSFs resulting in reduced image quality as well as a loss in sensitivity, since the energy entering the aperture is spread over a wider area on the detector.

2.2.1 Phase aberration

The primary effect of atmospheric turbulence is aberration of the phase, or wavefront, of the incident plane wave. Here, we assume the atmospheric turbulence to be confined to a number of independent thin layers, which is valid in the vertical propagation regime. Note that this assumption is not necessarily required for the following analysis (see e.g. Andrews and Phillips, 2005).

For a single thin layer at altitude $z = h$, we assume the thickness of the layer δh to be small enough such that we can neglect diffraction effects. The total phase aberration caused by the layer is then related only to the integral of refractive index fluctuations along the path of the light

$$\phi(\mathbf{r}, h) = k \int_h^{h+\delta h} n_1(\mathbf{r}, z)\, \mathrm{d}z, \tag{2.8}$$

with $k = 2\pi/\lambda$ the wavevector. (Roddier, 1981). Making the simplifying assumption that the incident plane wave has $|\Phi| = 1$ and $\phi = 0$, then the field at the output of the turbulent layer becomes

$$\Phi(\mathbf{r}, h) = e^{i\phi(\mathbf{r},h)}. \tag{2.9}$$

It can then be shown that if $n_1(\mathbf{r}, z)$ obeys Kolmogorov statistics, the structure function of the phase can be written (Roddier, 1981) as

$$D_\phi(\boldsymbol{\rho}, h) = \langle |\phi(\mathbf{r}, h) - \phi(\mathbf{r} + \boldsymbol{\rho}, h)|^2 \rangle = 2.91 k^2 C_n^2(h) \delta h \rho^{5/3}. \tag{2.10}$$

The astronomical regime allows us to make two more useful assumptions. We may assume that the phase perturbations through a thin layer are small ($\phi(\mathbf{r}, h) \ll 1$) for light passing vertically through the turbulent atmosphere. This assumption holds providing that the telscope is not observing at large zenith angles. Under this assumption, the effect of multiple atmospheric layers at different altitudes h is additive and we may decouple phase fluctuations at the ground $\phi(\mathbf{r}, 0)$ from amplitude fluctuations $|\Phi(r, 0)|$. Secondly, we can make the near-field approximation which is that the phase fluctuations are much larger than the amplidude fluctuations, hence the fluctuations of the overall complex field $\Phi(\mathbf{r}, 0)$ are dominated by the fluctuations in $\phi(\mathbf{r}, 0)$.

Under these two assumptions the power spectrum and structure function of phase aberrations in the telescope pupil ($z = 0$) may be derived for an atmosphere with a continuous turbulence profile $C_n^2(h)$ as

$$W_\phi(f) = 9.7 \times 10^{-3}\, k^2 f^{-11/3} \int_0^\infty C_n^2(h)\, \mathrm{d}h \tag{2.11}$$

$$D_\phi(\boldsymbol{\rho}, 0) \approx 6.88 \left(\frac{\rho}{r_0} \right)^{5/3}. \tag{2.12}$$

Here we have introduced the Fried parameter r_0, defined as

$$r_0 = \left(0.423 k^2 (\cos \gamma)^{-1} \int_0^\infty C_n^2(h)\, \mathrm{d}h \right)^{-3/5}, \tag{2.13}$$

where γ denotes the telescope zenith angle (Roddier, 1981). r_0 defines the aperture diameter over which there is approximately 1 rad^2 of phase variance. For apertures of this size and larger, the size of the PSF is limited by turbulence to λ/r_0 as opposed to λ/D (Fried, 1966). More generally r_0 is a measure of the overall strength of turbulence and is inversely proportional to the integrated $C_n^2(h)$ profile. In the

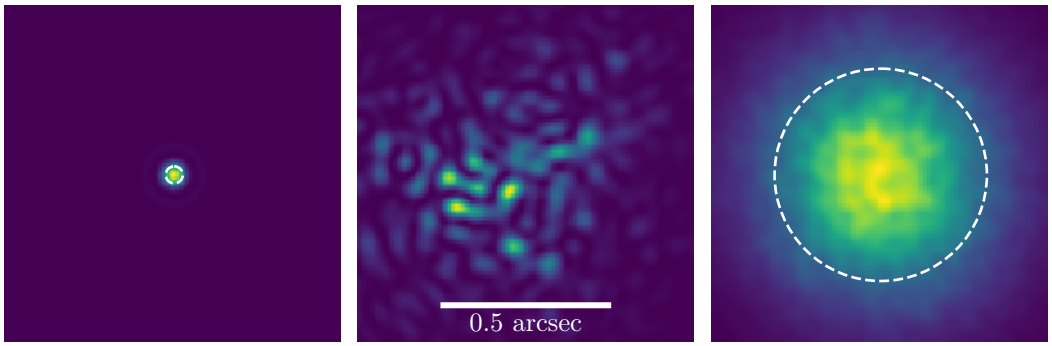

Figure 2.3: Simulated PSFs formed at the focus of an imaging system with a circular aperture of diameter $D = 2\,\mathrm{m}$. *Left*: No turbulence, diffraction limited Airy pattern. *Middle*: Short exposure through turbulence, showing speckle pattern. *Right*: Long exposure composed of the average of 500 short exposures through random turbulence realisations. White dashed circles indicate the theoretical FWHM of the PSFs in the left (λ/D) and right (λ/r_0) panels. Fried parameter $r_0 = 16$ cm and $\lambda = 500$ nm.

visible, values of r_0 measured at night at good observing sites range from less than 10 cm in poor conditions to over 20 cm in good conditions. In Fig. 2.3 we show the effect of the turbulent phase aberration on the PSF in both short and long exposure cases.

In addition to r_0, other atmospheric turbulence parameters may be computed from the turbulence profile $C_n^2(h)$. The angular correlation of turbulence is described by the isoplanatic angle

$$\theta_0 = \left(2.91k^2 \cos(\gamma)^{-8/3} \int_0^\infty C_n^2(h) h^{5/3}\,\mathrm{d}h\right)^{-3/5} = 0.314\frac{r_0}{\bar{h}}, \tag{2.14}$$

where $\bar{h}$ describes the effective turbulence height given by

$$\bar{h} = \left(\frac{\int_0^\infty C_n^2(h) h^{5/3}\,\mathrm{d}h}{\int_0^\infty C_n^2(h)\,\mathrm{d}h}\right)^{3/5}. \tag{2.15}$$

This angle is of the order of several arcseconds in the visible and indicates the correctable field of view for an SCAO system (Fried, 1976).

Finally, the coherence time is defined as

$$\tau_0 = \left(2.91k^2 \cos(\gamma)^{-8/3} \int_0^\infty \frac{C_n^2(h)}{V(h)}\,\mathrm{d}h\right)^{-3/5} = 0.314\frac{r_0}{\bar{V}}, \tag{2.16}$$

where $V(h)$ denotes the wind velocity profile. The effective velocity $\bar{V}$ is defined similarly to Eq. 2.15:

$$\bar{V} = \left(\frac{\int_0^\infty C_n^2(h) V(h)^{5/3} \, \mathrm{d}h}{\int_0^\infty C_n^2(h) \, \mathrm{d}h} \right). \tag{2.17}$$

The coherence time describes the temporal correlation of turbulence and is usually of the order of several milliseconds in the visible (Roddier, 1981). This constrains the update rate of the AO loop since it must operate on similar timescales to ensure that the turbulence measured by the WFS is the same as the turbulence corrected by the DM.

Since r_0, θ_0 and τ_0 depend on wavelength as $\lambda^{6/5}$, the effects of turbulence are worse at shorter wavelengths. Throughout we will use a standard wavelength of $\lambda = 500$ nm when calculating these parameters.

2.2.2 Amplitude aberration

Although according to the near-field approximation fluctuations of the complex amplitude $|\Phi(\mathbf{r}, 0)|$ in the telescope pupil are small, they still produce a measurable effect. As light passes though a high altitude phase aberration $\phi(\mathbf{r}, h)$ and propagates downwards, it is locally focussed and defocussed causing a characteristic "flying shadow" pattern at the ground. Viewed through an aperture, these patterns are spatially averaged over the pupil and result in overall intensity variation of the image in the focal plane. This effect is known as scintillation, or twinkling.

Since we are in the near-field regime, the propagation to the ground may be described by convolution of the output of the turbulent layer $e^{i\phi_h(r)}$ with the Fresnel kernel (Schmidt, 2010)

$$\Phi(\mathbf{r}, 0) = e^{i\phi(\mathbf{r},h)} \otimes \frac{e^{ikh}}{i\lambda h} \exp\left(\frac{ik}{2h} r^2 \right). \tag{2.18}$$

We are usually concerned with fluctuations in the intensity or irradiance $I(\mathbf{r}, 0) = |\Phi(\mathbf{r}, 0)|^2$ since this is what we are able to measure with an optical device. As

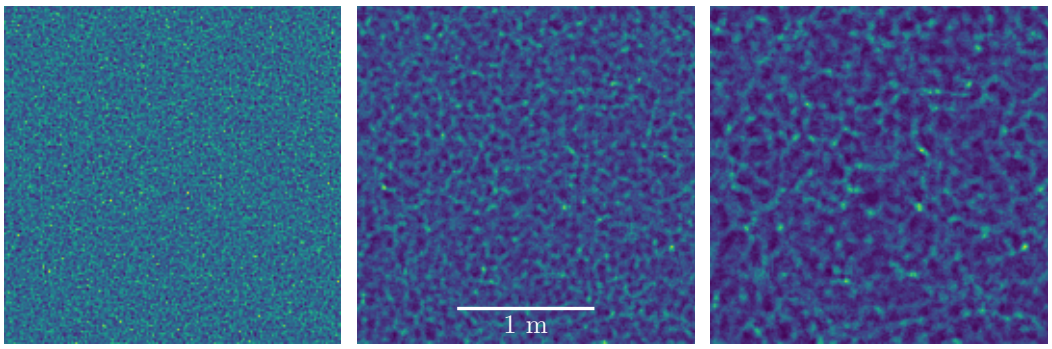

Figure 2.4: Simulated intensity aberration patterns produced at ground level by a single turbulent layer located (from left to right) at $h = 1$ km, $h = 5$ km and $h = 10$ km. The turbulent layer has $r_0 = 16$ cm and the propagation is performed at $\lambda = 500$ nm.

for phase aberrations, under the small perturbations approximation the effects of multiple turbulent layers are additive, and we may derive a power spectrum for intensity fluctuations at the ground for Kolmogorov turbulence as an integral over the C_n^2 profile (Roddier, 1981; Tokovinin, 2002)

$$W_I(f) = 3.9 \times 10^{-2} k^2 f^{-11/3} \int_0^\infty C_n^2(h) \sin^2(\pi \lambda h f^2) \, \mathrm{d}h. \tag{2.19}$$

Unlike Eq. 2.11, the $\sin^2(\pi \lambda h f^2)$ factor means that for intensity variations to be produced, the layer must be at some altitude $h > 0$.

From Eq. 2.19 we may derive the spatial covariance of this intensity pattern, via the Wiener-Khinchin theorem (Roddier, 1981) which states that autocovariance and power spectra are related by a Fourier transform $B(r) = \mathcal{F}^{-1}[W(f)]$:

$$B_I(r) = 3.9 \times 10^{-2} 2\pi k^2 \int_0^\infty C_n^2(h) \int_0^\infty f^{-8/3} \sin^2(\pi \lambda h f^2) J_0(2\pi r f) \, \mathrm{d}f \mathrm{d}h \tag{2.20}$$

where J_0 is a Bessel function of the first kind order 0 (Shepherd et al., 2014). The spatial scale of the intensity variations and hence the width of $B_I(r)$ for a given layer is given by the Fresnel radius

$$r_F = \sqrt{\lambda h}\,, \tag{2.21}$$

therefore layers at higher altitudes produce an intensity pattern at larger scales (Tatarski, 1961), as illustrated in Fig. 2.4.

2.3 Adaptive optics

2.3.1 Wavefront control

The basic AO control loop as illustrated in Fig. 1.2 consists of three operations. Firstly, the WFS measures the phase aberration on the telescope pupil ϕ (note for clarity we drop the coordinate $\mathbf{r}$ here). This measured phase will be averaged over the integration time of the WFS, which must be less than τ_0 to avoid significant error. Next, the RTC processes this measurement into a correction signal d to be applied to the DM, resulting in a corrective phase ϕ_{corr} applied to the wavefront. The aim is to flatten the wavefront and as much as possible return it to a plane wave with constant phase ϕ.

The WFS phase measurement vector m may be written

$$m = \hat{M}\phi + b, \tag{2.22}$$

where $\hat{M}$ is a linear operator describing the measurement of phase with a particular WFS type and b represents additive random noise (Rigaut et al., 1998). Many variations of WFS exist, but the two in most common usage currently are Shack-Hartmann (see e.g. Hardy, 1998) and Pyramid (Ragazzoni, 1996) sensors. Shack-Hartmann sensors operate by optically splitting the telescope aperture into an array of smaller subapertures and measuring the local wavefront gradient across each subaperture. Smaller subapertures allow higher order aberrations of the phase to be measured. Pyramid sensors utilise a modulated four sided prism in the focal plane and reimage the four resulting pupil images onto a detector. The wavefront can be measured from these pupil images which will exhibit different intensity patterns depending on the phase aberration.

In the RTC system, the measured wavefront signal m is converted to a correction signal to be applied to the DM, which we denote d. This computation may be

written as another matrix multiplication

$$d = \hat{W}m \tag{2.23}$$

where $\hat{W}$ denotes the the reconstructor matrix. The DM usually splits the aperture into zones, with actuators locally deforming the surface to apply a phase correction (see e.g. Hardy, 1998). d describes the voltages applied to each actuator in order to achieve a phase correction ϕ_{corr}.

In classical SCAO this matrix may be computed by the inverse of the interaction matrix, which may be obtained during calibration by measuring WFS signals m as a result of moving each DM actuator. In this situation $\hat{W}$ is sometimes referred to as the command matrix.

The above vectors and matrices may be defined in the space of pure WFS measurements m and DM actuator commands d, in which case the reconstructor $\hat{W}$ will be of dimension (number of WFS measurements $\times$ number of DM commands). It is also common to define the problem in terms of some orthornomal basis such as Zernike polynomials (Noll, 1976), where $\hat{W}$ will have dimension (number of measured modes $\times$ number of corrected modes). In either case, it is clear that as apertures become larger and the desired level of correction increases (both requiring a greater number of subapertures or modes), the size of the computation in Eq. 2.23 rapidly increases. This is a fundamendal challenge of designing RTC systems at ELT scales (see e.g. Jenkins et al., 2018).

2.3.2 Performance metrics

The residual wavefront after AO correction is given by

$$\phi_{\text{resid}} = \phi - \phi_{\text{corr}}. \tag{2.24}$$

It is aberrations in this residual phase that determine the image quality in the focal plane. Thus a commonly used metric is the residual wavefront error σ_ϕ, ususally

defined as the root mean square (RMS) variance of $\phi_{\text{resid}}(r)$ averaged across the aperture

$$\sigma_\phi = \sqrt{\langle(\phi_{\text{resid}} - \langle\phi_{\text{resid}}\rangle)^2\rangle}, \tag{2.25}$$

where $\langle\rangle$ here denotes averaging over the aperture. We subtract the constant aperture averaged phase $\langle\phi_{\text{resid}}\rangle$ or piston term since this does not contribute to image quality. Wavefront variance σ_ϕ^2 is usually given in units of rad^2 whereas RMS wavefront error σ_ϕ is generally given in units of nm.

A metric that may be calculated from focal plane images of point sources is the Strehl ratio S, defined as

$$S = \frac{I_{\text{max}}}{I_0}\,, \tag{2.26}$$

where I_{max} denotes the maximum intensity of the aberrated PSF and I_0 is the theoretical maximum intensity of a diffraction limited PSF as defined in Eq. 2.7. Hence the maximum value of S is 1 which indicates the diffraction limit, with any aberration to the phase resulting in a reduction of this value. The Strehl ratio may be related to the wavefront error by the Marechal approximation

$$S \approx \exp\left(-\sigma_\phi^2\right), \tag{2.27}$$

which holds for wavefront variances smaller than around 1 rad^2 (Ross, 2009).

2.3.3 Tomography

For tomographic AO, the computation of $\hat{W}$ is more complex, since we are combining measurements from multiple WFS and, in the case of MOAO and MCAO, projecting the correction onto multiple DMs. For the purposes of this thesis we are concerned only with the tomographic reconstruction step, i.e. the reconstruction of L turbulent layers given a set of N WFS measurements $\mathbf{m} = (m_1(\alpha_1), m_2(\alpha_2), ..., m_N(\alpha_N))$ where α_i denotes the direction of GS i. We will also focus only on one form of tomographic reconstructor, the minimum mean square error (MMSE) estimator (Fusco et al., 2001).

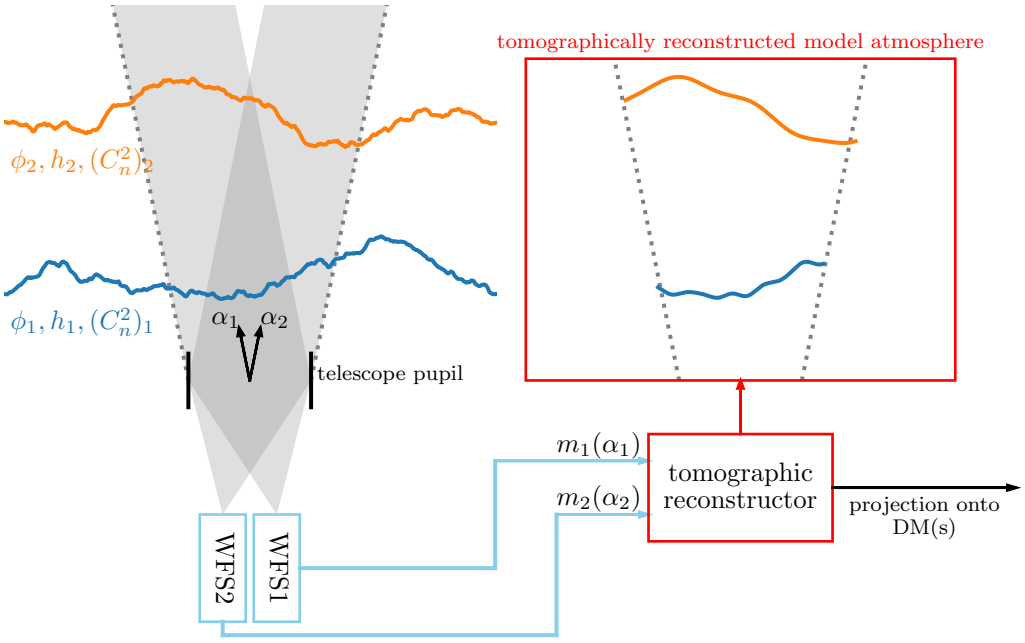

Figure 2.5: 1D representation of tomographic reconstruction for the simple case of $N = 2$ guide stars and reconstructing $L = 2$ turbulent layers. The two WFSs sample turbulence from the two atmospheric layers in directions α_1 and α_2 according to the grey shaded areas. The corresponding measurements $m_1(\alpha_1)$ and $m_2(\alpha_2)$ are fed into the tomographic algorithm, which reconstructs the turbulent layers across the field of view (indicated by the dotted grey lines). This turbulent volume may then be projected onto one or several DMs to perform correction.

Instead of treating the phase aberration only at the telescope pupil (ϕ), we now consider an atmosphere with L turbulent layers at altitudes $h_1, h_2, ..., h_L$ with respective strengths $(C_n^2)_1, (C_n^2)_2, ..., (C_n^2)_L$. We denote the phase aberration at each layer $\boldsymbol{\varphi} = (\phi_1, \phi_2, ..., \phi_L)$. Each ϕ_i is decomposed onto an orthonormal basis of N_{modes} modes, so the phase aberrations are described by a vector of N_{modes} basis coefficients per layer.

Since we are now considering a model atmosphere with L turbulent layers, our WFS measurement model from Eq. 2.22 must also be slightly modified

$$\mathbf{m} = \hat{M}\hat{P}_{\boldsymbol{\alpha}}^{L}\boldsymbol{\varphi} + \mathbf{b} \tag{2.28}$$

where $P_{\boldsymbol{\alpha}}^{L}$ is a projection operator, performing the addition of the relevant spatial regions of $\boldsymbol{\varphi}$ that lie along the lines of sight $\boldsymbol{\alpha} = (\alpha_1, \alpha_2, ..., \alpha_L)$ (Neichel et al., 2009; Fusco et al., 1999).

An MMSE reconstructor minimses the squared residual between the tomographically reconstructed phase vector

$$\boldsymbol{\varphi}_{\text{recon}} = \hat{W}_{\text{MMSE}}\mathbf{m}\,, \tag{2.29}$$

and the true phase $\boldsymbol{\varphi}$, i.e.

$$\sigma^2_{\text{tomo}} = |\boldsymbol{\varphi} - \boldsymbol{\varphi}_{\text{recon}}|^2, \tag{2.30}$$

where we have defined this residual as the tomographic error σ^2_{tomo}.

The optimal minimisation is given by

$$\hat{W}_{\text{MMSE}} = \hat{C}_{\boldsymbol{\varphi}_n}(\hat{M}\hat{P}^L_{\boldsymbol{\alpha}})^T[\hat{M}\hat{P}^L_{\boldsymbol{\alpha}}\hat{C}_{\boldsymbol{\varphi}_n}(\hat{M}\hat{P}^L_{\boldsymbol{\alpha}})^T + \hat{C}_{\mathbf{b}}]^{-1} \tag{2.31}$$

with $\hat{C}_{\boldsymbol{\varphi}_n}$ and $\hat{C}_{\mathbf{b}}$ the turbulence and WFS noise covariance matrices respectively (Fusco et al., 2001; Neichel et al., 2009). These matrices provide *a priori* information about the turbulence and noise statistics. We are particularly interested in $\hat{C}_{\varphi_n}$, which is a block diagonal matrix of dimension $(LN_{\text{modes}}) \times (LN_{\text{modes}})$ defined as

$$\hat{C}_{\varphi_n} = \begin{pmatrix} \lambda_1 C_\phi & 0 & \cdots & 0 \\ 0 & \lambda_2 C_\phi & \cdots & 0 \\ \vdots & \vdots & \ddots & \vdots \\ 0 & 0 & \cdots & \lambda_L C_\phi \end{pmatrix} \tag{2.32}$$

where C_ϕ represents the turbulent phase covariance matrix expressed in the basis of choice which may be derived from the Kolmogorov theory (see e.g. Noll, 1976, for this derivation with Zernike modes). The $\lambda_i = (C_n^2)_i / \sum_i (C_n^2)_i$ represent the turbulent fraction in each reconstruction layer (Neichel et al., 2009). It is here that good knowledge of the turbulence profile $C_n^2(h)$ becomes important since it is required in order to optimise the tomographic reconstruction and therefore minimise the tomographic error, which may be a significant portion of the total wavefront error for a tomographic system (see e.g. Gilles et al., 2008).

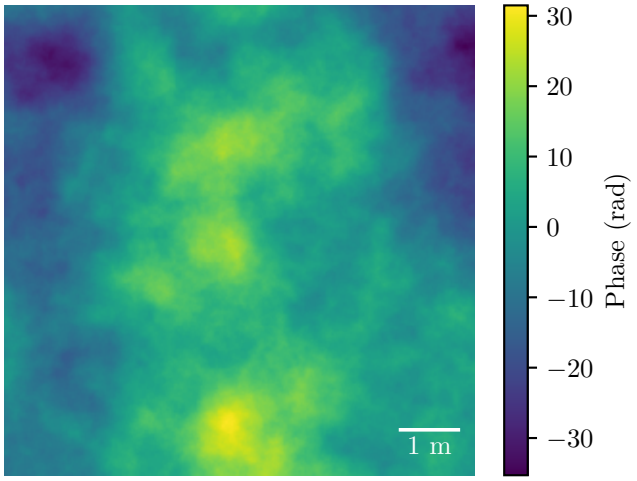

Figure 2.6: Example of a random phase screen. This screen was generated with Kolmogorov statistics and $r_0 = 0.16$ m. Many thousands of such screens are used to model the turbulent atmosphere in Monte Carlo AO simulations.

2.3.4 Monte Carlo simulation

In Monte Carlo simulation, many random repeats are performed and the results obtained by statistically analysing the outputs. This is particularly suited for AO where we have a theory that describes the statistics of random atmospheric turbulence.

The fundamental process of Monte Carlo AO simulation is the generation and translation of two dimensional turbulent phase screens across a simulated aperture. These screens, which describe the phase aberration of each turbulent layer, are randomly generated with a power spectrum described by Eq. 2.2 or Eq. 2.4. Under the Taylor frozen flow hypothesis (Taylor, 1938), the turbulent atmosphere may be modelled by translating these screens according to the wind speed and direction for each layer. An example of a randomly generated phase screen is shown in Fig. 2.6.

All components of the AO system itself are then simulated to a high degree of accuracy, with the wavefront reconstruction and correction computed and applied to the input phase. One may then directly compute the long or short exposure PSF and measure performance. Real world effects such as noise, optical misalignments and incorrect calibration may also be accounted for and their effect on the overall

performance quantified. Monte Carlo simulation is therefore sometimes referred to as end-to-end (E2E) since it may include all aspects of the system from the atmosphere to the science camera. The high fidelity model of the real AO system created by these simulations means that they are the primary choice when performing simulations for instrument design.

A downside of this high fidelity is a large demand on processing power. For atmospheric statistics to converge, many realisations of independent phase screens must be used. Even with fast low level programming languages and a high degree of parallellisation, at ELT scales these simulations require computing times of the order of hours to produce results for as little as several seconds of simulation time. This severely limits the user's ability to perform many simulations with different parameters, such as different turbulence profiles.

Current Monte Carlo AO simulations include SOAPY (Reeves, 2016), OOMAO (Conan and Correia, 2014), YAO (Rigaut and van Dam, 2013), DASP (Basden et al., 2007), COMPASS (Gratadour et al., 2014), and OCTOPUS (Le Louarn et al., 2004).

2.3.5 Fourier simulation

A solution to the atmospheric convergence problem that makes Monte Carlo simulation so slow is to perform the entire simulation in the Fourier domain. The atmospheric turbulence has well defined power spectra defined by e.g. Eqs. 2.2 or 2.4. By deriving linear Fourier domain operators for each component of the AO system (WFSs, DMs etc.), we can obtain the power spectrum of the residual phase by simply multiplying the input atmospheric power spectrum by these operators (Jolissaint et al., 2006). Similarly, we may derive tomographic reconstructors as per Eq. 2.31, replacing the turbulence and noise covariance matrices with turbulence and noise power spectra (Neichel et al., 2009). Integrating the residual phase power spectrum gives us the wavefront error σ_ϕ^2 directly and the theoretical long

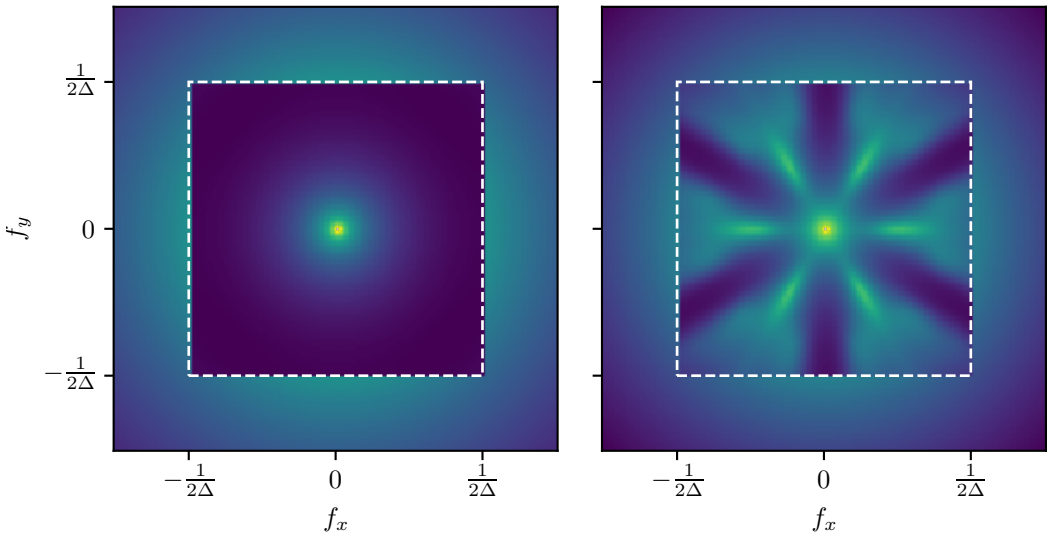

Figure 2.7: Analytically computed power spectra of residual phase after AO correction. Both are plotted using a logarithmic colour scale. *Left*: On-axis SCAO correction, including fitting error and WFS noise. *Right*: On-axis LTAO correction including tomographic error, fitting error and WFS noise for an ELT scale 6 LGS system with an asterism diameter of 1 arcminute. The AO corrected zone is indicated by the dashed white box. This zone is square, as these power spectra are calculated assuming zonal correction by square DM subapertures with pitch Δ. The residual wavefront error may be obtained from these power spectra by integration over the plane.

exposure AO corrected PSF may then be computed if required (Jolissaint et al., 2006).

Examples of residual phase power spectra are shown in Fig. 2.7. At high frequencies outside the AO correction zone the atmospheric power spectrum is seen with characteristic $f^{-11/3}$ slope. In the SCAO case we observe only a contribution at lower frequencies from the WFS noise. For the LTAO case there is more structure within the correction zone: modes along the directions of the LGS the turbulence are effectively sensed and corrected whereas for other modes the correction is not as good.

Since the system is represented in the Fourier domain, many effects that are modelled in Monte Carlo simulation are not possible to model in a Fourier simulation. Most importantly, since the Fourier filters are shift-invariant we cannot model

aperture edge effects and must effectively assume an infinite aperture size.

Analytical modelling therefore allows computation only of a first order estimate of AO performance. However, since computation times are drastically reduced from hours to seconds at ELT scales, it has uses in the preliminary stages of instrument design for fast scanning of parameter spaces. It has also been shown by comparison to E2E simulation at ELT scales that a Fourier model gives similar results, providing that the field of view is smaller than 10 arcminutes.

Analytical AO simulation implementations include PAOLA (Jolissaint et al., 2006) and the Fourier code developed at LAM (Neichel et al., 2009). Throughout this thesis we employ an IDL implementation of the LAM Fourier code.

2.3.6 Error terms

In the particular case of SCAO, many of the residual phase power spectrum integrations may be performed analytically, leading to direct expressions for the wavefront error arising from different sources. Assuming these error terms are independent, we can write the total residual wavefront error as

$$\sigma_\phi^2 = \sigma_{\text{fitting}}^2 + \sigma_{\text{aniso}}^2 + \sigma_{\text{temporal}}^2 + \dots, \tag{2.33}$$

where we have shown here only the DM fitting error $\sigma_{\text{fitting}}^2$, anisoplanatic error σ_{aniso}^2 and temporal error $\sigma_{\text{temporal}}^2$, which are associated with the turbulence profile.

Through analysis of these error terms in the Fourier domain, and performing the resulting integrals analytically, these error terms may be modelled as

$$\sigma_{\text{fitting}}^2 \propto \left(\frac{\Delta}{r_0}\right)^{5/3}, \tag{2.34}$$

$$\sigma_{\text{aniso}}^2 \propto \left(\frac{\theta}{\theta_0}\right)^{5/3}, \tag{2.35}$$

$$\sigma_{\text{temporal}}^2 \propto \left(\frac{\tau}{\tau_0}\right)^{5/3}, \tag{2.36}$$

with Δ the DM actuator pitch, θ the angular distance between the GS direction and the science target direction in the field of view and τ the AO loop delay (Rigaut et al., 1998; Fried, 1982, 1990).

Therefore the parameters r_0, θ_0 and τ_0 are of interest to AO, since they are simple simple weighted integrals of the C_n^2 profile and are directly convertible into an estimate of SCAO performance in given atmospheric conditions.

For a tomographic AO system, the error terms are slightly different,

$$\sigma_\phi^2 = \sigma_{\text{tomo}}^2 + \sigma_{\text{gen. fitting}}^2 + \sigma_{\text{fitting}}^2 + \sigma_{\text{temporal}}^2 + \dots, \tag{2.37}$$

where $\sigma_{\text{gen. fitting}}^2$ denotes the generalised fitting error and σ_{tomo}^2 is the tomographic error. As previously defined in Eq. 2.30, the tomographic error arises from the inability of the tomographic reconstructor to perfectly reconstruct the three dimensional phase volume from the WFS measurements, and may vary across the field of view depending on the position of the guide stars and the turbulence profile. Note that this replaces the anisoplanatic error term from the SCAO case.

The generalised fitting is important in MCAO and arises from the inability of a DM to correct phase distortions over a wide field of view unless the turbulent layer and DM are conjugate to the same plane. If the tomographically reconstructed turbulent layer and DM are conjugate to different planes, the layer must be projected onto the DM, effectively averaging phase distortions in different directions and inducing generalised fitting error (Rigaut et al., 2000). In cases where i) there is a DM conjugated to each turbulent layer in the reconstructor or ii) correction is only required in a single direction (e.g. LTAO), then $\sigma_{\text{gen. fitting}}^2 = 0$.

The tomographic AO specific error terms σ_{tomo}^2 and $\sigma_{\text{gen. fitting}}^2$ may not be described by simple expressions involving atmospheric parameters as for Eqs. 2.34, 2.35 and 2.36. Hence a full Fourier analysis or E2E Monte Carlo simulation must be used to obtain performance estimates. It is therefore difficult to calculate how changes in the turbulence profile affect changes in tomographic AO performance, which is the primary motivation of this thesis.

The overall performance of a tomographic AO system will depend on the magnitude of the different error terms in Eq. 2.37. In chapters 4 and 5 we will focus on the tomographic error since it will be common to all tomographic systems. Preliminary error budgets for ELT scale systems with relatively narrow LGS asterisms have shown that the tomographic error, classical fitting error and generalised fitting (where applicable) tend to be of similar magnitude (Trancho et al., 2012; Gilles et al., 2008) and constitute a significant portion of the total error.

3

Representative profiles from large datasets via cluster analysis

Note: this chapter is an adaptation of Farley et al. (2018)

3.1 Introduction

Since the optical turbulence profile is deemed important during site characterisation studies, turbulence profiling instruments produce many measurements of the profile to fully characterise the atmosphere and obtain robust statistics regarding its variability. However as discussed in section 2.3.4, design simulations of tomographic AO tend to be Monte Carlo in nature and require long simulation times and many repeats of the simulation to produce results for a single set of atmospheric conditions. It is therefore not feasible to run simulations on many thousands of turbulence profiles to fully characterise AO performance for a particular site. Thus the large dataset of measured turbulence profiles must be reduced to a small set that is in some way representative of the dataset as a whole.

If the turbulence profile at a site were to show very little temporal variation, this task is relatively simple; the average integrated $C_n^2(h)$ values in each altitude bin for example would give a good approximation of the profile at all times. However for most observing sites the profile varies greatly on timescales from minutes to seasons. At different times the profile will show strong layers at different altitudes and by averaging we smooth out these features that are only present in a subset of the data. The resulting profile may look completely unlike any measured profile and is therefore not representative of the dataset. An instrument optimised to such a profile may not perform as expected under real world conditions.

Here we put forward a method of obtaining a set of representative turbulence profiles from a large dataset by employing hierarchical clustering to provide a quantitative classification of profiles. By grouping the data according to this classification we separate profiles with different structure. We may then extract a single profile from each group, resulting in a small set of profiles that are more representative of the dataset as a whole.

An example of a site with large variation in the structure of the turbulence profile is ESO Paranal, Chile. A 20 month long campaign using a Stereo-SCIDAR instrument (Shepherd et al., 2014) mounted on one of the auxiliary telescopes (ATs) has yielded a set of over ten thousand high resolution (250 m altitude bins) measurements of the turbulence profile at Paranal (Osborn et al., 2018). We apply the clustering method to this dataset to obtain a small set of turbulence profiles. By ensuring the clustered profiles represent the dataset in terms of integrated atmospheric parameters we validate them in an atmospheric sense without reference to any particular AO system.

We can make the assumption that the free atmosphere turbulence at Paranal is similar to Cerro Armazones, the site of the planned European ELT, since they are separated by only around 20 km distance and by around 500 m in altitude. As such this work is relevant to both sites.

In section 3.2 we present an overview of hierarchical clustering and our method of extracting a small set of turbulence profiles from a large dataset. In section 3.3 we apply this method to the Stereo-SCIDAR dataset from Paranal to obtain a small set of clustered profiles, with comparisons to other turbulence profiles for Paranal. Conclusions are in section 3.4.

3.2 Clustering

Cluster analysis allows underlying structure in large datasets to be ascertained by partitioning the data into subsets, known as clusters. There are many different ways to perform clustering on a dataset but here we focus on hierarchical clustering (Everitt et al., 2011, chapter 4). We settle on this particular variety of clustering for two reasons. Firstly, it allows easy switching and comparison of distance metrics, specifically non-euclidean distance metrics that are particularly effective in this case. Secondly, the clustering can be visualised by the use of a dendrogram (see Fig. 3.1). At the lowest level we have each element in the dataset represented by a vertical line, known as leaves. As we move up the dendrogram to larger distances elements are merged into clusters represented by the joining of two vertical lines into one. To define a certain number of clusters, we cut the dendrogram horizontally at a particular distance and count how many vertical lines (clusters) are intersected. In our case the dendrogram is most useful as a check that the clustering produces sensible results, especially when coupled with the dataset ordered according to the leaves as also displayed in Fig. 3.1.

3.2.1 Distance Metrics

The input to a hierarchical clustering algorithm is the distance matrix D. For a dataset of n observations of p variables (in this case $C_n^2(h)\,\mathrm{d}h$ in p altitude bins), D is an $n \times n$ matrix whose components δ_{ij} represent the pairwise distances between all the observations using a given metric. The choice of the distance metric can

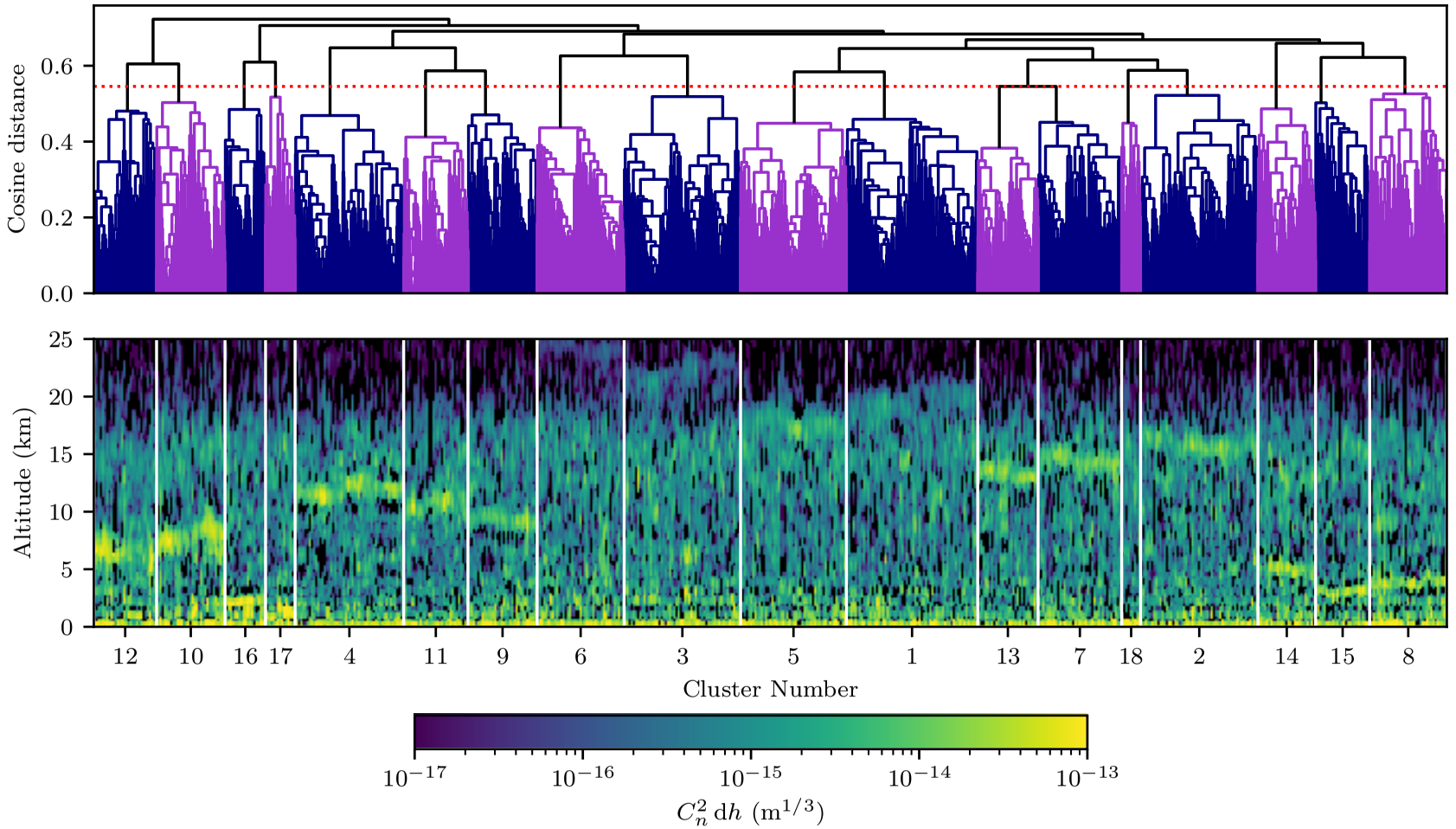

Figure 3.1: *Upper*: Dendrogram representing average linkage agglomerative hierarchical clustering of the ESO Paranal Stereo-SCIDAR dataset using the cosine distance metric. Branches below a cutoff distance of 0.55 (indicated by the dashed red line) are coloured alternately to indicate 18 clusters. *Lower*: The turbulence profiles in the dataset, ordered according to the leaves of the dendrogram, with the partitioning into 18 clusters indicated by verical white lines. Each cluster is assigned a number according to its size, with 1 being the largest cluster and 18 the smallest.

have a large impact on the resulting clustering. The most commonly used metric is the euclidean distance:

$$\delta_{ij}^{\text{euc}} = \sqrt{\sum_{k=1}^{p} (\mathbf{x}_{ik} - \mathbf{x}_{jk})^2}, \tag{3.1}$$

where $\mathbf{x}_{ik}$ and $\mathbf{x}_{jk}$ represent the kth variables in two measurements of the turbulence profile $\mathbf{x}_i$ and $\mathbf{x}_j$ (Everitt et al., 2011, p. 49). This metric forms the basis of popular clustering algorithms such as K-means (Hartigan, 1975). However for profiling data spanning several orders of magnitude in $C_n^2(h)$ the euclidean distance proves to be very sensitive to outliers. As a result, clusters produced using the euclidean distance tend to contain a small number of extreme but very similar profiles, while assigning all other profiles (often over half the dataset) to a single large cluster.

As an alternative, we found the cosine or angular distance to produce favourable results, defined as the normalised dot product

$$\delta_{ij}^{\cos} = 1 - \frac{\mathbf{x}_i \cdot \mathbf{x}_j}{\|\mathbf{x}_i\|_2 \|\mathbf{x}_j\|_2}, \tag{3.2}$$

where $\|\mathbf{x}\|_2$ denotes the L2 norm of the vector $\mathbf{x}$. For positive data this metric is bound between 0 and 1. The cosine distance is less sensitive to outliers in our case and produces more reasonable clustering for turbulence profiles.

In calculating the distance matrix with profile measurement vectors $\mathbf{x}_i$ we have made the implicit assumption that all the components of the vector (altitude bins) are independent. This means that the height of the turbulent layer is not taken into account in the clusters and therefore layers that are close in altitude are considered as similar in the distance matrix as layers far apart in altitude. This is not ideal since we are dealing with measurements with finite altitude resolution. We therefore modify the cosine metric as described in Sidorov et al. (2014). By introducing a $p \times p$ matrix S describing the similarity between vector components we obtain the soft cosine distance

$$\delta_{ij}^{\text{softcos}} = 1 - \frac{\sum_k^p \sum_{k'}^p S_{kk'} \mathbf{x}_{ik} \mathbf{x}_{jk'}}{\sqrt{\sum_k^p \sum_{k'}^p S_{kk'} \mathbf{x}_{ik} \mathbf{x}_{ik'}} \sqrt{\sum_k^p \sum_{k'}^p S_{kk'} \mathbf{x}_{jk} \mathbf{x}_{jk'}}}, \tag{3.3}$$

where both k and k' run through vector components. For $S = 1$ this reduces to the cosine distance described in Equation 3.2.

The altitude resolution of the Stereo-SCIDAR is given by

$$\delta h = \epsilon \frac{\sqrt{\lambda |h - h_{\mathrm{conj}}|}}{\theta}, \tag{3.4}$$

where λ is the operating wavelength, taken here to be 500 nm, h_{conj} is the conjugate altitude of the imaging plane (for the Stereo-SCIDAR at Paranal $h_{\mathrm{conj}} = -3$ km), θ is the separation of the double star used to compute the turbulence profile and ϵ is a constant which we take as 0.5 (Avila et al., 1997, see also section 6.2 in this thesis). We define each row k of S as a gaussian with mean h_k and full width half maximum defined by Equation 3.4. Each row is normalised such that all $S_{kk} = 1$. The widths of these gaussians correspond very well to the response functions of the instrument (Shepherd et al., 2014). The similarity matrix S used for the Stereo-SCIDAR data is shown in Fig. 3.2. This process ensures that the distance between profiles as defined by our metric takes into account the finite altitude resolution of the instrument.

3.2.2 Clustering process

The second choice that must be made in hierarchical clustering after the distance metric is the method of defining the inter-cluster distance or linkage. Here we use average linkage, where the inter-cluster distance is defined as the mean pairwise distance between the members of the two clusters.

A description of the process we employ to perform agglomerative hierarchical clustering is as follows:

1. Compute pairwise distance matrix D for the chosen metric.
2. Merge the two closest elements.
3. Define the new distance from this cluster to the rest of the elements according to the chosen inter-cluster distance.

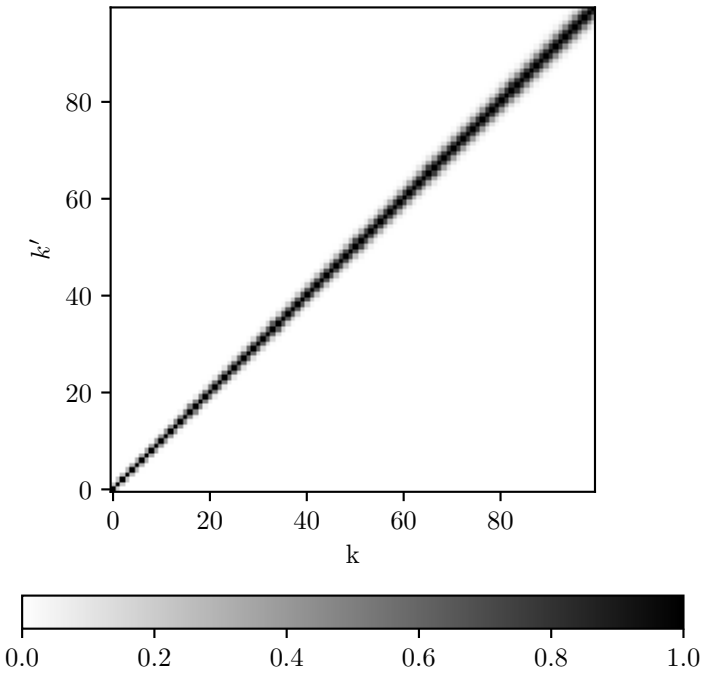

Figure 3.2: Similarity matrix S between altitude bins for the Stereo-SCIDAR at Paranal, using the average stellar separation of 12.5", wavelength 500 nm and conjugate altitude $h_{\text{conj}} = -3$ km.

4. Repeat (ii) and (iii) until there are two remaining clusters that are merged into one representing the whole dataset.

The clustering was performed in python using the hierarchy module in SciPy, which for average linkage clustering utilises the nearest-neighbours chain algorithm (see e.g. Müllner, 2011).

3.2.3 Data preprocessing

The turbulence profiles contain many zero measurements. Usually these occur when turbulence in an altitude bin is below the sensitivity of the instrument but also can be a result of noise propagated through a non-negative least squares fit in the data processing pipeline. While it is tempting to treat all zero values as missing data and remove them from the analysis, this can have a profound effect on the calculation of distance between profiles. Thus we choose not to remove these zero measurements before clustering.

The dynamic range of C_n^2 measurements in the data poses a problem in clustering. The distance between profiles tends to be dominated by strong turbulence since these measurements can be up to 100 times stronger than weak or moderate turbulence (see Fig. 3.3). We are more interested in the significance of turbulence, i.e. whether turbulence is high or low relative to the average level of turbulence at a particular height. The C_n^2 measurements in each altitude bin are log-normally distributed but the censored nature of the data, where measurements below a sensitivity limit are recorded as zeros, means that we cannot log transform the data and perform the common normalisation procedure of subtracting the mean and dividing by the standard deviation for each altitude bin. Instead we find that simply dividing by the mean of each altitude bin is effective in "flattening" the profiles, reducing the importance of strong ground layer bins and effectively increasing the importance of weak high layer turbulence such that turbulence at all heights is considered approximately equally in the clustering. The effect of this normalisation on the distance matrix can be seen in Fig. 3.4. Note that the profiles are additionally L2 normed when the cosine distance is used.

3.2.4 Determining the number of clusters

We seek to cluster turbulence profiles until they are separated according to their structure, such that we can extract a profile from each producing a representative set of profiles. To quantify this we employ two metrics, the within cluster variance and the silhouette score.

We define the within cluster variance as the sum of the distances of the members of each cluster to the profile we extract as the centre of that cluster. We determine the distance with the same soft cosine metric used in the clustering:

$$W_N = \sum_{m=1}^{N} \sum_{i=1}^{n_m} \delta^{\text{softcos}}(X_{im}, X_m^*) \tag{3.5}$$

where n_m is the number of profiles in cluster m, N is the total number of clusters, the X_{im} are all the profiles in cluster m and X_m^* is the centre of cluster m. The

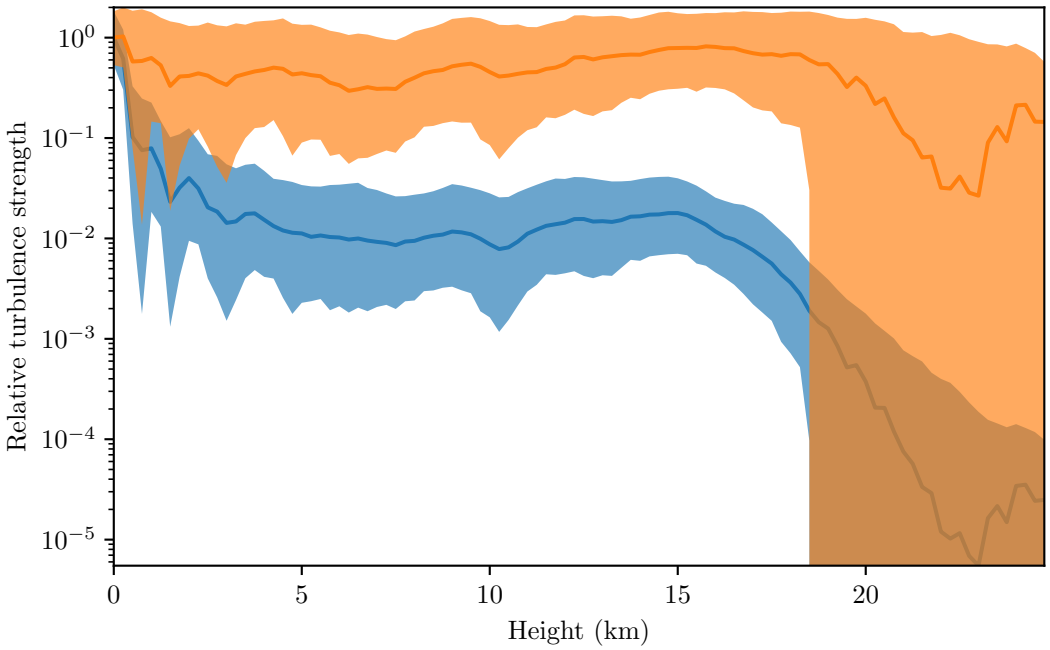

Figure 3.3: The effect on the median (solid line) and interquartile range (shaded areas) of the turbulence strength due to normalisation by dividing each altitude bin by its mean value. Blue shows the distribution before normalisation and orange after normalisation. Turbulence strength is defined relative to the median value of the first (0 m) bin. Note for altitudes above around 18 km, the lower quartile is equal to 0, hence on the log scale it drops to $-\infty$.

quantity W_N is analogous to the within cluster sum of squares that is minimised in K-means clustering, with the squared euclidean distance substituted for the cosine distance and the cluster centroid $\bar{X}_m$ substituted for our more general cluster centre X^*_m. As we increase the number of clusters N, W_N will decrease rapidly at first and plateau as the clustering becomes less effective. It is at this point that we define the number of clusters, a technique known as the elbow method.

The second metric is the silhouette score (Kaufman and Rousseeuw, 2005, chapter 5). This metric is defined for a single measurement i as

$$s_i = \frac{b_i - a_i}{\max\{a_i, b_i\}}, \tag{3.6}$$

where a_i and b_i are quantities dependent on the distance matrix D. a_i represents the average distance between measurement i and all the other members of the cluster i is assigned to. Conversely, b_i represents the average distance between i and all the members of every other cluster. If $a_i > b_i$ resulting in $s_i < 0$ then this

profile is on average closer to members of other clusters and is probably assigned to the wrong cluster. If $b_i > a_i$ then $s_i > 0$ and the profile is probably assigned to the correct cluster. A more positive silhouette score is therefore indicative of better clustering. s_i is by definition bounded between -1 $< s_i <$ 1. By taking the mean silhouette score s over all members of the dataset we gain insight into the quality of clustering over all clusters.

These two metrics are chosen since, while not completely independent of one another, they incorporate distinct parts of the clustering process. The silhouette score depends solely on pairwise distances between profile measurements described in the distance matrix, whereas the within cluster variance also includes our chosen centre for each cluster X^*. This allows us to draw a more robust conclusion as to the number of clusters in the dataset.

3.2.5 Cluster centres

After performing the clustering and subsequently partitioning our dataset we must extract a single turbulence profile from each cluster. The resulting profiles vary greatly depending on the method used, so we present two methods and hence two sets of turbulence profiles here.

The simplest way to extract a profile from a cluster is to take an average of each altitude bin in a cluster. More specifically, we take the mean profile in our normed space, then un-normalise this profile and adjust it such that the integrated strength of the profile coincides with the median seeing for the cluster. This results in any features of the clustering common to all profiles in a cluster being retained while features belonging only to a subset of profiles will be averaged out as described earlier. The profiles thus produced will be an unrealistic but conservative description of the variability in the profile and will represent the profile in the majority of cases.

Alternatively, we have already defined a metric that describes how well a profile fits

into a particular cluster — the silhouette score. The profile in each cluster with the maximum silhouette score is therefore the best fit profile for that cluster according to our distance metric. In this way we can select an individual turbulence profile as the cluster centre. We therefore select the N profiles from the dataset that represent the centre of each of the N clusters. These profiles will not be "typical" in the sense that they represent the majority of measurements, but will describe a greater amount of variability which would be useful for AO simulation.

3.3 Application to ESO Paranal dataset

We use the 2018A Stereo-SCIDAR data release described in Osborn et al. (2018). The dataset consists of 10,691 turbulence profile measurements taken over 83 nights between April 2016 and January 2018. The profiles have 100 equally spaced altitude bins between the ground and 25 km.

The metrics for selecting the number of clusters are shown in Fig. 3.5. There is a clear peak in the silhouette score at 17–19 clusters. After 19 clusters the silhouette score drops off indicating that further clustering does not improve the quality of the resulting clusters. The within cluster variance in the average centre case shows no clear elbow but a transition from steep to shallow gradient at 15–20 clusters. In the single profile centre case however there is a clearer flattening of the gradient at 18 clusters, corresponding to the centre of the peak in the silhouette score. We therefore choose 18 as our number of clusters.

The magnitude of the silhouette score is only around 0.17 at the peak which is indicative of structure in the data that has not been captured in the clustering. Indeed we can see from the full set of extracted profiles shown in Fig. 3.6 and Fig. 3.7 that members of some clusters, especially those containing large numbers of profiles, are fairly inhomogeneous in structure. However, the clustering has for the most part selected and separated profiles with turbulence in strong single layers. This strong single layer is common to almost all profiles in a cluster. The lowest

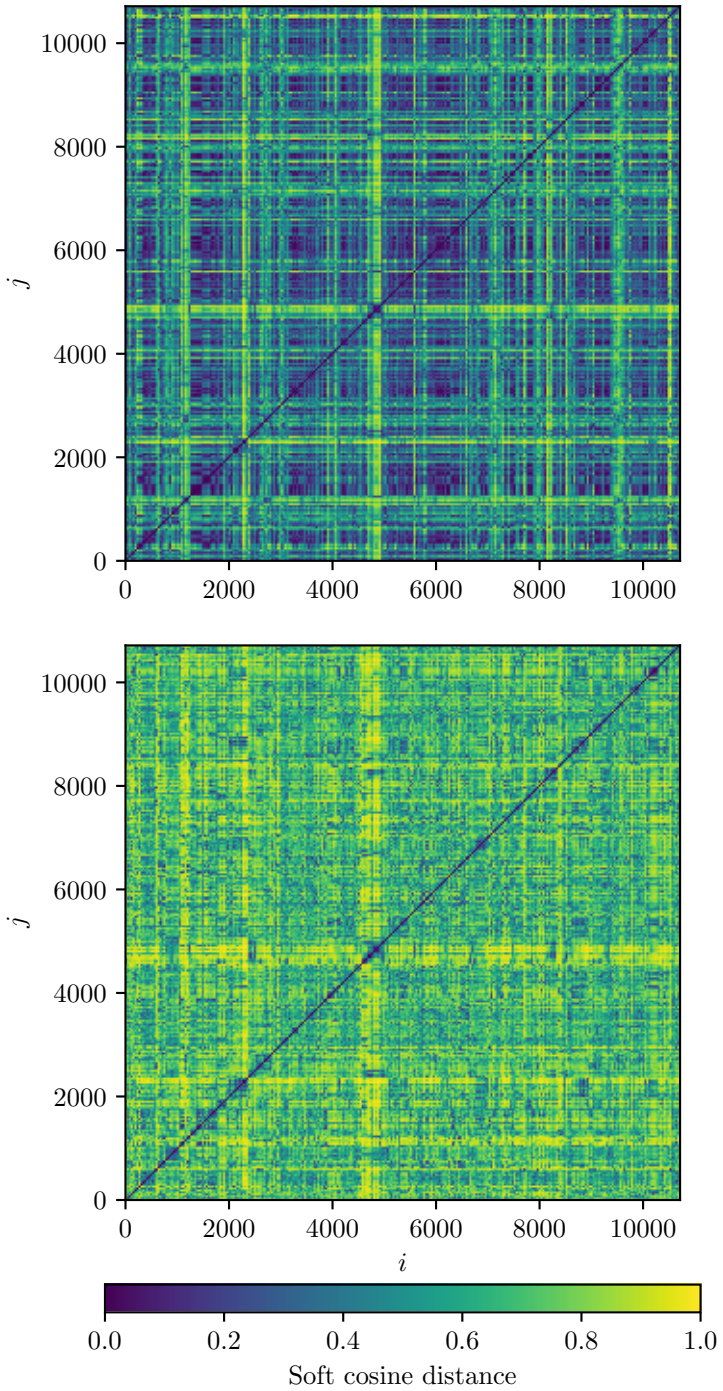

Figure 3.4: Pairwise distance matrices calculated using the cosine metric defined in Equation 3.2 for the 2018A dataset. *Top:* Raw C_n^2 measurements. *Bottom:* Profiles normalised by dividing by the mean value in each altitude bin.

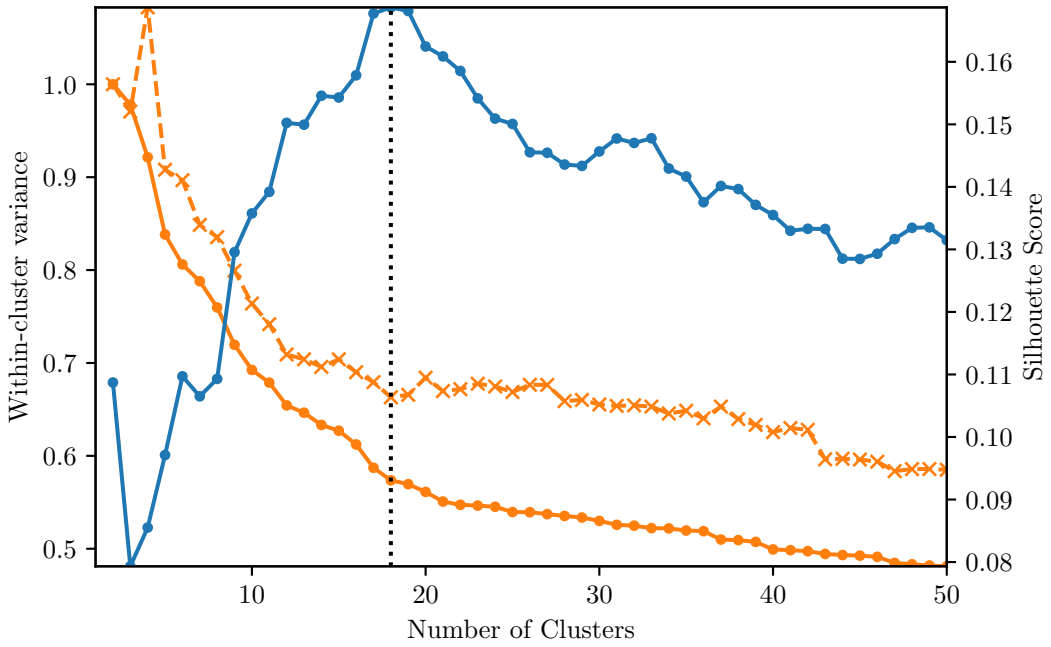

Figure 3.5: Within cluster variance (orange) and silhouette score (blue) for the Paranal Stereo-SCIDAR dataset with increasing numbers of clusters. The two within cluster variance lines represent the two methods of defining the centre of a cluster: average (solid, circular markers) and single profile (dashed, cross markers). Within cluster variance in both cases is normalised to the value at 2 clusters. The dashed vertical line is at 18 clusters.

turbulent layers (e.g. clusters 14, 16, 18) tend to be thinner and stronger whereas high layers (e.g. clusters 2, 4, 5) tend to be more spread out and weaker. This may be an instrumental effect due to the reduction in native altitude resolution of the Stereo-SCIDAR with increasing height as described by Equation 3.4 and included in the clustering by our use of the soft cosine distance. In total, clusters with significant high altitude ($h \geq 10$ km) layers contain around 55% of all profiles. We have also separated one ground-layer dominated cluster (18) representing only 1.4% of profiles. This propensity towards high altitude turbulence is expected from atmospheric parameter statistics for this data: a median isoplanatic angle of 1.75" and fraction of turbulence below 600 m of 0.4 (Osborn et al., 2018).

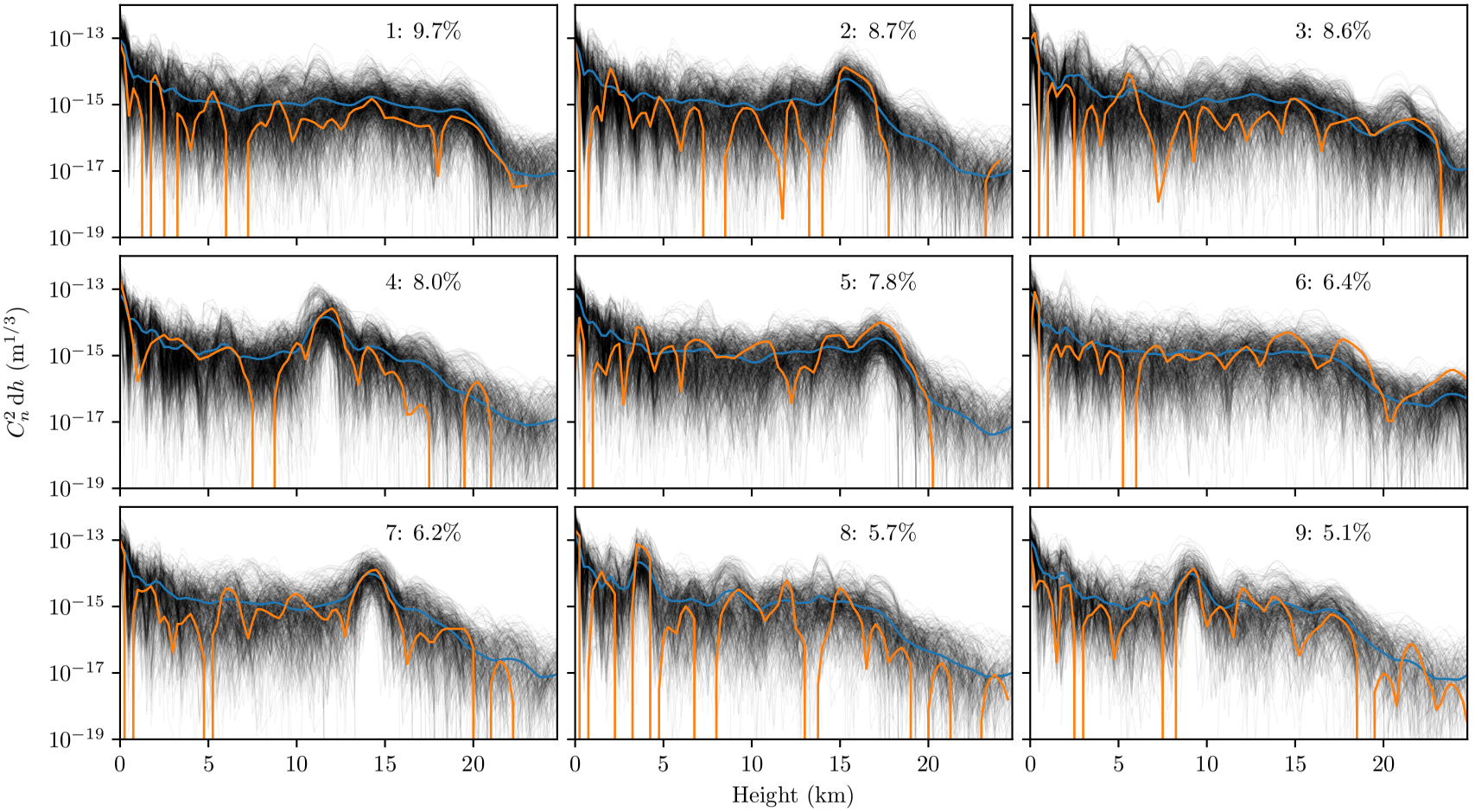

Figure 3.6: Full atmosphere turbulence profiles for Paranal extracted through our hierarchical clustering method. Black lines represent every measurement of the turbulence profile in the given cluster. The two methods of obtaining the centre of each cluster are shown as blue (average profile) and orange (single profile) lines. Each cluster is numbered in descending order of the number of profiles in the cluster along with the percentage of all profiles contained in that cluster. Note that these profiles are not normalised.

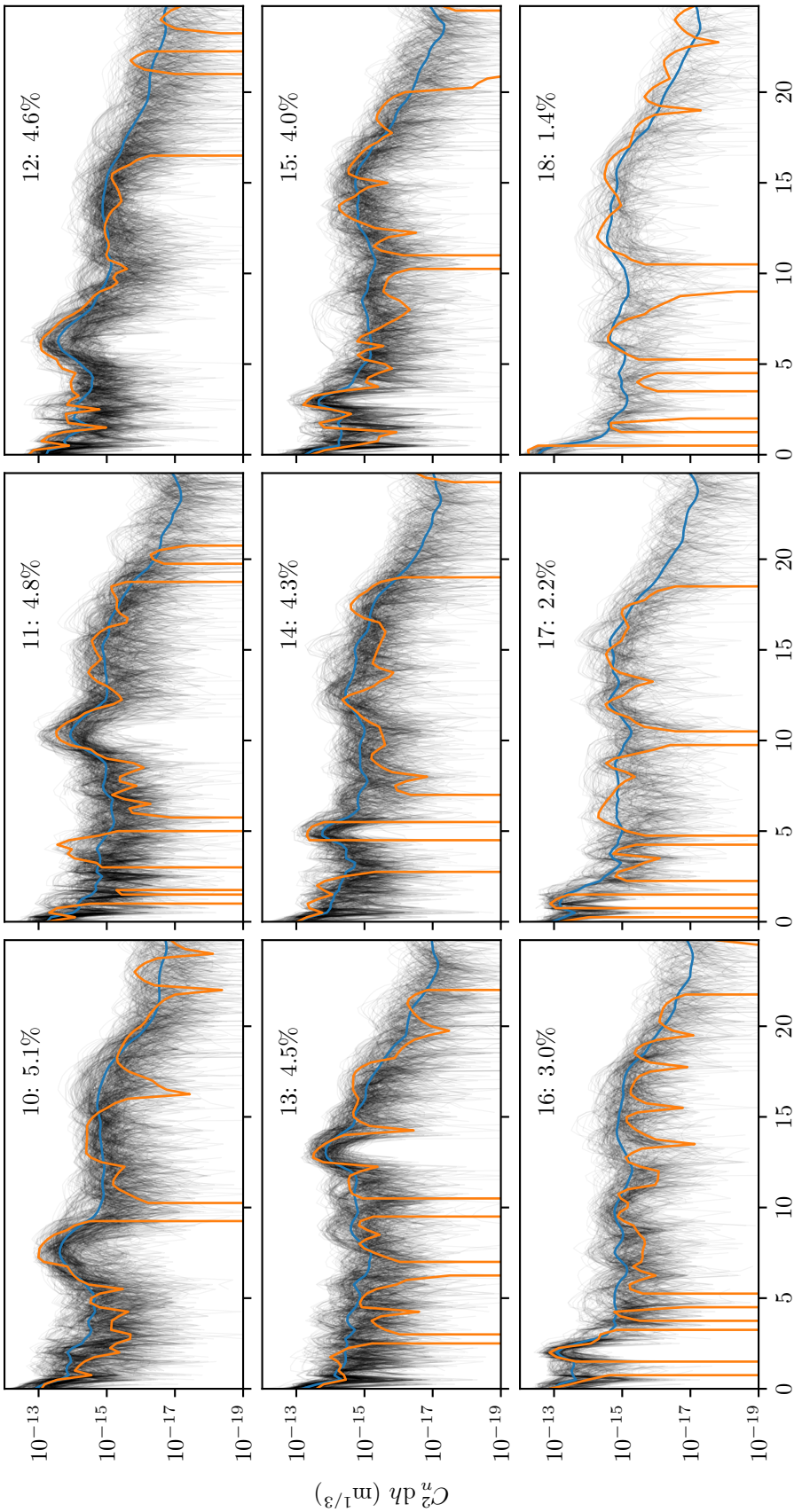

Figure 3.7: Fig. 3.6 continued

3.3.1 Comparison Profiles

The most conventional way to reduce a large turbulence profile database to a small set of representative profiles is to first bin the profiles according some integrated parameter, then take an average profile from each bin. The most common parameter used is the integrated strength (seeing), either measured from the profile itself or a contemporaneous measurement from a dedicated seeing monitor such as a DIMM (Sarazin and Roddier, 1990). This is the case for the ESO 35 layer profiles for Paranal (Sarazin et al., 2013), consisting of a profile associated with median seeing and four profiles associated with seeing quartiles. We also produce 18 profiles by binning the Stereo-SCIDAR dataset into 18 seeing bins to provide a more equal comparison to our 18 clustered profiles.

In addition we compare to the good, high and low profiles computed using the method defined in Sarazin et al. (2017). Rather than binning by the total integrated turbulence strength, the dataset is split into three cases: good seeing, high altitude dominated and low altitude (ground layer) dominated profiles. The average from each of these cases is taken to produce three reference turbulence profiles for Paranal. We also include a profile "all" defined as the average of all profiles in the dataset.

3.3.2 Validation and comparison

Whether or not the clustered profiles represent the dataset as a whole is a difficult question to answer since the concept of "representativeness" can be defined in many different ways. The ultimate aim of this study is to produce a set of turbulence profiles that can be used in AO simulation with the knowledge that they reflect the variability in the turbulence profile seen in reality in some meaningful way.

Here, we validate our clustered profiles using the atmospheric parameters r_0 and θ_0. In this sense we validate the profiles only in an atmospheric sense, rather than with reference to a particular instrument. However, as discussed in section 2.3.6 these

atmospheric parameters do not necessarily apply to tomographic AO systems. A validation of these profiles using Fourier tomographic AO simulation is presented in chapter 4.

We calculate these parameters for the entire dataset and for our small sets of profiles and the results are shown in Fig. 3.8. We can see that splitting the dataset into 18 seeing bins and taking an average profile from each produces a set of profiles that by design fits very well with the distribution of r_0. However little of the variability in θ_0, a better indicator of the distribution of the turbulence, is described by these profiles. The ESO 35 layer median and quartile profiles behave in the same way. In particular, small values of θ_0 indicating significant high altitude turbulence are poorly represented. The good, high and low profiles provide a better description of the variability θ_0 but are slightly skewed towards larger values of r_0 indicating weaker turbulence. The "all" profile lies in approximately the centre of both distributions as one would expect.

We include in the upper panel of Fig. 3.8 the distribution of integrated parameters for clustering with some different parameters to those presented above. We find that if we use the euclidean distance instead of the soft cosine distance, the resulting clusters are heavily skewed towards smaller values of both r_0 and θ_0. Without normalisation, the clustering produces profiles which better describe the distribution of θ_0 whilst being skewed towards larger values of r_0. Combining the soft cosine distance with the normalisation described above (shown in the middle panel of Fig. 3.8), we produce profiles that accurately reflect the distributions of both parameters. However, the two methods of defining the centre of a cluster display different results here. By taking an average profile for each cluster we produce a set of profiles whose integrated parameters are grouped tightly around the centre of the distribution for the dataset. In the case of the r_0 distribution this is somewhat by design since we are not sensitive to changes in integrated strength in our clustering, therefore we produce clusters whose individual distributions of r_0 follow approximately the distribution of r_0 for the entire dataset. When we set the

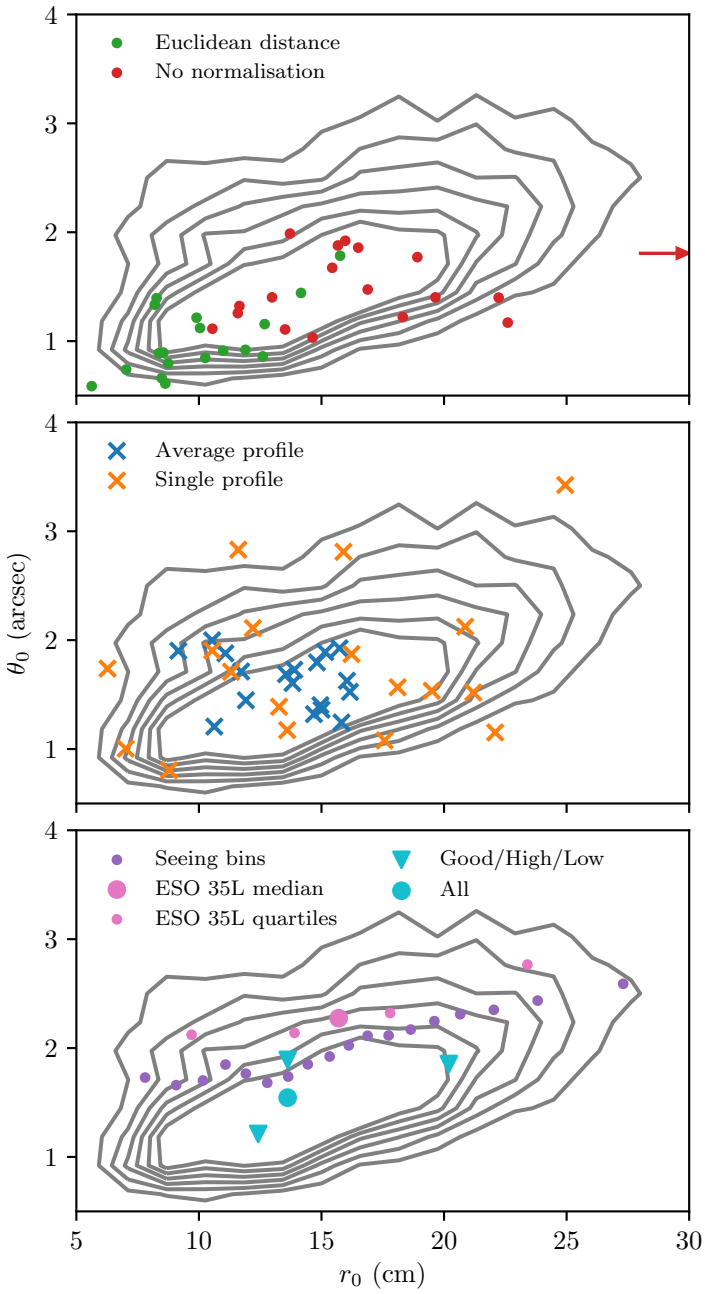

Figure 3.8: Distribution of integrated parameters r_0 and θ_0 for the entire dataset (contours) and small sets of profiles. *Upper*: Bad clusterings generated through our clustering method with suboptimal parameters. One outlier profile in the no normalisation case with $r_0 = 33$ cm is indicated by an arrow. *Middle*: The two sets of 18 representative clustered profiles with cluster centres defined as average and single profiles. *Lower*: Comparison profiles as discussed in section 3.3.1

.

integrated strength of each of these clustered profiles to the median seeing for that cluster the values will tend to group around the median for the entire dataset. In the distribution of θ_0 however we see a similar tight grouping, with less of the bias towards larger values.

In contrast, if we take a single profile with the maximum silhouette score as our cluster centre we produce a set of profiles that are spread more widely around parameter space. These profiles therefore describe more variability. Again in the case of r_0 this is somewhat by design — since the clustering is not sensitive to r_0 we have essentially randomly sampled the distribution with 18 points, resulting in a wider spread around the parameter space.

Thus we have produced two sets of profiles that are both representative in different ways. Our average profiles are "typical" since they can be used to represent the profile most of the time. The single profiles are not typical since they represent a single measurement at a single time that is unlikely to represent the profile in the majority of times. However, these profiles exhibit more of the variability in the atmosphere that would be useful in characterising the performance of an AO system.

The clustered turbulence profiles presented here are publicly available at `https://durhamuniversity.app.box.com/v/clusters-paranal`.

3.4 Conclusions

We have outlined a method for obtaining a small set of representative turbulence profiles from a large dataset, where all steps of the process are informed by quantitative analysis of the clustering and resulting profiles.

We applied this method to the Stereo-SCIDAR dataset from ESO Paranal, partitioning over 10,000 measurements into 18 clusters. We have used two methods to obtain the centre of each cluster resulting in two sets of 18 high resolution full

atmosphere turbulence profiles with 100 altitude bins between 0 and 25 km. While the clustering has not preserved all the structural variation in the turbulence profile at Paranal, each cluster is dominated by a single strong turbulent layer in addition to the ground layer. The height of this strong layer varies over the full range of altitudes.

Through analysis of integrated turbulence parameters it has been shown that the two sets of profiles are two distinct forms of "representative" profile. Taking the average profile for each cluster results in typical profiles grouped around the centre of r_0-θ_0 parameter space and represent the profile in the majority of cases. Conversely defining a single profile as the cluster centre produces a set of profiles that represent more extreme variability in the dataset.

More generally in the context of site characterisation and monitoring, clustering methods can be applied not only to large databases of turbulence profiles but to any multivariate data (e.g. wind, humidity, temperature, sodium layer profiles) in order to extract small sets of representative conditions. Data from existing instruments such as AO telemetry or point spread functions could also be used either as input to the cluster analysis or as validation for representative atmospheric conditions.

4

Validation of reference profiles for tomographic adaptive optics

Note: this chapter is an adaptation of Farley et al. (2019)

4.1 Introduction

We have shown in chapter 3 that we are able to extract a small set of optical turbulence profiles from a data set that are representative of the full distribution in terms of atmospheric parameters r_0 and θ_0. From section 2.3.6 and more specifically Eqs. 2.34 and 2.35 we can also draw the conclusion that these profiles will give representative performance for an SCAO system.

However, this conclusion may not be made for a tomographic AO system. Since wavefront error in these systems depends on some parameters of the system in question (e.g. geometry of guide stars and their relative positions) in addition to the C_n^2 profile, their error terms cannot be modelled by integrated atmospheric parameters as for SCAO.

Monte Carlo simulations of tomographic AO are currently used extensively to evaluate the performance impact of different designs. The validity of these simulations is dependent to some extent on a set of accurate reference turbulence profiles to describe typical conditions and variability of the atmosphere at a particular site. Single or very few reference turbulence profiles must be used due to long computation times, and these profiles are usually chosen by taking mean or median profiles from large databases obtained by site characterisation and monitoring campaigns (see e.g. Els et al., 2009; Dali Ali et al., 2010; Vernin et al., 2011; Osborn et al., 2018; García-Lorenzo and Fuensalida, 2011). Typically reference profiles are selected from these databases that are representative of integrated parameters of the turbulence such as r_0 (or seeing) and θ_0, for which the distribution for the entire database can be easily computed (Sarazin et al., 2013; Els et al., 2009). Therefore these profiles cannot be constructed with tomographic systems in mind – instead it must be assumed *a priori* that, for example, a median C_n^2 profile will result in median tomographic AO performance.

One important source of error in a tomographic AO system resulting from the profile is the tomographic error, which arises from imperfect reconstruction of the turbulent phase volume at altitude (see Eq. 2.30). This error forms a large part of the error budget for most tomographic AO systems (see e.g. Gilles et al., 2008; Martin et al., 2017) and is common to all systems for a given guide star asterism and turbulence profile regardless of particular AO flavour (LTAO, MCAO, MOAO, etc.). It is therefore important that the turbulence profiles used in simulation provide tomographic errors similar to those that would be seen on sky. The impact of the turbulence profile on the tomographic error has been modelled by Tokovinin and Viard (2001), showing that the stratification of turbulence in thin layers is of greater importance for smaller error than the overall strength of the turbulence. This is supported in simulation by Fusco and Costille (2010) using a limited set of turbulence profiles.

Here we employ a fast analytical AO simulation (see section 2.3.5 and Neichel et al.

(2009)) in order to directly ascertain the impact that the varying turbulence profile has on the tomographic error using the aforementioned Stereo-SCIDAR 2018A database from ESO Paranal, Chile. By operating in the Fourier domain and computing the power spectral density (PSD) of the AO-corrected PSF we can obtain the tomographic error of an ELT scale AO system for a particular set of atmospheric conditions in seconds as opposed to hours on modest hardware. We are therefore not limited in the number of turbulence profiles we can use, allowing us to understand how the tomographic error is distributed over a large database of real turbulence profiles. Additionally, through comparison of the distribution of tomographic error across the Stereo-SCIDAR dataset to small sets of profiles commonly used to represent the Paranal turbulence profile in Monte Carlo simulation, we can assess how representative these profiles are.

4.1.1 Simulation parameters

We simulate an ELT-scale system, with the fixed simulation parameters summarised in Table 4.1. We adopt a simple LTAO configuration, with a single ground-conjugated DM and six LGS in a circular asterism. The reconstructor is optimised and performance measured on-axis such that there is no contribution from generalised fitting error. In addition we only integrate the PSD within the AO-correction radius such that there is no contribution from classical fitting error. In this way we measure only the tomographic error associated with the imperfect reconstruction of the turbulent volume. Included in this tomographic error is a constant contribution from the noise in the LGS WFS measurements. Note also that we use the true 100 layer turbulence profile in the reconstructor, i.e. it is assumed that the profile is known perfectly by the system and there is no model error incurred. An investigation into the effect on tomographic error when the profile is not perfectly known is presented in chapter 5.

We set the six LGS in asterisms with diameters Θ of 1, 2, and 4 arcminutes to obtain tomographic error estimates applicable to a wide range of instruments, from

Telescope diameter (m)	39.3
Projected subaperture size (m)	0.5
Projected DM pitch (m)	0.5
# LGS	6
# DM	1
DM conjugation altitude (m)	0
Tomographic reconstructor	MMSE
Outer scale L_0 (m)	25
LGS noise (rad^2)	1
Zenith angle (deg)	0

Table 4.1: Fixed simulation parameters for all LGS asterisms.

narrow-field LTAO to wide field MCAO and MOAO.

4.1.2 Comparison profiles

We compare the distribution of tomographic error across the 10,691 profiles to some small sets of profiles that aim to be representative of different atmospheric conditions. These profiles were have introduced in section 3.3.1 however they are also mentioned here for completeness. Firstly, we use the commonly used ESO 35 layer (35L) median and seeing quartile profiles (Sarazin et al., 2013). These profiles are composed of combinations of profile measurements from both Paranal and Armazones, binned by seeing and averaged.

The second set is the 100 layer good, high, low and all (g/h/l/a) profiles defined from the same Stereo-SCIDAR 2018A data set (Sarazin et al., 2017). This analysis splits the profiles into three groups: good, where the total integrated turbulence is low; high, where the profile is dominated by turbulence above the ground layer and low, where the profile is dominated by the ground layer. The mean of profiles falling into each category is taken producing three reference profiles. In addition, the "all" profile is the mean of the entire data set.

Finally, we consider the profiles produced by the clustering method described in chapter 3 (Farley et al. (2018)). Here, cluster analysis was used to partition the 10,691 profiles into 18 groups according to their shape. Two methods of defining

the centre of each cluster are used: taking the mean profile from each cluster and selecting a single profile to represent each cluster. There are therefore two sets of 18 profiles from this method.

We compute the tomographic error for these profiles with the same simulation method and the parameters as described above so that the resulting values are directly comparable to the distribution over all profiles from the 2018A database.

4.2 Simulation results

The distributions of tomographic error for the simulation parameters listed in Table 4.1 and our three LGS asterisms are shown in Fig. 4.1. We can see that for all asterism diameters the tomographic error across all turbulence profiles is approximately log-normally distributed, with median values of 84 nm, 133 nm and 192 nm respectively for 1, 2 and 4 arcminute asterisms. We list the values of tomographic error obtained in these simulations in Table 4.2.

Using the distributions for all the profiles of the 2018A dataset we are able to place the small sets of profiles in context. We can see that the ESO 35 layer and good/high/low/all profiles produce tomographic errors towards the higher end of the distribution. This is also true for the clustered profiles where we take an average profile from each cluster. The clustered profiles where a single profile from each cluster is chosen to represent that cluster are however more representative of the distribution of tomographic error.

It is informative to consider the scaling of tomographic error with LGS asterism diameter. In addition to simulations with all profiles at 1, 2 and 4 arcminutes, we select a small number of profiles with which to perform simulations with finer asterism diameter sampling. Three profiles are selected that consistently provide median, lower and upper quartile error according to the full distributions in Fig. 4.1. We show how the tomographic error evolves for these profiles with asterism diameter in Fig. 4.2. From Tokovinin and Viard (2001) we expect the tomographic

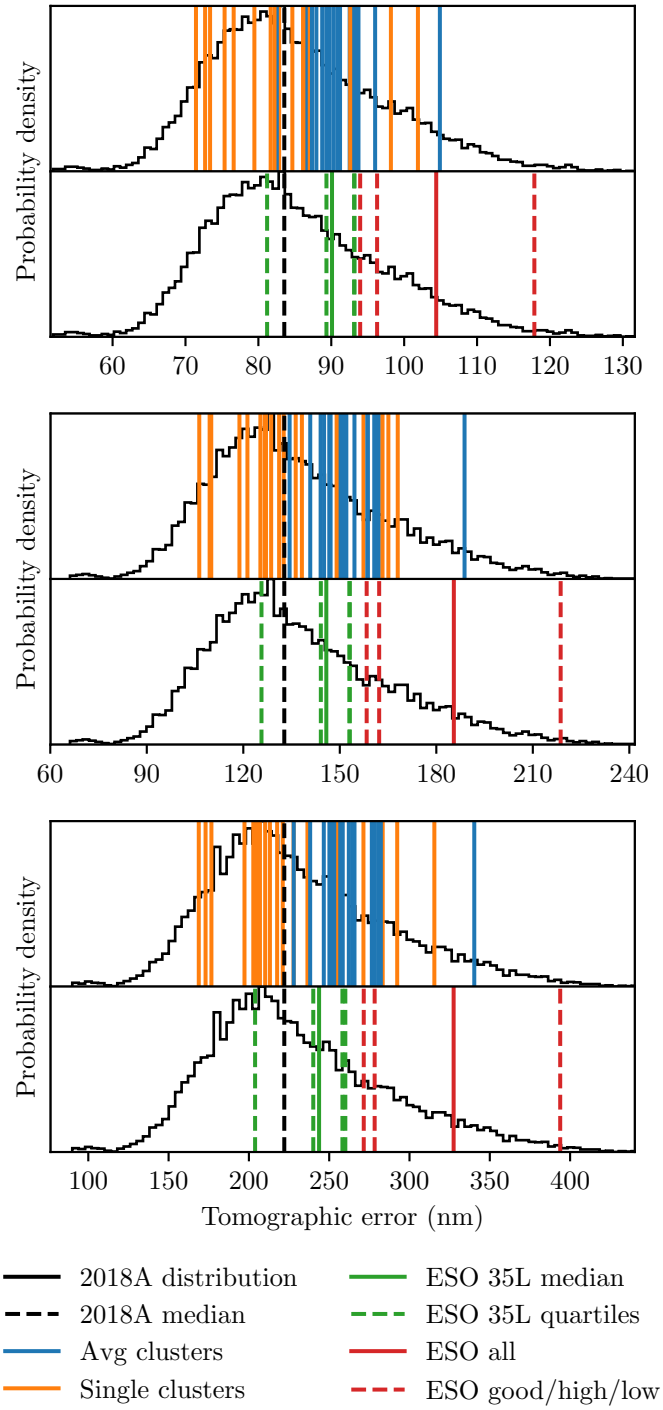

Figure 4.1: Histograms showing the distribution of tomographic error for all profiles (black) compared to small sets of profiles (coloured vertical lines). From upper to lower panel: 1, 2 and 4 arcminute LGS asterisms. Comparison profiles for each asterism are separated into two panels for clarity: the background histograms for each pair are identical. The median tomographic error for each asterism is indicated by the black dashed line. Note the change of x axis for each asterism diameter.

Profile(s)		Θ 1'	2'	4'
2018A database [10691 profiles]	Q1	77	118	192
	Median	84	133	222
	Q3	93	154	265
Clusters (avg) [18 profiles]	Q1	88	147	252
	Median	91	151	260
	Q3	93	159	278
Clusters (single) [18 profiles]	Q1	77	122	203
	Median	83	130	215
	Q3	87	146	250
ESO 35L median		90	146	244
ESO 35L Q1		81	126	204
ESO 35L Q2		89	144	240
ESO 35L Q3		93	153	258
ESO 35L Q4		93	153	260
ESO good		94	158	272
ESO high		118	219	394
ESO low		96	162	248
ESO all		104	185	327

Table 4.2: Tomographic error in nm rms for the Stereo-SCIDAR 2018A dataset as well as our comparison profiles, for each of the 1, 2 and 4 arcminute LGS asterisms simulated. We consider the 2018A dataset and the two sets of 18 clustered profiles as distributions, calculating the median, lower and upper quartiles of tomographic error for each.

error in the zero-noise limit to increase as $\Theta^{5/3}$, however we find that a pure 5/3 power law does not give a good fit to our computed errors. We find instead an expression of the form

$$\sigma^2_{\text{tomo}} = \alpha\Theta^{\beta} + \sigma^2_0, \tag{4.1}$$

with fit parameters α and β, provides a good fit to within 1% fractional error across our asterism range. Note that the fitting is performed with error variance (nm^2). The parameter σ^2_0 describes the additional error resulting from non-zero noise in the LGS WFS, which may be computed by setting $\Theta = 0$ in the simulation. For small asterism diameters, the error arising from the noise dominates and thus should be considered an important parameter in simulation.

The fact that we must introduce the parameter β in order to obtain a good fit has the important consequence that each profile scales slightly differently with

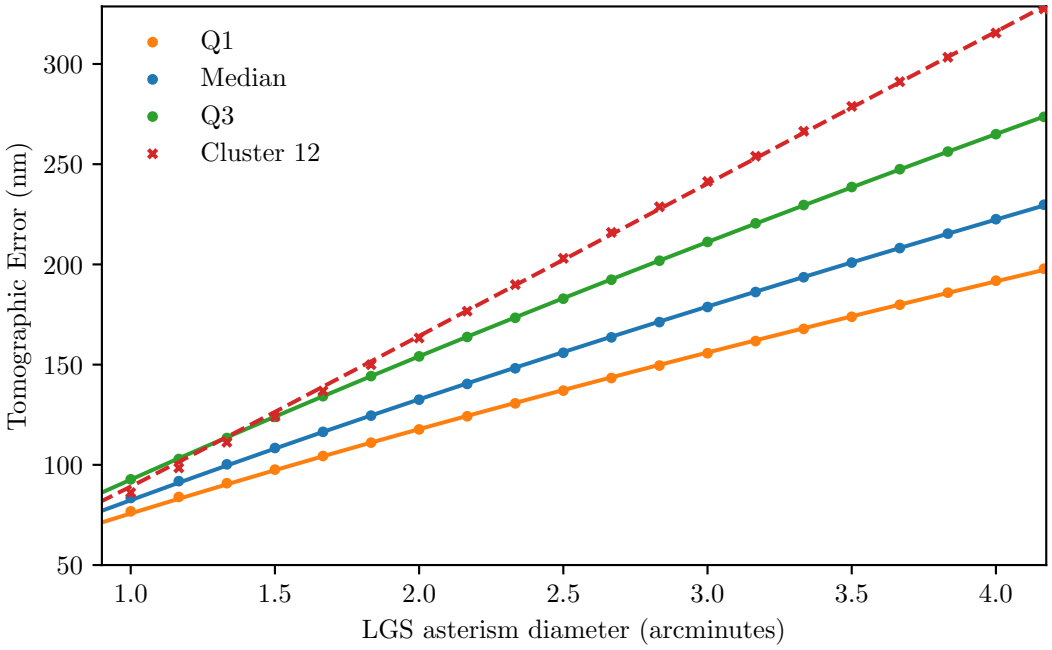

Figure 4.2: Computed tomographic error from Fourier simulation (circlular points and crosses) as a function of circular LGS asterism diameter. Three profiles are chosen to represent median (blue) and upper/lower quartiles (green/orange). Lines indicate best fit to the model in Eq. 4.1. Additionally an example of a profile whose tomographic error scaling with asterism diameter deviates substantially is shown in red.

asterism diameter. Therefore, for example, it is not guaranteed that a profile selected for median tomographic error at one asterism will maintain median error as the asterism changes, since it could scale more or less rapidly relative to other profiles. We show this in Fig. 4.2 with a profile (single cluster 12) that provides just over median error at 1 arcminute, but rapidly increases to around 80th percentile at 2 arcminutes and 90th percentile at 4 arcminutes.

We may illustrate this over the full data set by computing the percentile of the tomographic error distribution to which each profile belongs for two asterism diameters. In Fig. 4.3 we compare the percentiles of each profile in the data set for 1 arcminute and 4 arcminute diameters. We can see that the majority of profiles fall close to the $y = x$ line: as asterism diameter is increased, the profile will remain at approximately the same percentile of the distribution, with some small amount (approximately ± 10 percentile) of variability. This is clearly the case for

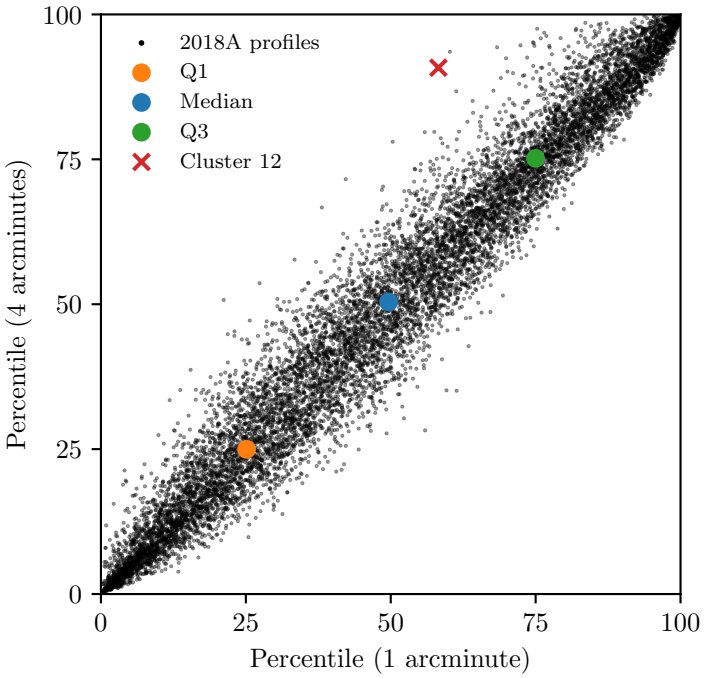

Figure 4.3: Percentiles of the tomographic error distribution for which the profiles of the 2018A data set (black dots) fall, for 1 arcminute and 4 arcminute asterism diameters. Also shown are the Q1, median and Q3 profiles as well as the outlier cluster 12.

our selected median and lower/upper quartile profiles. However, there are also a clear number of outlier profiles, one of which being cluster 12, showing large shifts in terms of percentile. Care should therefore be taken when extrapolating performance between asterism diameters, as it is impossible to ascertain how the tomographic error provided by a profile will scale with asterism diameter without simulation across multiple diameters and fitting to a model such as Eq. 4.1. By computing a full distribution of tomographic error as in Fig. 4.1 and comparing individual profiles we can be sure that we have selected a representative profile only for that particular asterism and system parameters.

With the above caveats, from this point onwards we will consider only the tomographic error for the $\Theta = 2$ arcminute asterism for further analysis. We choose this particular asterism since for MCAO-like systems represented by this asterism the tomographic error is most likely to be a significant if not dominant term in the error budget.

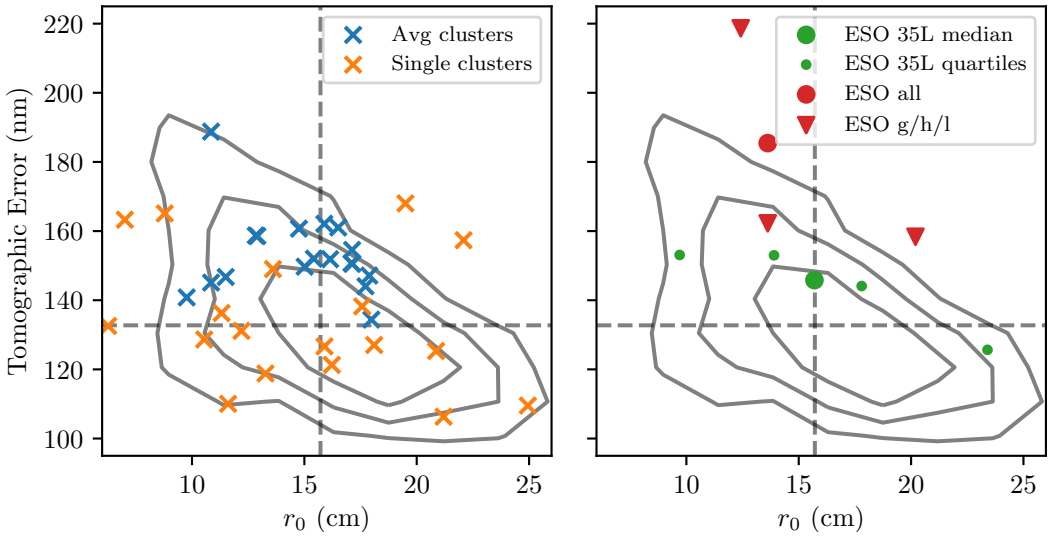

Figure 4.4: Parameter space of tomographic error (for the $\Theta = 2$ arcminute asterism) and r_0. In both panels, the grey contours represent the 25th, 50th and 75th percentiles of the two-dimensional distribution across the 2018A dataset. Dashed horizontal and vertical lines represent the median values of these distributions. Overplotted are reference profiles, with clustered profiles in the left panel and ESO profiles in the right panel.

All of the small sets of profiles considered here have been shown to be representative of the distributions of parameters r_0 and θ_0 according to the 2018A dataset (Farley et al., 2018, see chapter 3), with the exception of the ESO 35 layer profiles that were shown to be biased towards larger θ_0. We know that the tomographic error has some dependence on r_0 from Tokovinin and Viard (2001). In Fig. 4.4 we show the parameter space of tomographic error and r_0 allowing us to understand its importance in determining the error. From the contours we observe a clear correlation between r_0 and tomographic error, obtaining a correlation coefficient of -0.56. However we also note that the spread in tomographic error for a given value of r_0 is high, particularly for small values (stronger turbulence). For example, at $r_0 = 10$ cm, 75% of profiles lie between around 120 nm and 200 nm tomographic error. The inverse is also true, for example we measure 120 nm tomographic error with r_0 values between 10 cm and 25 cm. Therefore we can confirm that, especially in strong turbulent conditions, variation in the shape of the profile is far more important than integrated strength in determining the tomographic error.

These two dimensional distributions also show us that the additional tomographic error for profiles composed of averages (average clusters, ESO 35 layer, ESO g/h/l/a) cannot be attributed to smaller values of r_0, i.e. stronger turbulence. These profiles follow the distribution in r_0 well but for any given value we obtain higher tomographic error using an average profile than we would expect. For example, the ESO 35 layer median profile has an r_0 value of 15.7 cm that coincides almost exactly with the median value from the Stereo-SCIDAR. However, the tomographic error for this profile is higher than expected at 146 nm; an additional 60 nm rms when added in quadrature from the median tomographic error of 133 nm. The single profile clusters are better distributed around the parameter space of r_0 and tomographic error and do not exhibit this bias towards higher error. There is however a noticeable lack of low r_0, high tomographic error profiles in this small set.

4.3 Discussion

We have identified two key problems regarding the choice of representative turbulence profiles. First, that while a clear correlation exists, r_0 is a poor predictor of tomographic error. Thus any profile or set of profiles designed to be representative in r_0 or seeing has no guarantee of being representative in terms of tomographic error. Second, we have found that profiles composed of averages of many measurements produce higher tomographic error than expected, given the distribution of error across all the individual profiles.

To expand on the first point we show in Fig. 4.5 two example profiles drawn from the Stereo-SCIDAR 2018A dataset. Here we select two profiles with similar r_0 but different tomographic errors. We also maintain similar θ_0 values to ensure there is no large difference in the effective height of the turbulence.

We can see that despite large variability in tomographic error from 113 to 159 nm, we are able to select two profiles that vary by less than 0.1 cm in r_0 and less than 0.1 arcseconds in θ_0. Looking at the shape of the profiles we can contrast strong

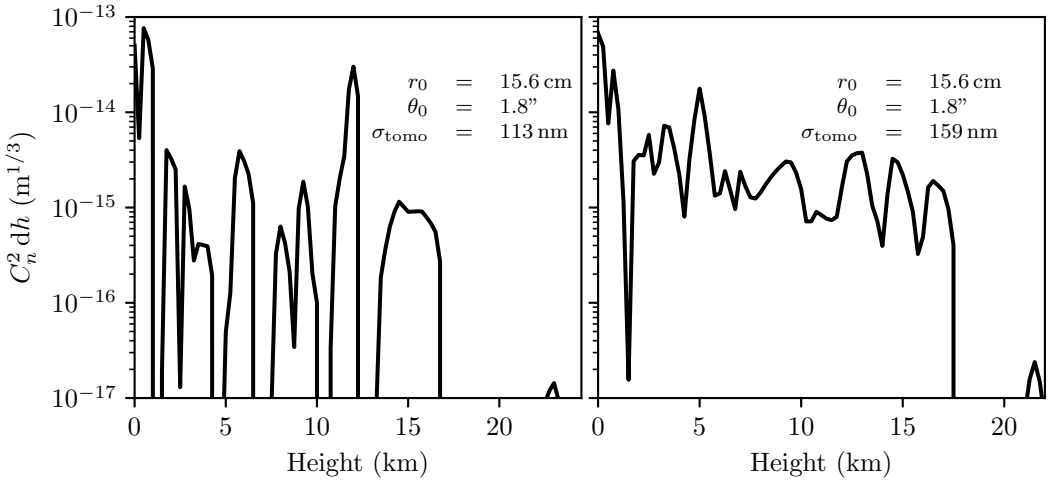

Figure 4.5: Two turbulence profiles taken from the Stereo-SCIDAR 2018A dataset with similar r_0 and θ_0 values but different tomographic error, calculated here for the 2 arcminute asterism.

thin layers of turbulence leading to low tomographic error with a less stratified profile leading to higher tomographic error. This is consistent with previous work showing that the thickness of turbulent layers is important in the calculation of tomographic error (Tokovinin and Viard, 2001; Fusco and Costille, 2010).

4.3.1 The effect of averaging profiles

It is clear that measured turbulence profiles with less stratified, more continuous distributions of turbulence result in higher tomographic error. This characteristic is shared by profiles that are constructed by averaging a large number of measurements. This is because over a large sample we observe both strong and weak turbulence at all altitudes across different individual profiles, therefore by taking an average profile we obtain a continuous distribution with some moderate level of turbulence at all heights. It is therefore possible that the higher tomographic error provided by reference turbulence profiles is a direct consequence of the averaging method employed to compute them.

Here, we quantify the effect of averaging on a small set of profiles by investigating the impact of averaging on tomographic error as well as the parameters r_0 and θ_0.

We select 50 profiles from the 2018A database that lie closest to the median values of r_0, θ_0 and tomographic error concurrently. From this set of 50 individual profiles we compute mean $\overline{C_n^2}(h, N)$ and median $\widetilde{C_n^2}(h, N)$ profiles:

$$\overline{C_n^2}(h, N) = \frac{1}{N} \sum_{i=1}^{N} C_n^2(h, i), \tag{4.2}$$

$$\widetilde{C_n^2}(h, N) = \text{median} \left(\frac{C_n^2(h, i \leq N)}{\int C_n^2(h, i \leq N)\, \mathrm{d}h} \right) (C_n^2\, \mathrm{d}h)_{\text{ref}}, \tag{4.3}$$

where N is the total number of profiles used in the average computation. Thus, for example, $\overline{C_n^2}(h, 25)$ represents the mean of the first 25 profiles in the 50 profile set. Note that in the case of median profiles, we must first divide the profile by its integrated C_n^2 then fix the integrated strength to some reference value $(C_n^2\, \mathrm{d}h)_{\text{ref}}$. The normalisation step must be taken as, unlike the mean profile, the median does not preserve the total turbulence sum. This is a consequence of the log-normal distribution of C_n^2 in each altitude bin: for this distribution the median value is always less than the mean value hence the turbulence sum always decreases, even if all profiles are normalised to the same seeing. The result is a rapid increase in r_0 and θ_0 as N increases. We choose $(C_n^2\, \mathrm{d}h)_{\text{ref}} = 3.3 \times 10^{-13}$ $\mathrm{m}^{1/3}$, the median integrated C_n^2 for the 2018A data set. This means that by definition the r_0 values of median profiles will be constant with increasing N.

In Fig. 4.6 we show how r_0, θ_0 and tomographic error evolve as N increases, i.e. as more profiles are included in our averaging. In terms of r_0 and θ_0, it is clear that a mean profile represents the profiles used to compute it well, since the values of these parameters converge to their respective median values. However, the mean profile produces a much higher tomographic error than any of its constituent profiles. After averaging only 20 profiles, tomographic error has increased from 133 nm to over 160 nm rms.

In contrast median profiles, which by design maintain a constant r_0 with increasing N, do not show as great an increase in tomographic error, reaching only around

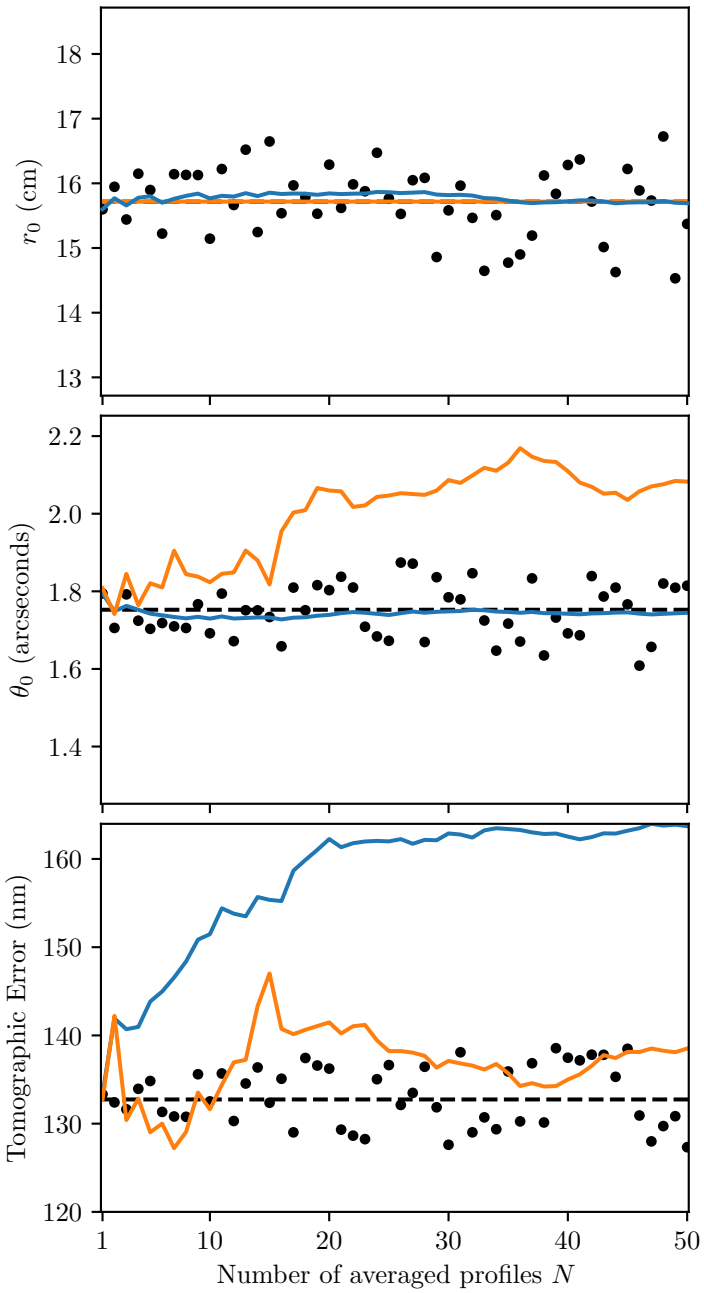

Figure 4.6: Evolution of r_0, θ_0 and tomographic error as greater numbers of profiles are averaged. The values for each individual profile $i = 1$ to 50 are indicated by black circles, with the values for mean $\overline{C_n^2}(h, N)$ and median $\widetilde{C_n^2}(h, N)$ profiles shown as blue and orange solid lines respectively. The dashed black horizontal lines indicate the median values of the respective distributions.

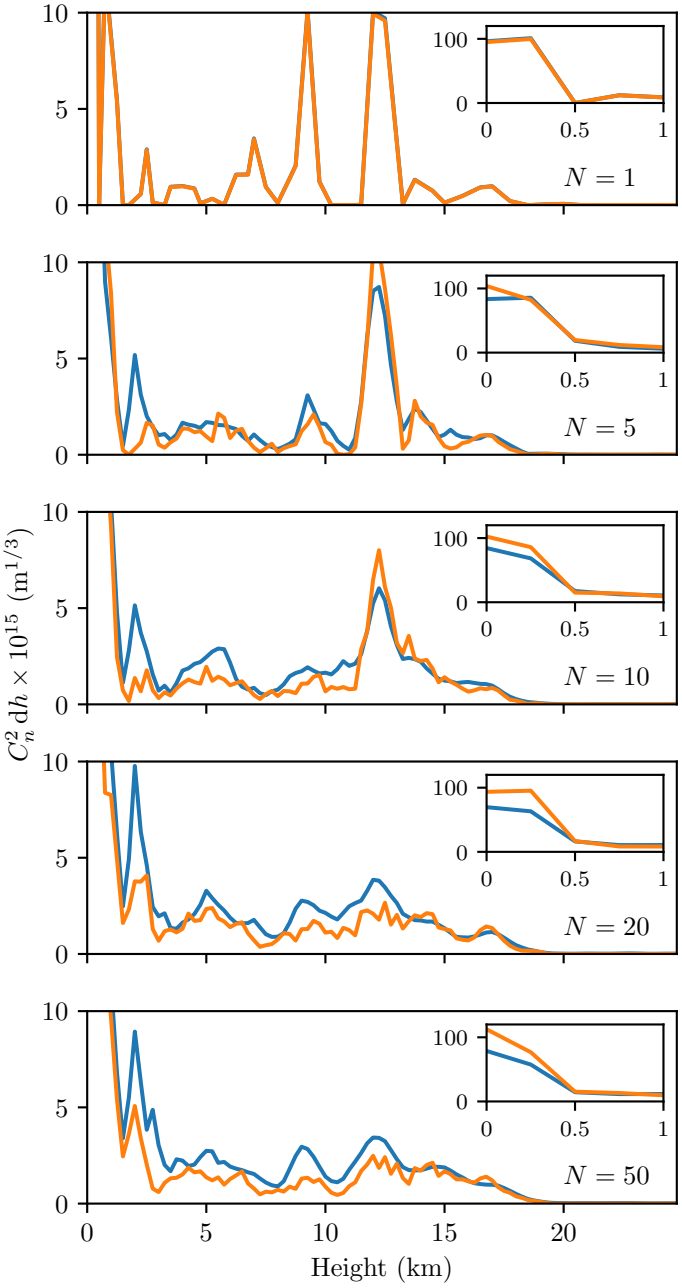

Figure 4.7: Turbulence profiles composed of averages of increasing numbers of profiles. From the upper to lower panel we show a single profile then the averages of 5, 10, 20, and 50 profiles. Mean $\overline{C_n^2}(h, N)$ and median $\widetilde{C_n^2}(h, N)$ profiles are shown as blue and orange lines respectively. Note that the y-axis scale is contracted to highlight the difference between profiles in the free atmosphere. Ground layer ($h < 1$ km) evolution for both mean and median profiles is shown in the inset axes. At $N = 1$ the two profiles are identical.

140 nm at $N = 50$. However, we now see an increase in θ_0, from 1.8 arcseconds at $N = 1$ to 2.1 arcseconds at $N = 50$.

To understand this increase it is informative to compare the profiles produced by our averaging methods. In Fig. 4.7 we show the average profiles produced with our mean and median methods for 5 values of N. It is clear in both cases that we move from strong, discrete turbulent layers to weak turbulence spread over all altitudes as N increases. However, there is a marked difference here between mean and median profiles: in taking a median profile we reduce turbulence strength in the free atmosphere and increase the fraction of turbulence in the ground layer compared to the mean profile. Indeed, at $N = 50$, we obtain a ground layer ($h < 1\,\mathrm{km}$) fraction of 62% by taking the median. This ground layer fraction falls at the 90th percentile of the distribution of ground layer fractions for the 50 constituent profiles. We are therefore producing a profile with a higher ground layer fraction than expected from an average profile, which in turn results in a larger θ_0.

High ground layer fractions are normally associated with lower tomographic error since the system is good at sensing and correcting turbulence at the ground. However, the tomographic error for the $N = 50$ median profile is still higher than almost all the constituent profiles. This is a result of the smoothing effect of the averaging process.

It is clear that for both averaging methods turbulence that is confined to stratified, strong layers in each individual constituent profile is spread over a wide altitude range. While in the case of the mean we can still maintain reasonable values of atmospheric parameters r_0 and θ_0, the effect on tomographic error is large and therefore this profile will not provide realistic performance estimates if used in simulation. For the median profile, the effect on tomographic error is smaller, but this is due to an unrealistically high ground layer fraction which may affect other aspects of the simulation such as anisoplanatism.

4.3.2 Choosing a representative turbulence profile

By averaging a number of measurements of the turbulence profile, we produce an unrealistic profile that is not representative in terms of tomographic error and, in the case of median profiles, θ_0. We therefore propose that when presented with a large database of turbulence profiles, one should select single profiles with the desired characteristics for the particular system in question. For instance, if a profile representing "median" atmospheric conditions is required, a profile should be selected that lies at the median of the distribution of tomographic error as well as the median of the distributions of r_0 and θ_0 to ensure that other errors (e.g. fitting error) are also at their respective median values. This of course requires one to compute the distribution of tomographic error for a particular instrument over the large database, but we have shown here that this may be accomplished in a feasible timescale using analytical AO simulation.

4.3.3 Extrapolation to fewer turbulent layers

Typically in Monte Carlo simulation high resolution turbulence profiles with many turbulent layers are not used since each additional simulated turbulent layer adds to the computational complexity. It has been shown that between 10 and 20 layers are required to avoid an underestimation of tomographic error by undersampling of the profile (Fusco and Costille, 2010), depending on the particular system and method used to compress the profile (Saxenhuber et al., 2017). In order for our conclusions about tomographic error to be valid in Monte Carlo simulation we therefore require that there is no significant change in error as we reduce the number of layers. In Fig. 4.8 we show how the tomographic error depends on the number of simulated layers for our comparison profiles and the distribution over all profiles. To compress the profiles we use the equivalent layers method (Fusco et al., 1999), which reduces the number of layers while maintaining the same r_0 and θ_0. We can see that in all cases for very few layers the tomographic error is greatly

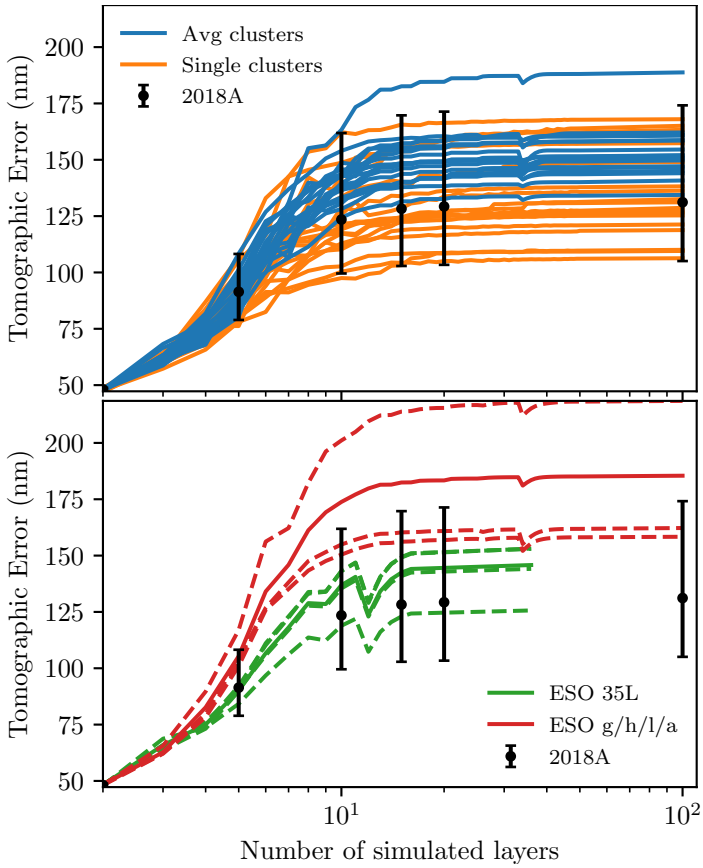

Figure 4.8: Evolution of tomographic error in the 2 arcminute LGS asterism case with the number of layers simulated. Error bars indicate the 10th and 90th percentiles of the tomographic error distribution over the 2018A dataset. Note that some instabilities in the equivalent layers compression method result in variability of the tomographic error, as is most apparent in the ESO 35 layer profiles. These instabilities only affect specific numbers of layers and can therefore be ignored.

underestimated, and the variability in tomographic error between profiles is also greatly reduced. This is understandable as it is more difficult to model a complex turbulence profile with fewer layers hence the data set becomes more homogeneous. As we increase the number of simulated layers, we see that the tomographic error begins to converge at around 10 layers, consistent with the findings of Fusco and Costille (2010). We therefore require at least 10, preferably 20 layers to sufficiently sample the turbulence profile for a 2 arcminute LGS asterism. Once we are above this threshold, the distributions of tomographic error over all of the profiles simulated are almost identical to the full 100 layer cases, and as such our conclusions drawn with 100 layer profiles are applicable to more realistic numbers of layers for

Monte Carlo simulation.

4.4 Conclusions

By employing fast analytical Fourier simulation of a simple ELT-scale tomographic AO system and a large database of Stereo-SCIDAR turbulence profiles from ESO Paranal, we have performed a statistical study of tomographic error over a wide range of circular 6 LGS asterisms.

We find that the tomographic error across the whole data set follows an approximately log-normal distribution, with the median and spread increasing with asterism diameter. However, further analysis shows that the tomographic error scales differently with asterism diameter for each individual profile in the data set. This means that a profile providing e.g. median error for one asterism may not necessarily be considered a median profile for other asterisms.

Our findings are consistent with previous work regarding the influence of r_0 on the tomographic error — there is a moderate negative correlation between r_0 and tomographic error. However, particularly for small values (stronger turbulence) the spread in computed values of tomographic error can be very large. Therefore especially in strong turbulence conditions the shape of the profile becomes of primary importance in determining the tomographic error. We observe that profiles with strong, thin layers lead to smaller error whilst more continuous distributions of turbulence lead to higher tomographic error.

After computation of the distribution of tomographic error across all 10,691 profiles, we are able compare to small sets of profiles used in E2E simulation. We find that the ESO 35 layer, good/high/low/all and average clustered profiles are all pessimistic in terms of tomographic error to different extents. Taking as an example the 2 arcminute asterism, we find that the ESO 35 layer median and ESO all profiles result in around 60 and 130 nm additional rms error respectively when compared to the median error of the distribution of 10,691 profiles. Single profile clusters did

not exhibit this bias toward higher error and perform best in terms of representing the distribution of tomographic error.

We note that the small sets of profiles providing higher tomographic error than expected are composed of averages of many measurements of the profile. By selecting 50 profiles from the dataset with similar r_0, θ_0 and tomographic error values and cumulatively averaging them we observe a transition from a profile with strong thin layers to a continuous average profile associated with high tomographic error. We find that mean profiles are representative of their constituent profiles in r_0 and θ_0 but rapidly increase in tomographic error. Median profiles do not increase as much in tomographic error but produce a much larger ground layer fraction than their constituent profiles and therefore larger, unrepresentative θ_0.

Finally it was shown that the distributions of tomographic error computed for high resolution 100 layer profiles do not change when the number of layers simulated is reduced to more reasonable numbers for Monte Carlo simulation (fewer than 35 layers). We do not find any significant change of the tomographic error distribution for greater than 10 layers in the 2 arcminute LGS diameter case.

We propose that if profiles that are representative in terms of tomographic error are required from a large database, single profiles should be selected from this database rather than average (mean or median) profiles. These single profiles should be selected such that they exhibit the desired error characteristics (e.g. good, median or bad tomographic error) for the given system parameters, including the guide star asterism. Fast analytical AO simulation such as has been employed here is therefore required in order to compute the distribution of tomographic error for this system across the large database such that these single profiles may be selected. Selecting a single profile in this way ensures that the characteristics of the turbulence profile as seen by the AO system are preserved, and thus any more detailed E2E simulations using this profile will produce realistic performance estimates.

5

Limitations imposed by profile structure and evolution on tomographic reconstruction

Note: this chapter is an adaptation of Farley et al. (2020)

5.1 Introduction

It is important for the science goals of ELTs that tomographic AO systems operate to the fullest extent of their capability: applying the best possible atmospheric correction in the given conditions. Building on the work in chapter 4, in this chapter we employ the same turbulence profile database and analytical tomographic AO simulation. Here, rather than identifying profiles that are representative of the data set for the purposes of accurate simulation, we investigate effects of the profile on tomographic reconstruction from an operational point of view. More specifically, the effect of not knowing the "true" profile. This could be because we may reconstruct only N discrete layers in our system, or because the profile has evolved since it was last measured.

The responsibility for maintaining optimal correction lies with the soft real time control (SRTC) system or supervisor, which takes telemetry (WFS measurements) from the AO system and maintains an up-to-date tomographic reconstruction matrix. The two key pieces of information to compute this matrix or reconstructor are the system geometry, i.e. relative positions of NGS/LGS, and the optical turbulence profile.

The computation performed by the SRTC usually consists of two stages. First, the turbulence profile $C_n^2(h)$ and other atmospheric parameters such as the outer scale $L_0(h)$ are obtained by fitting measured WFS measurements from the AO telemetry through a variant of the SLODAR technique (Wilson, 2002; Gilles and Ellerbroek, 2010; Cortés et al., 2012; Vidal et al., 2010). The profile, which is comprised of N discrete layers, must be of sufficient fidelity to model the true continuous $C_n^2(h)$ profile. Also, since the turbulence is a random statistical process, we must average WFS measurements over a time period δt in order for the statistics to converge (Martin et al., 2012). During this time we must assume that the profile is stationary.

Depending on the method, the time taken to perform this fitting procedure can depend on the number of WFS measurements as well as the number of reconstructed layers N (Gratadour et al., 2018). This dependence can be alleviated by fitting a fixed number of reconstruction layers and using only the WFS measurements containing the most information about the profile (Laidlaw et al., 2019).

These parameters, including the discrete turbulence profile, are then used in the computation of the tomographic reconstruction matrix, which differs depending on the AO configuration. If there are altitude conjugated DMs as in MCAO, then the full turbulence volume must be explicitly reconstructed onto the N reconstruction layers (Fusco et al., 2001). The computation time therefore depends on both the number of WFS measurements and N. If there are no altitude conjugate DMs, as is the case in LTAO, GLAO and MOAO, the turbulent volume need only be implicitly reconstructed (Vidal et al., 2010), in which case the computation depends only on the number of WFS measurements and system specific parameters such as the

number of targets for MOAO.

The large number of WFS measurements at ELT scales (up to 90k WFS measurements in total) makes both of these stages computationally expensive, and as such efforts have been made to accelerate the SRTC using both GPU and CPU architectures (Gratadour et al., 2018), as well as applying novel numerical techniques to speed up the computation (Ellerbroek, 2002; Doucet et al., 2018). It is not only the raw computational power of the SRTC that may limit this computation time. Many of the matrices involved may be precomputed offline, in which case they are stored in a database which must be accessed and the data loaded before computation. While this reduces the computational overhead, these matrices can be up to multiple terabytes in size (Arcidiacono et al., 2018) and this could therefore place constraints on other areas of the SRTC such as the memory.

Both the system geometry and the turbulence profile are temporally evolving and together they constrain the rate at which the SRTC must update the reconstructor Δt. Over the course of an observation, the geometry of the tomographic problem changes since NGS move in the field of fixed LGS due to field rotation. Additionally, as the pointing angle of the telescope changes the heights of turbulent layers also change with airmass. The turbulence profile itself in the free atmosphere is essentially a meteorological phenomenon and it varies on similar timescales to weather: from long-term seasonal changes to unpredictable variation on timescales as small as several minutes.

For a particular observation, the effects of changing system geometry are mostly predictable and as such their impact on AO performance and therefore requirements for the SRTC can be estimated. This is not the case for the effect of the changing turbulence profile, where changes are random and unpredictable in nature. Assessment of the impact of sub-optimal reconstruction due to an evolving profile is more difficult since we must use a large number of turbulence profiles and assess the impact on the tomographic error statistically for a particular site. This is not feasible with conventional Monte Carlo AO simulation which requires long

computation times for a single profile.

Previous work has studied the effect of sub-optimal tomographic reconstruction with limited sets of turbulence profiles. It has been shown, using 11 high resolution turbulence profiles measured from balloon flights at Paranal, that the number of layers required to maintain good performance is between $N = 10$ and $N = 20$, depending on the LGS asterism diameter (Fusco and Costille, 2010). It has also been shown that using more advanced compression methods can reduce this number further (Saxenhuber et al., 2017). Temporal effects have been investigated using a limited set of real turbulence profiles from La Palma by Gendron et al. (2014). They showed that the reconstructor should be reoptimised on timescales of $\Delta t = 10$ minutes and that the minimum averaging time should be at least $\delta t = 5 - 10$ minutes.

Here, we employ a large database of 10,691 high-resolution, high-sensitivity optical turbulence profiles measured by the Stereo-SCIDAR instrument at ESO Paranal, Chile (Shepherd et al., 2014; Osborn et al., 2018). By coupling these real turbulence profiles with fast analytical tomographic AO simulation, we assess the impact of sub-optimal reconstruction on the tomographic error in a statistical manner. This allows us to draw robust conclusions as to the number of required reconstruction layers N, the reconstructor update period Δt and averaging time δt for the Paranal observatory. By taking two contrasting nights, where the variability in the profile is markedly different, we also investigate the effect of different temporal optimisation strategies. We dimension our simulations according to the ELT currently under construction atop nearby Cerro Armazones which will employ multiple tomographic AO systems (Neichel et al., 2016; Diolaiti et al., 2018; Morris et al., 2016).

5.2 Simulation

Simulation parameters are maintained from chapter 4, i.e. an LTAO configuration with fixed parameters summarised in Table 4.1.

In most cases, we will compare tomographic error in the optimal case, where the profile is known perfectly, to the case where the reconstructor is sub-optimal. We will use the quantity E, the difference in quadrature between the tomographic error σ_{tomo} with sub-optimal parameters and the optimal case, i.e.

$$\begin{aligned} E(N, t - t_{\text{opt}}, \delta t) = &\big[\sigma^2_{\text{tomo}}(N, t - t_{\text{opt}}, \delta t) \\ &- \sigma^2_{\text{tomo}}(N = 100, t - t_{\text{opt}} = 0, \delta t = 0)\big]^{1/2}, \end{aligned} \tag{5.1}$$

for N the number of reconstructed layers, $t - t_{\text{opt}}$ the time since the previous reconstructor optimisation and δt the time over which the profile is averaged at each reconstruction step. Therefore a value of $E = 0$ occurs when the profile is known perfectly, and any increase corresponds to the additional incurred tomographic error with a sub-optimal reconstructor.

It should be noted that the baseline optimal reconstructor averaging time is not 0 but some finite time δt_{min} since turbulence profiles are themselves measured from a temporal average of measurements. For the Stereo-SCIDAR at Paranal, $\delta t_{\text{min}} \approx 140$ s. For the purpose of our analysis we must assume that there is no significant difference in tomographic error between $\delta_t = 0$ and $\delta_t = \delta t_{\text{min}}$.

It is not only the increase in tomographic error from the optimal case that is of interest. At the other end of the scale, a useful quantity is the worst case performance. We define this as the tomographic error obtained if we ignore the variability of the atmosphere, and choose instead to precompute our tomographic reconstructor with a single turbulence profile. We have several options when selecting this profile. The absolute worst performance is obtained if we have no a priori information about the profile at all, which corresponds to an optimisation profile of constant $C_n^2(h)$. Unfortunately, performance with this profile is so poor (median values of E between 160 and 520 nm rms depending on the LGS asterism diameter) that it does not provide a useful benchmark with which to compare our results — regardless of our reconstructor parameters we always perform better than this.

A more reasonable prior for the turbulence profile is the 35 layer profile defined

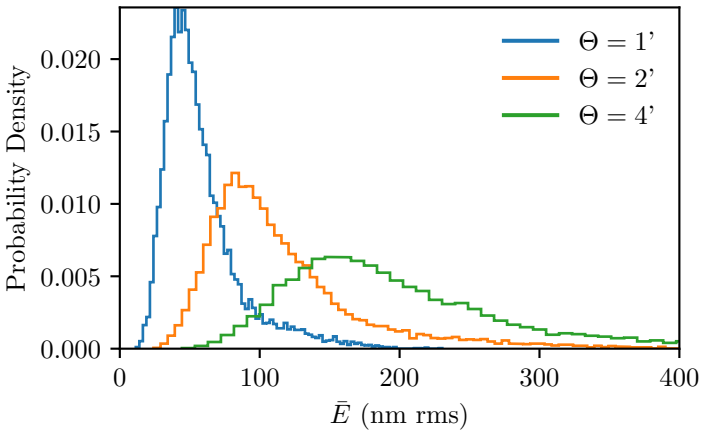

Figure 5.1: Distributions of $\bar{E}$ across the Stereo-SCIDAR 2018A data set obtained if we use only a single reconstructor computed with the ESO 35 layer profile, for 1, 2 and 4 arcminute LGS asterisms.

Θ	$\mathbf{P}_5$	$\mathbf{P}_{25}$	$\mathbf{P}_{50}$	$\mathbf{P}_{75}$	$\mathbf{P}_{95}$
1 arcmin	27	40	51	67	118
2 arcmin	55	79	101	135	234
4 arcmin	100	143	184	246	425

Table 5.1: Percentiles P_i of the distributions of $\bar{E}$ shown in Fig. 5.1. Units are nm rms.

by ESO (Sarazin et al., 2013). This profile is designed to represent median conditions at Paranal and is often used in ELT simulations. In Fig. 5.1, we show the distributions of E obtained if we optimise using this profile, which we denote $\bar{E}$. Quartiles of the distributions of $\bar{E}$ are also listed in Table 5.1. Similar distributions are obtained if we instead use a median or mean profile over the 2018A dataset. We therefore conclude that these distributions represent approximately the best possible performance obtainable for a single profile reconstructor that is never updated.

We focus on the tomographic error to maintain generality, however of course the overall performance of a tomographic AO system is defined by the sum of all error terms. Whether the performance impact of our worst case in Fig. 5.1 is important will depend on the magnitude of these additional errors. Many of these errors will be highly system specific and as such it would not be meaningful to include them here since we must make many assumptions as to the parameters of

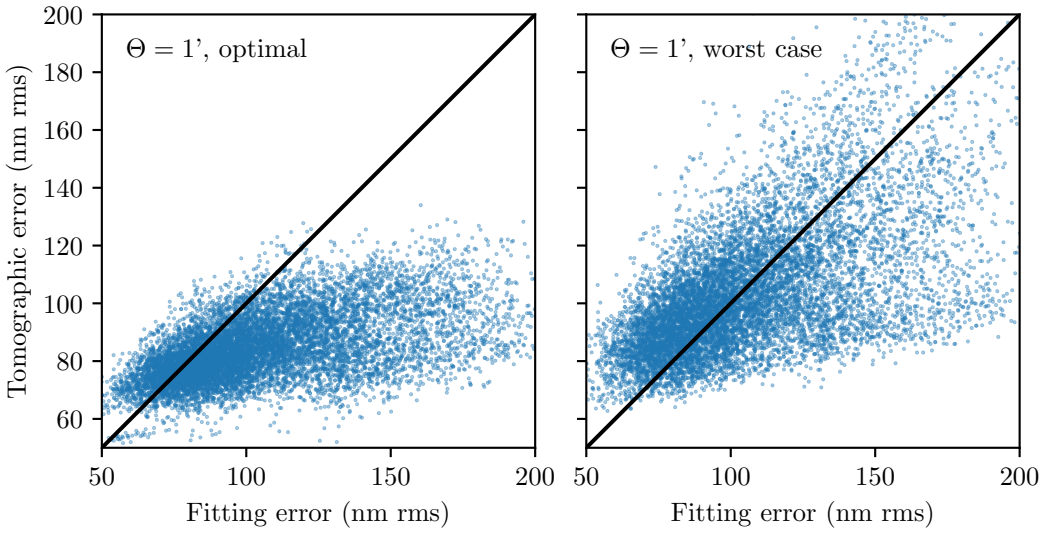

Figure 5.2: Tomographic error vs. fitting error for 1 arcminute LGS asterism, in the cases where the reconstructor is optimal (left) and the worst case (right). Each dot corresponds to one turbulence profile in the 2018A dataset. The black line corresponds to the case where the two errors are equal.

AO systems still in the design phase. However, in order to give some context to the values of tomographic error we can compute and compare to the DM fitting error over the 10,691 profiles. The fitting error can be computed (see section 2.3.6) as $\sigma^2_{\text{fitting}} = 0.23(\Delta/r_0)^{3/5}$ for Δ the projected DM pitch and r_0 the Fried parameter (Rigaut et al., 1998) and describes the inability of the DM to correct high order turbulent modes. We compute this using an assumed $\Delta = 0.5$ m for the ELT, and compare to the tomographic error for an LGS asterism diameter of 1 arcminute, which corresponds to the narrow field LTAO case where these two errors are most likely to be the largest contributors. We can see in Fig. 5.2 that when the tomographic error is optimal, we are usually dominated by the fitting error, and the tomographic error dominates for only around 20% of profiles. In the worst case this increases to over 50%. By ensuring the reconstructor is optimised we can greatly improve the tomographic error when it is poor in the worst case (> 100 nm rms), ensuring that it is smaller than the fitting error for most profiles.

For systems with larger LGS asterisms the absolute gain from optimising the reconstructor will be greater as can be seen in Table 5.1 and Fig. 5.1, however this

may be cancelled out by larger additional error terms, for example generalised fitting in the MCAO case. As these systems are developed the values of E computed throughout this work may be compared to the magnitude of these system specific errors to determine the extent to which the turbulence profile may limit performance.

5.3 Number of reconstructed layers

In any tomographic AO system, the atmosphere is modelled as a number N of discrete turbulent layers. Since in reality the turbulence profile is a continuous function of height h, the accuracy of this model for a given profile depends on the number of layers and their altitudes. If the number of layers is too few or their altitudes incorrect, we induce a model error which results in an increase in tomographic error. The amount of model error induced by modelling the profile with N layers will depend on the system geometry (e.g. LGS positions) as well as the profile itself – profiles with strong, discrete turbulent layers lend themselves to modelling with a smaller number of layers whereas more continuous distributions of turbulence require a greater number of layers to achieve the same model error.

The input profiles from the Stereo-SCIDAR are of very high resolution, with $N = 100$ altitude bins between the ground and 25 km. We can assume that these profiles provide a very good model of the continuous $C_n^2(h)$ profile and may therefore be used directly in our analytical simulation to provide our optimal case.

The profiles obtainable by the SLODAR-type analysis of ELT WFS measurements will have a maximum resolution approximately equivalent to that of the Stereo-SCIDAR (Vidal et al., 2010). However for MCAO in particular, reconstructing such a large a number of layers poses an SRTC challenge. The computation of the reconstructor depends on the explicit projection of the turbulence measured by each WFS onto the N reconstruction layers. This means that matrices which are already large (of dimension up to 90k $\times$ 90k) must be generated N times and mul-

tiplied together. Alternatively if the geometry may be fixed, such as by separating NGS and LGS control (Gilles and Ellerbroek, 2008) and fixing the reconstruction layer altitudes, some of these large matrices may be precomputed and stored in a database. In this case the limiting factors may not only be the computing power but the speed at which the SRTC can retrieve and multiply these huge matrices (Arcidiacono et al., 2018).

For other forms of tomographic AO without altitude conjugate DMs, there is no explicit reconstruction of the N layers hence the computation of the reconstructor itself does not depend on the number of layers. However, the turbulence profile must still have sufficient layers to avoid model error. Depending on the specific method used to fit the $C_n^2(h)$ profile from WFS measurements, the number of layers may still be a factor in determining the reconstructor update time for these systems (Gratadour et al., 2018; Laidlaw et al., 2019). There is also interest from the perspective of simulating these systems as to the minimum number of layers required to model the atmosphere.

Here we probe the effect on tomographic error of reconstructing $N \leq 20$ turbulent layers, whilst maintaining the atmosphere at full 100 layer resolution. We compare cases where the altitudes of the small number of layers are allowed to vary to the case where the altitudes are fixed. The high resolution profiles are compressed using three methods. Firstly we employ the equivalent layers method described in Fusco et al. (1999). In this method, the turbulence profile is split into N slabs, with the $C_n^2(h)$ values for each layer being the integral of $C_n^2(h)\,\mathrm{d}h$ in each slab. The height of each layer is then set to the mean effective height $\bar{h} = [\int C_n^2(h) h^{5/3}\,\mathrm{d}h \,/\, \int C_n^2(h)\,\mathrm{d}h]^{3/5}$ of the layers in each slab. This has the effect of reducing the number of layers whilst conserving the isoplanatic angle θ_0.

The second compression method we use here is the optimal grouping method described in Saxenhuber et al. (2017). This method was shown in end-to-end AO simulation with a limited set of turbulence profiles to give better performance than many other compression methods including equivalent layers. This method is more

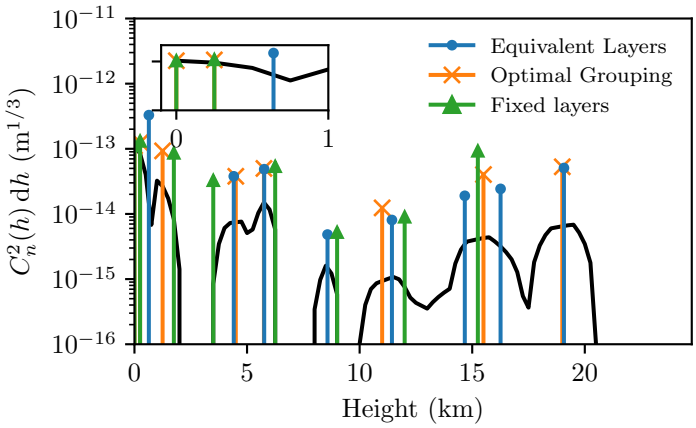

Figure 5.3: Use of the equivalent layers, optimal grouping and fixed layer methods to compress a high resolution Stereo-SCIDAR profile (black) measured on the night of the 8th May 2017. We compress from 100 layers to $N = 8$ layers. Inset axis shows the detail in the ground layer ($h < 1$ km).

computationally demanding, and involves the minimisation of the cost function

$$F = \sum_{l=1}^{N} \sum_{k \in G_l} C_n^2(h_k)|h_k - h_l| \tag{5.2}$$

where k runs over a particular grouping of turbulent layers G_l.

Finally, we consider the case where we fix the N reconstruction altitudes. These fixed altitudes are decided by optimal grouping compression of the average 2018A profile. This is essentially a simple re-binning of the C_n^2 profiles.

Application of these compression methods to an example profile can be seen in Fig. 5.3. We can see that at some altitudes the layers from the methods overlap, whereas at other altitudes there is a disagreement between them. We perform this compression for all profiles in the 2018A data set for N between 2 and 20 layers.

In Fig. 5.4 we illustrate how the tomographic error decreases as the number of layers reconstructed is increased for our 1, 2 and 4 arcminute LGS asterisms. We show here the spread of the distributions of $E(N)$ that result from the variation of the turbulence profile over the measurements in the 2018A data set. It is immediately obvious that wider asterisms require a greater number of layers to be reconstructed to reach the same level of error. In addition the spread of the distribution increases with larger asterisms. The optimal grouping and equivalent layers

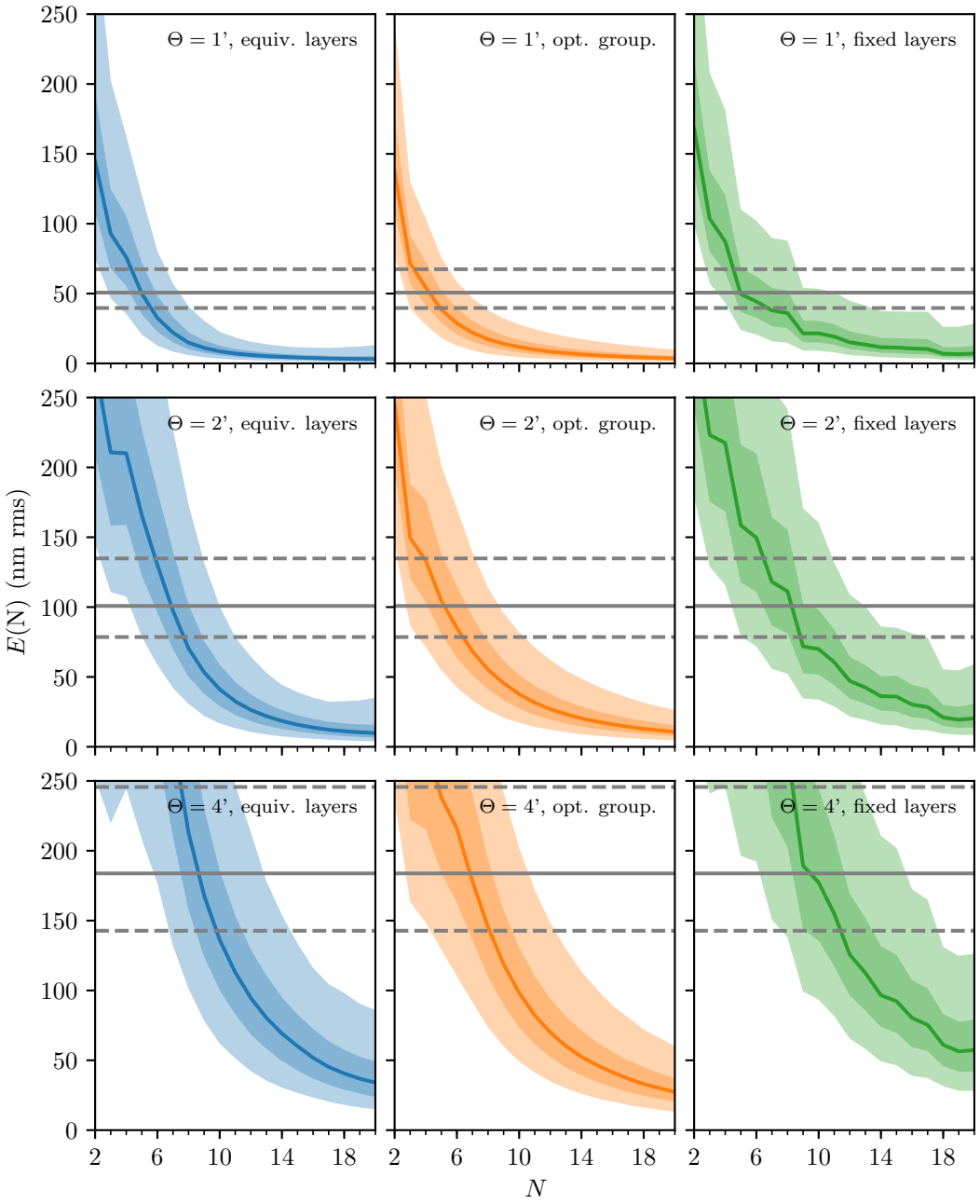

Figure 5.4: Tomographic error increase E as a function of the number of reconstructed layers N. From upper to lower panels: 1, 2 and 4 arcminute diameter LGS asterisms. From left to right panels: equivalent layers, optimal grouping and fixed layer profile compression (blue, orange and green). In all panels the solid line indicates the median of the distribution over the 10,691 profiles. Darker shaded region indicates the interquartile range and lighter shaded region the 5th - 95th percentile range. Horizontal lines represent median, lower and upper quartiles of the worst case distribution of $\bar{E}$.

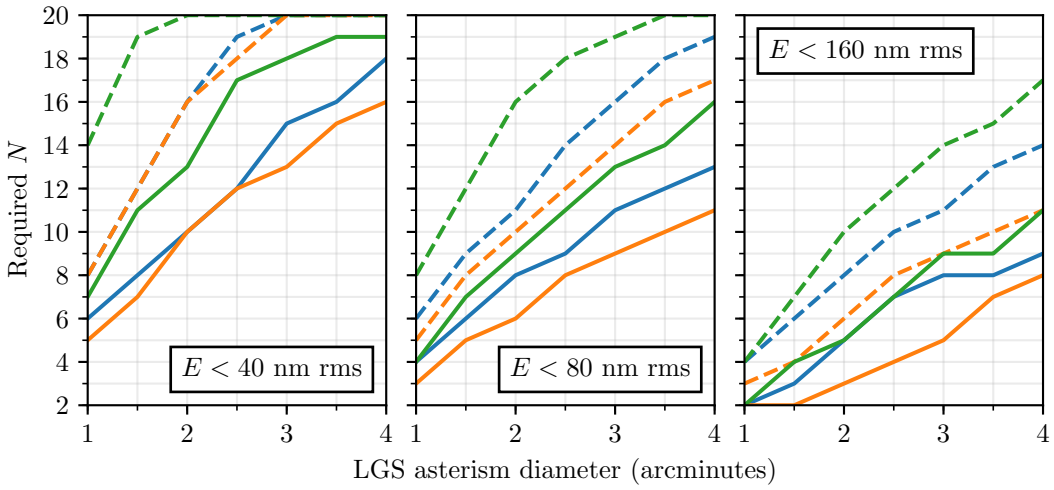

Figure 5.5: Number of layers required to maintain the increase in tomographic error below a tolerated threshold, with increasing LGS asterism diameter. From left to right: increasing error thresholds, indicated in the corners of each panel. Blue represents profiles compressed with the equivalent layers method, orange are profiles compressed with the optimal grouping method and green are fixed layers. Solid line indicates the median and the dashed line the 95th percentile of the distributions over the 10,691 profiles for each asterism diameter.

methods show similar increases in tomographic error, with a slight advantage for the optimal grouping method for small N. In the 1 arcminute asterism case, we can reconstruct as few as 5 equivalent layers or 4 optimal grouping layers before the tomographic error reaches the worst case distribution $\bar{E}$. For fixed layers, the increase in tomographic error is larger as would be expected since the heights of the reconstruction layers are no longer matched to the current profile. This is most apparent in the 95th percentile of E which is higher than for equivalent layers. This shows that there are a small set of profiles representing around 5% of profiles where using these fixed layers gives a particularly bad fit.

The exact number of layers required depends on the error increase that can be tolerated for a particular system. In Fig. 5.5 we show the distributions of the number of layers required to meet different error thresholds. Here we have additionally computed the number of layers required for some intermediate LGS asterisms as well as for 1, 2 and 4 arcminutes to better show the behaviour with increasing asterism diameter. If we tolerate a higher level of error, we are able to reconstruct

fewer layers, and the optimal grouping method consistently allows between 1 and 4 fewer layers to be reconstructed depending on asterism diameter. The variability of turbulence profile can result in a large variability in the number of layers required. At larger asterism diameters there can be as much as a 5 layer difference between the median number of layers required and the 95th percentile.

5.4 Temporal reconstructor optimisation

5.4.1 Tomographic error degradation over time

The tomographic reconstructor is computed using knowledge of both the system geometry and turbulence profile. If either of these change, the reconstructor will no longer be optimal and tomographic error will increase.

Over the course of an observation, usually around one hour, several changes may occur in the geometry of the system as the telescope tracks the target across the sky. NGS, which must be used to recover wavefront tip-tilt information, may move with respect to the LGS due to field rotation. We do not consider errors of this type here since they are highly system specific.

As the telescope zenith angle γ changes, the angle at which the turbulence profile is viewed also changes, with the effective altitudes of each turbulent layer changing according to airmass $\sec\gamma$. The level of this error over an observation will depend on the target altitude, however we show best and worst cases over a 1 hour observation in Fig. 5.6. We can see that when observing near zenith, the error is very small and always less than 20 nm rms in the 1 arcminute asterism case. This is contrasted by the case where we observe far from zenith and as a result the change in airmass is large. Here we see large increases in tomographic error of the order of 100 nm after 1 hour. This error can be removed for an LTAO system by modifying the LGS asterism diameter in order to maintain constant geometry (Neichel et al.,

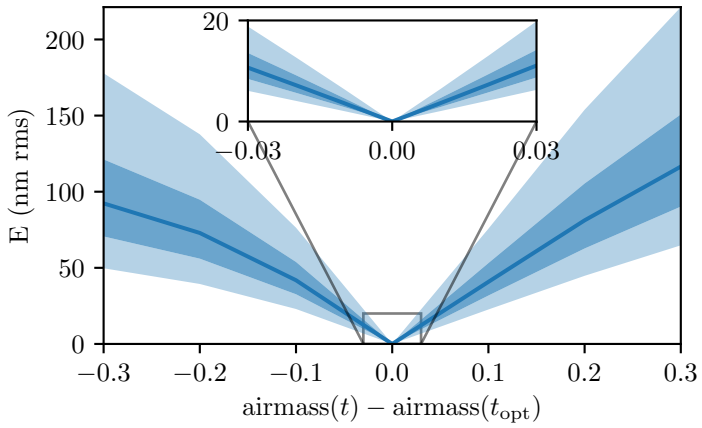

Figure 5.6: Increase in tomographic error with change in airmass over the course of a 1 hour observation if the reconstructor is not updated. We have simulated here only the 1 arcminute LGS asterism. Solid line indicates the median, darker shaded region the interquartile range and lighter shaded region the 5th - 95th percentile range over the 10691 profiles. The reconstructor is optimal at the origin ($t = t_{\text{opt}}$), and we show the cases of both rising (negative change in airmass) and setting (positive change in airmass) targets. Primary axes show the worst observing far from zenith where the airmass changes considerably (± 0.3) over the observation. The inset axis shows a best case where the observation is near zenith and the change in airmass is 100 times smaller (± 0.03).

2016). The specific implications for the tomographic error will depend on telescope observation patterns and is beyond the scope of this work.

We consider here the case where the telescope will be observing near zenith and as such the increase in error over time from changing airmass is small. What remains is the effect of the temporal evolution of the turbulence profile itself. Unlike the temporal errors above, this is not predictable over the course of an observation since the evolution of the profile is a meteorological phenomenon.

In some cases, as illustrated in Fig. 5.7, the profile may change dramatically from the profile that the reconstructor was last optimised with, leading to a large increase in tomographic error. In this particular example, at 03:00 UT the optimisation profile contains some weak high altitude layers above 10 km. After only a few minutes, a very strong layer appears at 5 km, resulting in an increase in tomographic error from around 90 nm to 110 nm. This is followed at approximately 03:30 UT by a strong layer at 15 km, pushing up the tomographic error to 150 nm rms.

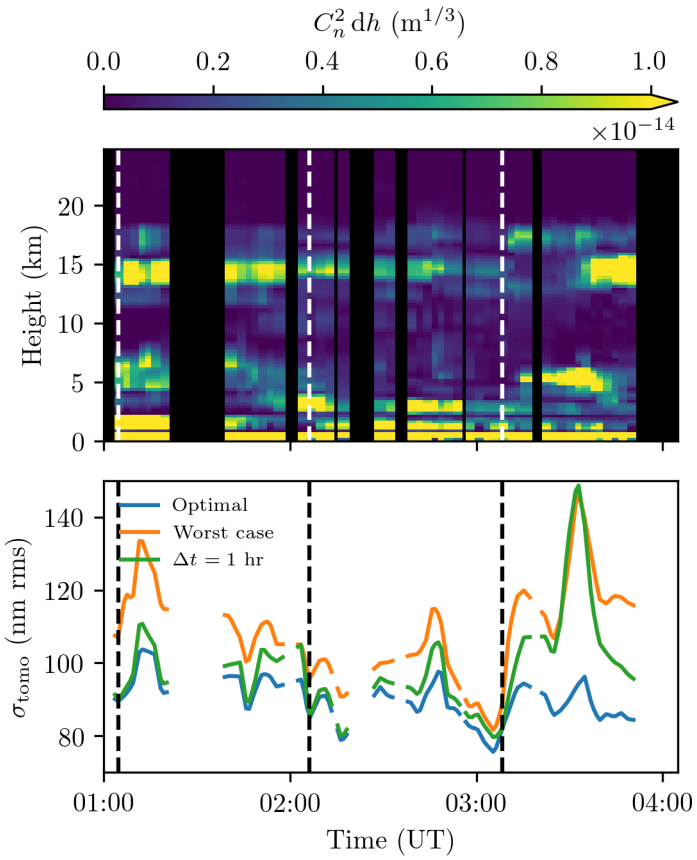

Figure 5.7: *Upper*: Sequence of approximately 3 hours of Stereo-SCIDAR profiling data from the night of the 8th July 2017. The $C_n^2\,\mathrm{d}h$ colour scale is clipped at 10^{-14} to emphasise high altitude layers. *Lower*: Corresponding tomographic errors for the 1 arcminute asterism. In blue we show the optimal case where the profile is always perfectly known. In orange, the case where we do not update the reconstructor, and optimise only using the ESO 35 layer profile. Finally in green the tomographic error in the case when we update the reconstructor once per hour. Reconstructor optimisation times are indicated by vertical dashed lines.

While this is an extreme example, the longer the time period between reconstructor optimisations the more likely it is that the atmosphere will change and performance will suffer.

To investigate this more generally, we update the reconstructor once per hour over all 10,691 profiles in the dataset and ascertain the statistical behaviour of E with increasing time since optimisation $t - t_{\mathrm{opt}}$. We show these results in Fig. 5.8.

The shape of the distributions over time are very similar for each LGS asterism, with larger absolute values of E for increasing asterism diameter. Most of the

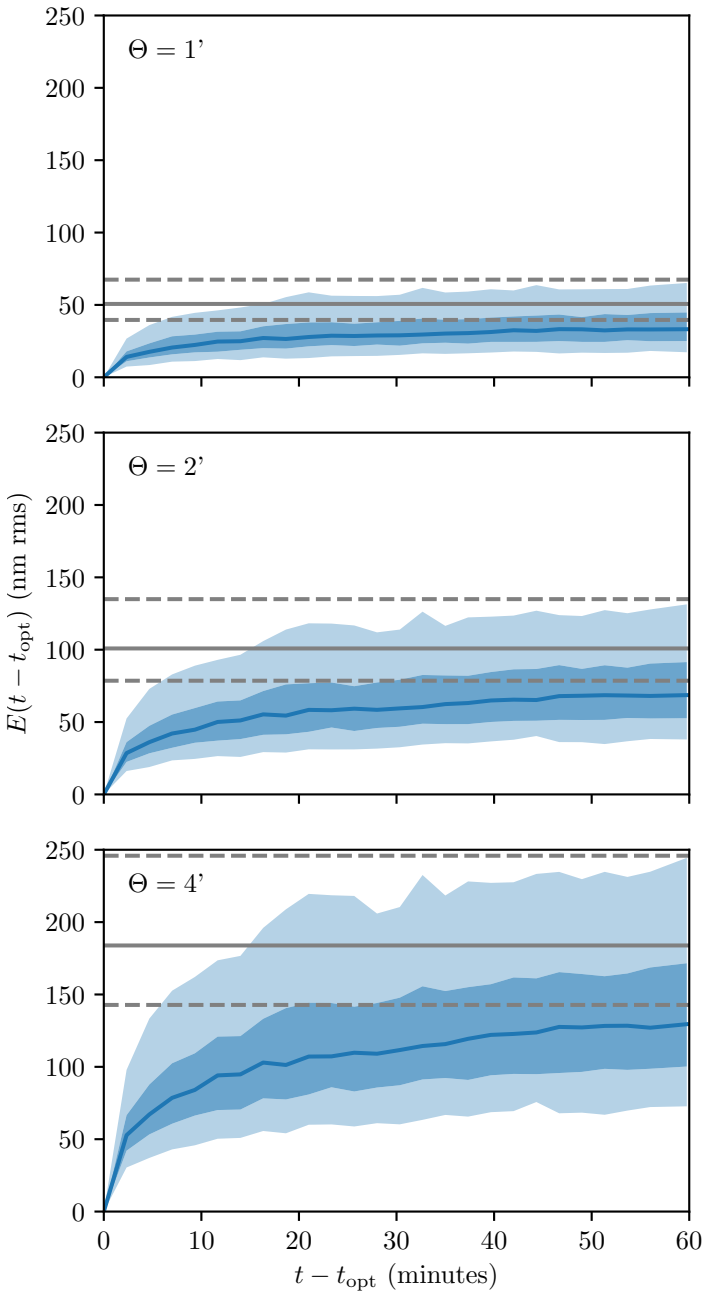

Figure 5.8: Tomographic error increase with increasing time since tomographic reconstuctor optimisation $t - t_{\mathrm{opt}}$. From upper to lower panel: 1, 2 and 4 arcminute LGS asterisms. The solid line indicates the median of the distribution over the 10 691 profiles. Darker shaded region indicates the interquartile range and lighter shaded region the 5th - 95th percentile range. Gray solid and dashed lines represent median and interquartile range of worst case distribution $\bar{E}$ for each asterism (Tab. 5.1).

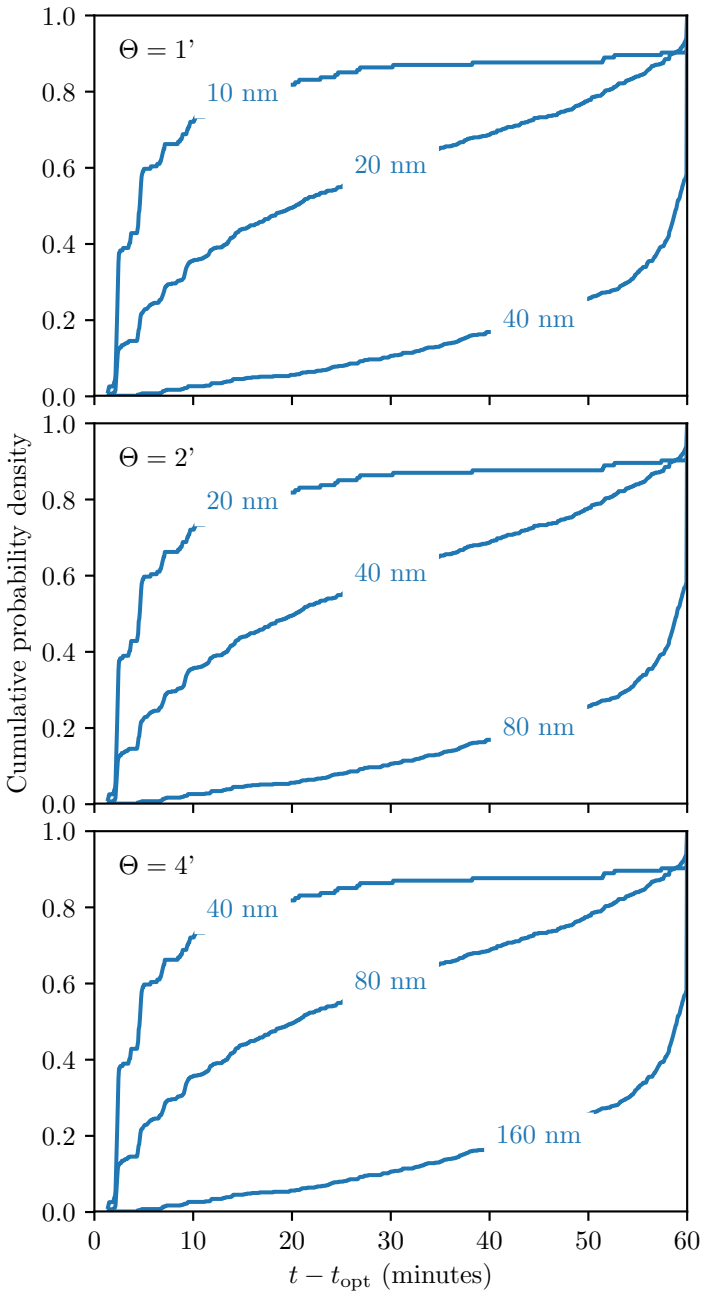

Figure 5.9: Cumulative probability distributions describing the time since the last optimisation step $t - t_{\text{opt}}$ at which the increase in tomographic error reaches some threshold. From upper to lower panel: 1, 2 and 4 arcminute LGS asterisms. Each line is labelled with its E_{crit} threshold.

additional tomographic error occurs on average in the first 10 to 20 minutes after optimisation of the reconstructor. After this point, the percentiles of the distribution plateau and there is a smaller increase for the remaining 40 minutes before the next optimisation step. After 60 minutes, the distributions do not reach the level of $\bar{E}$ as shown by the horizontal lines therefore it is always better to optimise using a recent profile as opposed to a precomputed reference profile.

With the same data, we may also calculate another interesting set of distributions. If we wish to limit the tomographic error to some fixed increase $E < E_{\text{crit}}$, we can calculate for each optimisation period the time at which we reach this threshold. In Fig. 5.9, we show that this time depends on the chosen error threshold and the LGS asterism diameter. As one would expect from the wide distributions in Fig. 5.8, the time at which we meet this error threshold can vary dramatically. Taking for example the 1 arcminute asterism, we find that in the median case we reach an error threshold of $E_{\text{crit}} = 20$ nm rms in approximately 20 minutes. However across the data set this time ranges from less than 5 minutes (around 10% of profiles) to over 1 hour (around 5% of profiles). This makes it difficult to select a single optimisation period Δt.

5.4.2 Reconstructor averaging time

Fitting the turbulence profile to WFS measurements requires the average of many measurements, to minimise statistical noise and to ensure the convergence of covariance matrices (Martin et al., 2012). During this averaging time the profile is assumed to be stationary however we know that sudden changes to the profile can occur on timescales of minutes. The profile measured by the system is therefore the mean over the averaging time (Gendron et al., 2014). It has been shown that averaging profiles on a large scale (i.e. entire datasets) produces unrealistic continuous distributions of turbulence that provide poorer tomographic error than expected (Farley et al., 2019, also chapter 4).

This averaging effect will result in an immediate degradation in performance, since the profile is no longer matched to the current profile at time $t = t_{\text{opt}}$. However, an additional consequence of the averaging is more stable performance over time. If for example the profile behaves strangely during the few minutes when the reconstructor is being optimised this can lead to a sudden performance hit when the profile returns to normal. This is less likely if the averaging time at each optimisation is longer.

There is therefore a trade-off between absolute performance, which will deteriorate as we average over greater timescales, and more constant performance over time which could result in better performance over longer timescales. The overall effect on the tomographic error will depend on how much the profile changes over the course of an update period, so it is clear that δt will be linked to Δt. Note that we are only taking into account changes in the profile here, and we do not take into account other effects that temporal averaging has on the reconstructor such as better estimation of WFS covariance matrices, leading to a more accurate reconstructor. In reality, these effects would more likely determine the averaging time δt.

We perform similar analysis to Section 5.4.1, updating the reconstructor once per hour over the 10,691 profiles. At each optimisation step, instead of using the most recent profile, we optimise on the average of profiles from the time $t_{\text{opt}} - t \leq \delta t$ with values of δt ranging from 10 minutes to 60 minutes in 10 minute steps. There are cases where there are very few measured profiles in the timeframe $t_{\text{opt}} - t \leq \delta t$, for example at the beginning of each night. To avoid biasing the results the data from these particular cases is removed from the subsequent analysis. In the worst case this filtering removes approximately 40% of the data, leaving 6545 profiles which is still a large enough sample for our statistical analysis.

We present the results of this analysis in Fig. 5.10. For clarity we show only the median behaviour of $E(\delta t)$, but the distribution across the data set follows similar patterns. This behaviour is quite clearly dependent on the reconstructor

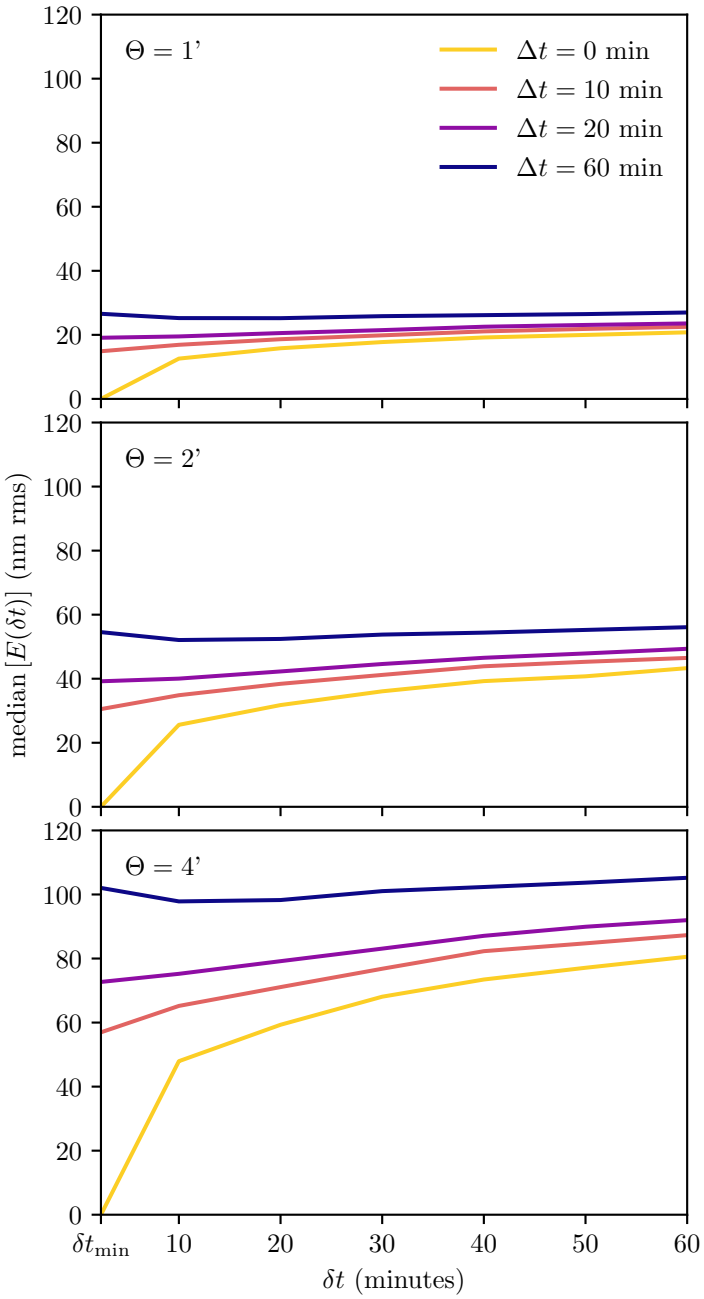

Figure 5.10: Median increase of tomographic error E with averaging time δt. From upper to lower panel: 1, 2 and 4 arcminute LGS asterisms. Several different values of the reconstructor optimisation period Δt are shown with different colours, from 0 to 1 hour.

update period Δt: when we are more frequently updating the reconstructor ($\Delta t <$ 20 minutes), increasing the averaging time is detrimental. We are dominated in this regime by the increase in tomographic error resulting from the fact that an optimisation profile consisting of the mean over δt is no longer matched to the current profile. If we increase Δt and update the reconstructor less frequently, overall the performance deteriorates as would be expected from Fig. 5.8. However the behaviour with δt changes and there is some optimum averaging time $\delta t > \delta t_{\text{min}}$ that provides slightly better overall performance. In this regime, for short averaging times we are dominated by increased error at large time since optimisation $t - t_{\text{opt}}$. By increasing the averaging time we reduce this increase in error over time, resulting in very slightly better error overall. This averaging time is between 10 and 20 minutes for all LGS asterisms. Overall this effect is small and only changes the tomographic error by a few nm rms.

5.5 Optimisation strategies

We have shown in section 5.4.1 that unpredictable variability in the profile over time means it is difficult to select a single reoptimisation period for a particular asterism. Longer optimisation periods are a gamble with the atmosphere. If we are lucky and optimise at the correct time the profile will change very little and we will achieve near optimal performance. The opposite is also true, if we optimise at the wrong time then the tomographic error can rapidly degrade as seen in Fig. 5.7. Minimisation of these error spikes is important for a system to maintain consistent performance over an observation.

The risk of a sudden increase in error can of course be minimised by selecting the shortest possible reoptimisation period. We can see from Fig. 5.9 that this should be less than around $\Delta t = 10$ minutes (depending on the LGS asterism and tolerated error increase) to maintain near optimal performance in approximately 95% of conditions. However, there is no reason why the optimisation period must

be fixed. Indeed the unpredictable changes in the profile mean that there may be long periods of almost constant profile followed by rapid changes.

Therefore we propose an alternative optimisation strategy, where the reconstructor is optimised not on some constant timescale Δt but instead in the case where the increase in error E reaches some threshold E_{crit}. This can be accomplished in reality by employing the same analytical Fourier simulation as employed here. For a new turbulence profile measured by the system or an external profiler, the simulation can provide, in several seconds, an idea of how this new profile has affected the tomographic error of the system. If the error has degraded beyond E_{crit}, then we optimise the reconstructor using this new profile.

To investigate the differences between these strategies we select two contrasting nights of $C_n^2(h)$ profiles from the dataset. The first, shown in Fig. 5.11, displays a large amount of variability in the profile throughout the night. In the second night in Fig. 5.12, the profile is less variable.

For each night, we compare the following optimisation strategies:

- **Optimal strategy**: Reconstructor updated with every new profile. Best possible tomographic error.
- **Worst strategy**: Not updating the reconstructor, using only the ESO 35 layer median profile. Corresponds to worst case performance as per Fig. 5.1.
- $\boldsymbol{\Delta t}$ **= 1 hour (lucky)**: Optimising when $t - t_{\text{opt}} > 1$ hour, at lucky times where the profile does not change much over the optimisation period.
- $\boldsymbol{\Delta t}$ **= 1 hour (unlucky)**: Optimising when $t - t_{\text{opt}} > 1$ hour, at unlucky times where the profile changes over the optimisation period.
- $\boldsymbol{\Delta t}$ **= 10 minutes**: Optimising when $t - t_{\text{opt}} > 10$ minutes.
- $\boldsymbol{E_{\text{crit}}}$ **= 40 nm**: Optimising when the increase in tomographic error becomes greater than 40 nm rms.

Of course in reality it is not possible to choose lucky or unlucky times to optimise the reconstructor. However, by simulating all possible optimisation times and selecting the best and worst cases, we show the potential variability than can arise as a result of changing optimisation times.

For the sake of brevity, we perform this analysis only for the 1 arcminute LGS asterism case. Additionally, we assume that sufficient layers are reconstructed that model error is small in comparison to the temporal error. From Figs. 5.4 and 5.5 this corresponds to an assumption that $N \geq 10$ for a 1 arcminute asterism. Since we have shown in section 5.4.2 that the averaging time δt has little effect on the tomographic error, we neglect it here. We also assume that other factors such as changing zenith angle are negligable, i.e. we are pointing near zenith.

Starting with Fig. 5.11, we see that there are some spikes in error throughout the night. These occur when the profile undergoes a large change and the system is not reoptimised. The worst error spikes occur unsurprisingly for the $\Delta t = 1$ hour case, particularly if we optimise at unlucky times. The worst spike at 04:00 UT is a good example of a lucky vs. unlucky optimisation. In the lucky case we happen to optimise just after the profile changes, meaning that we obtain near optimal error around 70 nm rms as opposed to 150 nm if we are unlucky. Clearly if the profile is this variable there is value in optimising at lucky times. Both $\Delta t = 10$ minutes and $E_{\text{crit}} = 40$ nm maintain almost optimal error over the entire night. However, looking at the optimisation times it is clear especially for the first half of the night that $\Delta t = 10$ minutes results in some unnecessary reconstructor optimisations.

Our second chosen night in Fig. 5.12 shows smaller errors as would be expected from a calmer atmosphere. We do not see the same spikes in error as in Fig. 5.11 and for the most part all optimisation strategies perform fairly well. At times such as this when the atmosphere is less variable optimising on timescales of 1 hour is enough to give good performance. The gain from decreasing this timescale to 10 minutes is small. The optimisation times for the $E_{\text{crit}} = 40$ nm case in particular shows how little the profile is changing. For example, the same reconstructor is

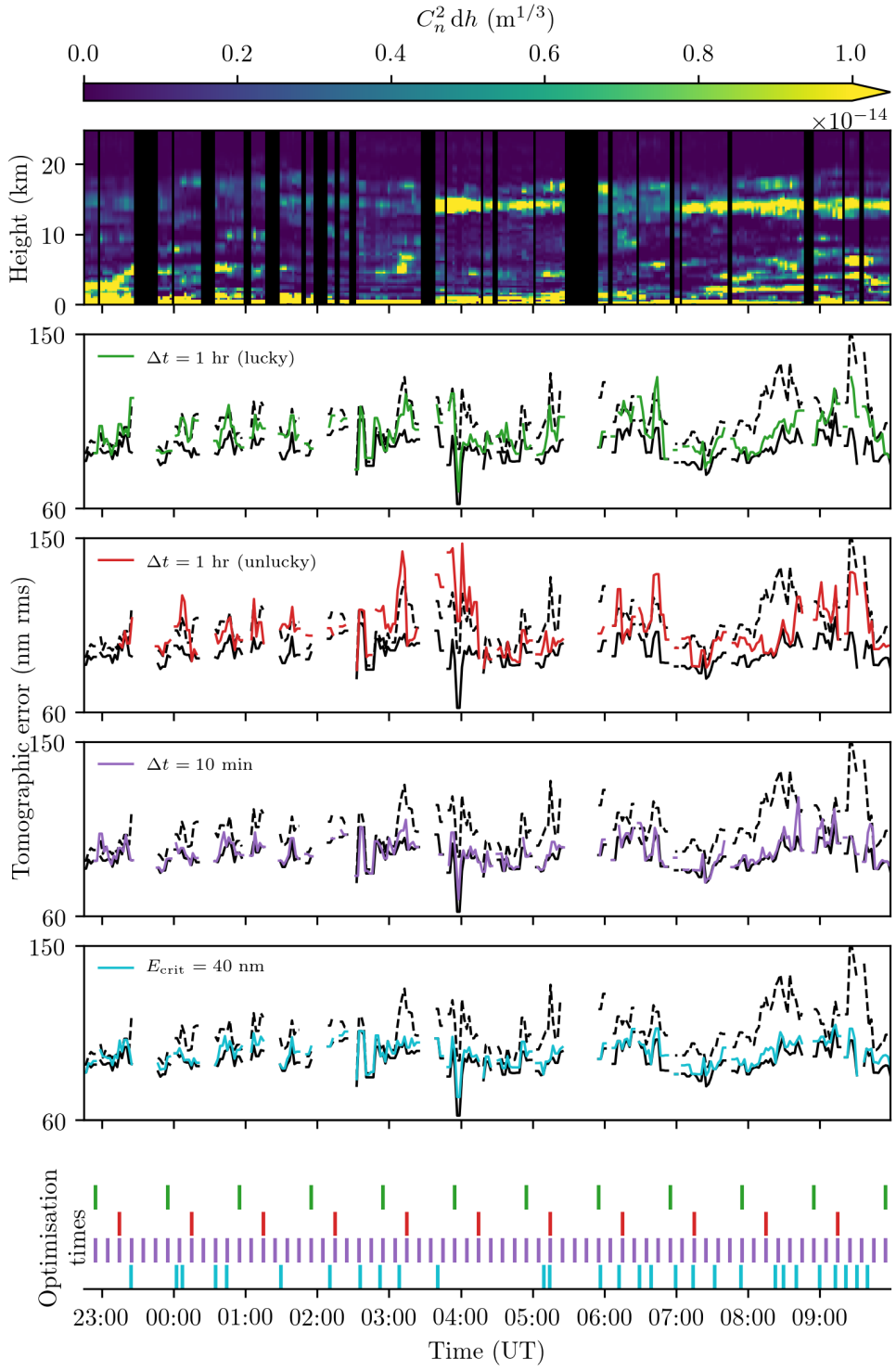

Figure 5.11: ELT tomographic error over the night of 6th August 2017, using a 1 arcminute diameter LGS asterism. *Upper*: C_n^2 profile evolution over the night. *Middle*: Corresponding tomographic error for different optimisation strategies. Solid and dashed black lines indicate optimal and worst strategies respectively, and are the same for all panels. *Lower*: Optimisation times for each strategy, colours same as the middle panels.

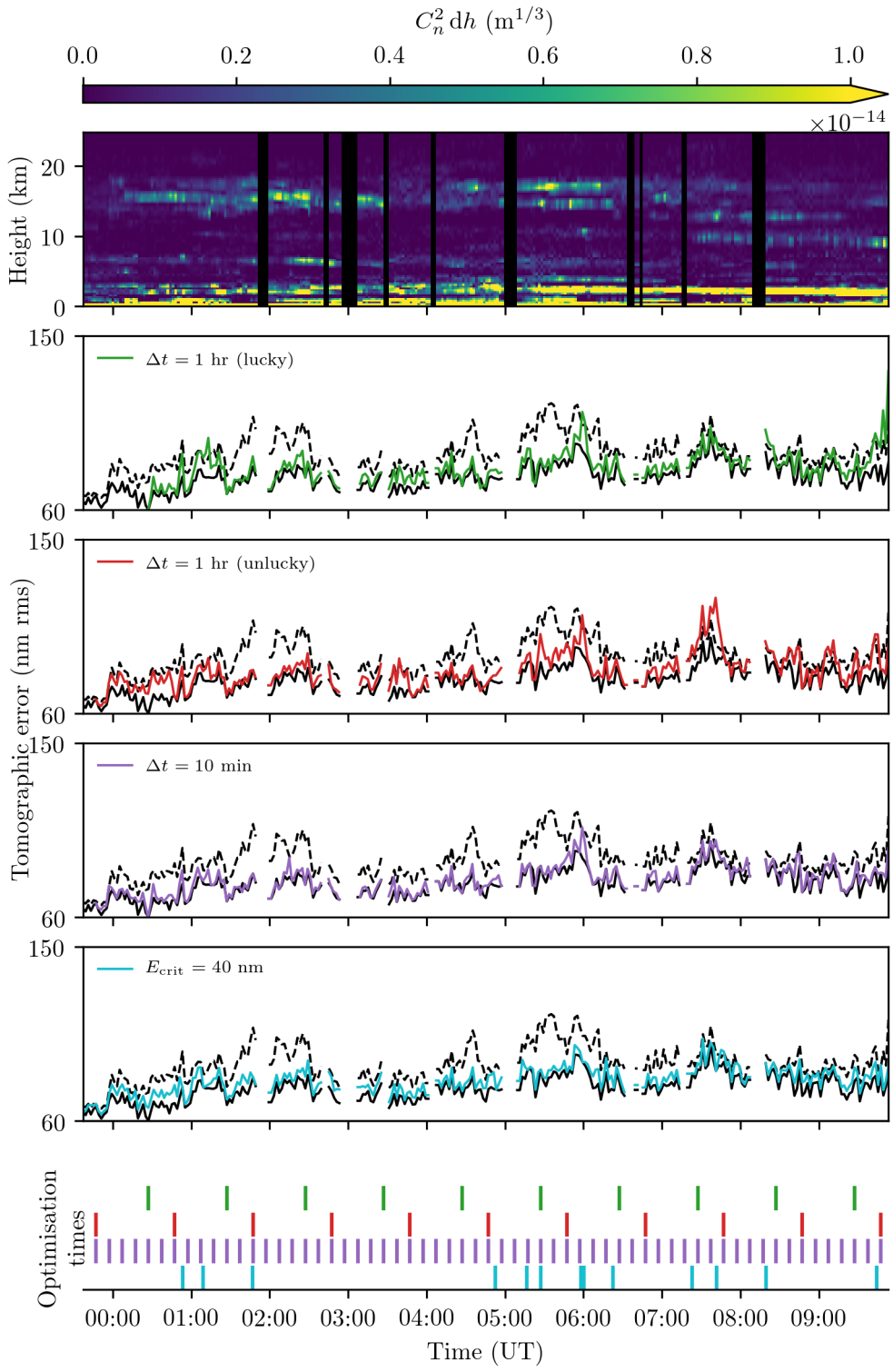

Figure 5.12: ELT tomographic error over the night of 29th April 2016, using a 1 arminute diameter LGS asterism. Layout as Fig. 5.11.

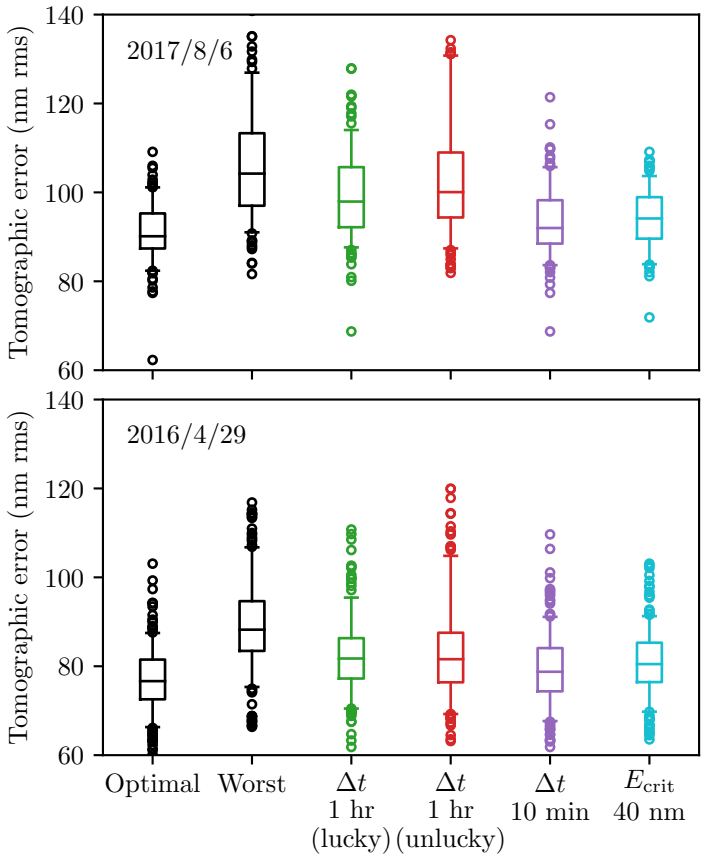

Figure 5.13: Distribution of increase in tomographic error over the nights of 6th August 2017 (upper panel) and 29th April 2016 (lower panel), for different optimisation strategies. Upper and lower boxplot whiskers represent the 5th and 95th percentiles. Circular markers represent outlier data points above the 95th and below the 5th percentiles.

used for 3 hours between 01:50 and 04:50 UT without any significant increase in error.

Finally, in Fig. 5.13 we compare integrated tomographic error across the two nights. Overall error is predictably worse for the first night where the atmosphere is more variable. We see that for both nights the closest to optimal tomographic error is obtained by either optimising fast ($\Delta t = 10$ minutes) or by limiting the increase in tomographic error to $E_{\text{crit}} = 40$ nm. However for the more variable night even with 10 minutes between optimisations there are still a small number of outliers pushing up to over 120 nm rms tomographic error, suggesting that despite this fast update rate we can still be unlucky in a small number of cases. For the longer $\Delta t = 1$ hour

periods, we see the pronounced difference in the upper end of the error distribution for the more variable night indicating the gain from optimising at the right (lucky) times.

Thus it seems that optimising to some maximum error threshold, allowing for the reconstructor optimisation period to dynamically change over the course of a night, gives the greatest flexibility. When the atmosphere is calm, the reconstructor does not need to be optimised for multiple hours, however when an unpredictable change in the profile occurs we can quickly reoptimise and avoid some of the larger increases in error that we see in the spikes of Fig. 5.11. The exact value of E_{crit} for a particular system will need to be tuned depending on the tolerances in the error budget and the capabilities of the SRTC.

5.6 Conclusions

We have shown, using fast AO simulation, the effects of sub-optimal tomographic reconstruction on AO performance for an ELT-scale system with a large database of real turbulence profiles from the Stereo-SCIDAR at ESO Paranal.

The number of reconstructed layers, N, can have a significant impact on the tomographic error when below a certain threshold. The exact number of layers required will depend on the tolerated level of error for a particular instrument and the LGS asterism diameter. The best tomographic error for a given number of layers is obtained with the optimal grouping compression method. Using this as a baseline, 2 - 6 addditional layers are required to achieve the same error with equivalent layers compression. If the layers are fixed in altitude, a further 2 - 10 layers are required. Variability of turbulence profiles also plays a role here, as some profiles lend themselves to modelling with few layers whereas others do not. A system wishing to operate to a given error tolerance in the best 95% of turbulence profiles (with respect to the tomographic error) will need to reconstruct between 6 - 12 additional layers compared to a system operating only in the best 50% of profiles.

The increase in tomographic error over time since reconstructor optimisation was investigated, with the temporal sampling of the Stereo-SCIDAR data allowing us to probe scales as small as several minutes. We find that, although the absolute increase in error is greater for larger asterisms, the shape of this increase with time is similar for all asterisms. After around 20 minutes, the increase in error plateaus and we see smaller increases in tomographic error with time. We therefore conclude that the scale of temporal atmospheric variations as seen by a tomographic AO system is of the order of 20 minutes, and as such one should choose a reconstructor update period of at least $\Delta t < 20$ minutes. The increase in tomographic error after 1 hour is on average between 30 and 130 nm rms depending on LGS asterism. However, the unpredictable variability of the profile means that large spikes in performance can occur on minute timescales, making it difficult to select a single optimal update rate.

We also investigated the effect of averaging time δt. The error arising from increased averaging of the profile is linked to the reconstructor update rate Δt. For small Δt, increasing δt only makes tomographic error worse: the averaged profile looks less like the real profile. However, if we allow the profile to evolve for longer before reoptimising by increasing Δt, averaging is less important. There is in fact some optimum value of $\delta t > \delta t_{\min}$ that slightly improves the tomographic error. This means that a small amount of averaging, usually of the order of $\delta t = 10$ minutes, can give the reconstructor slightly more resilience to a changing profile, but only if we are reoptimising on long timescales $\Delta t > 20$ minutes. The gain by averaging is very small (of the order of a few percent) compared to the other sources of error investigated here. From a purely atmospheric perspective, i.e. considering only the non-stationary nature of the profile, averaging does not confer any advantage or disadvantage.

Finally, we selected two contrasting nights to compare temporal optimisation strategies. When optimising on long timescales ($\Delta t = 1$ hour) it was found, particularly on the night where the profile is more variable, that it is important to be lucky. That

is, to optimise the reconstructor at the right times to avoid large tomographic error spikes. Since this is impossible in reality a very short optimisation period of the order of $\Delta t = 10$ minutes must be used. On the night where the profile is less variable, optimising only once per hour gives good results. By optimising only when the increase in tomographic error reaches some threshold E_{crit}, we are able to obtain good tomographic error at all times by allowing the optimisation period to change dynamically with the atmosphere. With careful selection of E_{crit} for a system, the requirements for the SRTC can be relaxed whilst maintaining near optimal tomographic reconstruction.

6

pt5m-SCIDAR

6.1 Introduction

Large statistically significant datasets of optical turbulence profiles are fundamental to the analysis presented in the previous chapters. It is also clear according section 5.3 that for ELT AO, the number of layers required to model the atmosphere effectively is of the order of 10, depending on the specifics of the system in question.

Instruments such as SCIDAR are more than capable of measuring profiles with over ten times the required vertical resolution with very high sensitivity. However, the resolution of these profilers depends on large apertures and as such are operated on preexisting telescopes with apertures around $D \approx 2$ m. Since these telescopes primarily used for science observations they may not be dedicated to full-time profiling operation. This severely limits the statistical data-gathering effectiveness of the instrument as it may only be operated a small fraction of the time. As a result, long term large databases of high resolution profiles (Osborn et al., 2018; García-Lorenzo and Fuensalida, 2011) are rare and require a concerted effort from the observatory to compile.

In contrast, profilers such as the MASS operate using their own dedicated small

robotic telescope that requires minimal operator interaction once commissioned. They may be run continously every night, producing very large datasets over long time scales (see e.g. Kornilov, 2012). Unfortunately, the altitude resolution of the MASS is not high enough for the purposes of ELT AO tomography, with the ability to fit only 6 fixed layers to the turbulent volume. Similarly, robotic SLODAR systems on small telescopes (see e.g. Butterley et al., 2020) are limited to fewer than 10 layers due to the effect of scintillation on small subapertures.

One solution to this problem would be a SCIDAR-type instrument operating on a dedicated 1 - 2 m class telescope. However as the cost of a telescope and required infrastructure (mounts, domes etc.) rises as $D^{2.45}$ (van Belle et al., 2004), this solution is prohibitively expensive for most observatories. To provide some context, as of July 2020 the typical cost of a small ($D \approx 0.3$ m) commerically available telescope for a MASS or DIMM is around \$2k*, plus costs for a small dome and mount. At the opposite end of the commercial telescope spectrum, a 1 m diameter telescope (including mount but without a dome) may currently be purchased for \$650k†. For bespoke telescopes with diameters larger than this, costs rapidly exceed multiple millions of dollars.

In this chapter, SCIDAR analysis using a relatively small ($D = 0.5$ m) aperture telescope is investigated as a potential remote site characterisation and monitoring tool for ELT-scale tomographic AO. More specifically, we present simulations and on-sky data from a SCIDAR instrument operated on the point-5 m (pt5m) telescope, operated on the roof of the William Herschel telescope (WHT) at the Observatorio Roque de los Muchachos (ORM), La Palma.

The remarkable information density contained in the spatial scintillation pattern, with scales from a few cm to around 10 cm depending on altitude (see Eq. 2.21), means that even with this small aperture the atmosphere can be measured with 11 to 15 layers depending on the observed target. A SCIDAR instrument operating

*https://www.firstlightoptics.com/optical-tube-assemblies/celestron-c11-xlt-optical-tube-assembly-cge-losmandy.html

†https://planewave.com/products-page/cdk700/pw1000-cdk-telescope-system/

robotically on a dedicated telescope such as the pt5m would be able to produce the large databases that are required for the analysis in the previous chapters at a small fraction of the cost of a manually operated instrument on a larger telescope.

We present an overview of SCIDAR methods in section 6.2, including different SCIDAR configurations and theoretical sensitivity. We then present the pt5m-SCIDAR instrument in section 6.3, including simulations addressing some of the issues of implementing the SCIDAR technique with such a small aperture, namely diffraction and a loss in sensitivity. We then present on-sky data measured by the pt5m-SCIDAR in La Palma, with concurrent comparisons to other turbulence monitoring instruments in section 6.3.4.

6.2 Theory

The quantity measured by the SCIDAR method is the spatio-temporal covariance of the intensity pattern in the telescope pupil, which can be related to the strength and altitude of the turbulence by Eq. 2.20. By imaging a double star with known separation θ, the peaks in the covariance map are spatially separated and we can reconstruct a turbulence profile $C_n^2(h)$. A diagram depicting the principle of SCIDAR can be seen in Fig. 6.1.

The spatial autocovariance of the intensity pattern of the double star at the ground for a many layered atmosphere is given by

$$B_I(r,\theta) = \int_0^\infty A_1 B_I(r) + A_2[B_I(r-\theta h) + B_I(r+\theta h)]\mathrm{d}h, \tag{6.1}$$

where A_1 and A_2 denote the amplitudes of the central ($B_I(r)$) and spatially separated ($B_I(r \pm \theta h)$) covariance peaks. The irradiance covariance $B_I(r)$ is given by Eq. 2.20. If the scintillation patterns from both stars are completely overlapping, A_1 and A_2 may be defined as

$$A_1 = \tfrac{1+\gamma^2}{(1+\gamma)^2}, \quad A_2 = \tfrac{\gamma}{(1+\gamma)^2} \tag{6.2}$$

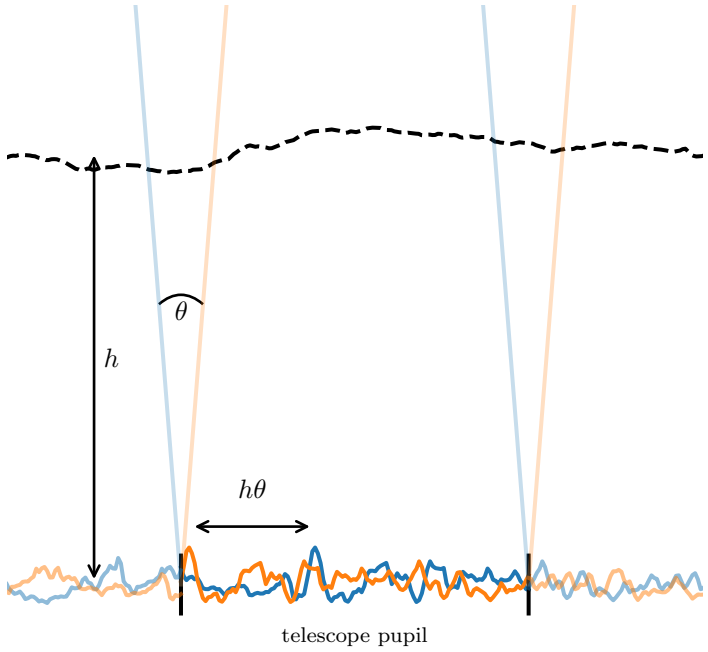

Figure 6.1: Diagram of the SCIDAR principle. Turbulent layer at altitude h (black dashed line), produces a fluctuating intensity pattern (scintillation) at the ground. By observing a double star with separation angle θ we observe two scintillation patterns (blue and orange solid lines) that are spatially separated by a distance $h\theta$. By computing the spatial covariance of the intensity pattern we can measure $h\theta$ as well as the amplitude of the covariance peak which gives us the altitude and strength of the turbulent layer.

where $\gamma = 10^{-0.4\Delta m}$ with Δm the magnitude difference between the two stars (Shepherd et al., 2014). For the simplest case where $\Delta m = 0$, $A_1 = 0.5$ and $A_2 = 0.25$, therefore the central peak is twice as high as the spatially separated peaks. The width of the peaks is proportional to the Fresnel zone radius in Eq. 2.21, and can be related to the altitude resolution of the instrument

$$\delta h = \epsilon \frac{r_F(h)}{\theta} = \epsilon \frac{\sqrt{\lambda h}}{\theta}, \tag{6.3}$$

where the parameter ϵ can vary depending on the fitting method (Prieur et al., 2001; Avila et al., 2008; Fried, 1995). Here we will take $\epsilon = 0.5$. The maximum altitude attainable is related to the maximum spatial separation at which we may measure covariance peaks

$$h_{\max} = \frac{D}{\theta}, \tag{6.4}$$

for telescope with outer diameter D. Rearranging and substituting for θ in Eq. 6.3 we obtain

$$\delta h = \epsilon \frac{h_{\max}\sqrt{\lambda h}}{D}. \tag{6.5}$$

Assuming we can find a target with separation θ for a diameter D such that $h_{\max}$ is a reasonable value (usually in the range 20 km to 30 km), we can see that δh is inversely proportional to D. Therefore ultimately the resolution and hence the number of layers measurable by the SCIDAR is limited linearly by the aperture diameter.

The scintillation covariance is measured in practice by recording many short exposure images of the scintillation pattern in the telescope pupil $I(r)$. From each frame we may numerically compute the covariance which we will denote $\Gamma_I(r)$. Given a set of frames our best estimate of the spatial covariance, $\Lambda(r)$, is then

$$\Lambda(r) = \frac{\Gamma_I(r) - \Gamma_{\langle I \rangle}(r)}{\Gamma_{\langle I \rangle}(r)} \tag{6.6}$$

where $\langle I \rangle$ denotes the temporal average of all the frames in the set. The normalisation term $\Gamma_{\langle I \rangle}(r)$ is required since we are observing the scintillation pattern through a finite aperture. This term approximates the autocovariance of the aperture iself $S(r)$ which must be cancelled out in order to observe the scintillation covariance.

Depending on the SCIDAR configuration, $\Lambda(r)$ may correspond directly with the theoretical scintillation autocovariance $\Lambda(r) = B_I(r, \theta)$ or the normalisation may be more complex, which must be taken into account when calculating instrument response functions (Avila and Cuevas, 2009).

6.2.1 SCIDAR configurations

We show in Fig. 6.2 the pupil images and resulting covariance maps from different configurations of SCIDAR instruments. In "classical" SCIDAR, the entrance pupil of the telescope is imaged directly (Azouit and Vernin, 1980). In this case, we observe two fully superimposed scintillation patterns and therefore in the autoco-

variance we see a triplet of peaks for each layer with separation $h\theta$ according to Eqs. 6.1 and 6.2.

We know from section 2.2.2 that scintillation requires some propagation distance to produce a signal, hence the classical SCIDAR is not sensitive to ground layer turbulence at $h = 0$. In order to be sensitive to this layer we may optically conjugate our imaging plane to some height $h_{\text{conj}} < 0$ below the ground. This is the generalised-SCIDAR principle (Avila et al., 1997; Fuchs et al., 1998), and allows the recovery of the full atmosphere turbulence profile. Normal negative conjugation altitudes are between -1 and -3 km, which is sufficient for the ground layer scintillation signal to be measured above the noise whilst minimising diffraction effects (see Fig. 6.5) and potential saturation of the scintillation, at which point the weak fluctuation theory breaks down and the instrument becomes insensitive (Roddier, 1981).

Instead of a single pupil image, the negative conjugation altitude results in partially overlapping pupil images from each star separated by $|h_{\text{conj}}\theta|$. The spatial separation of autocovariance peaks is now $|h - h_{\text{conj}}|\theta$. Since the pupils are now partially overlapping, the amplitudes of the central and lateral covariance peaks A_1 and A_2 are no longer given by Eq. 6.2, as the contrast of the scintillation pattern and therefore the height of the covariance peak depends on the position in the pupil.

Depending on h_{conj} and θ, the two pupil images may be completely separated. This is the case for SCIDAR instruments operating with very wide double stars to profile only low layer turbulence (Avila et al., 2008). The separation of pupil images may also be accomplished by use of a mirrored prism in the focal plane (Shepherd et al., 2014). Either way, in separating the pupil images we may extract each pupil and calculate the crosscovariance between them. Since the pupils are imaged on different parts of the detector, or onto two separate detectors in the case of Stereo-SCIDAR, the contrast is increased resulting in a gain in sensitivity of up to a factor of 2. Additionally, since we calculate a crosscovariance between pupil

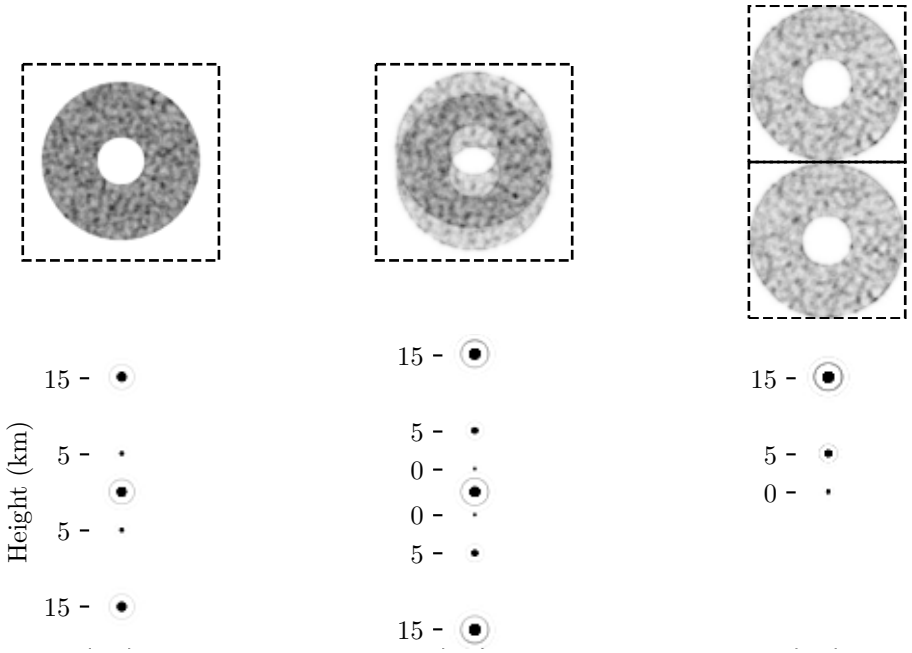

Figure 6.2: Pupil images obtained for different configurations of SCIDAR (upper) with corresponding scintillation auto- or cross-covariances $\Lambda(r)$ (lower). From left to right: classical SCIDAR, generalised SCIDAR and Stereo-SCIDAR. We use a three layer atmosphere with equal strength layers at $h = 0$ km, 5 km and 15 km. For generalised and Stereo-SCIDAR, the conjugation altitude is -3 km. The height of the layer corresponding to each peak in the auto- and crosscovariances is indicated. Note that the classical SCIDAR is insensitive to the ground layer and the peak at the centre of the autocovariance contains only information about the layers at 5 and 15 km. For the Stereo-SCIDAR there is only one set of peaks since we perform the crosscovariance between the two separated pupil images.

images rather than the autocovariance we remove the central peak and the offset of peaks corresponding to turbulent layers is now $h\theta$ as for classical SCIDAR.

6.2.2 Sensitivity

An important feature of SCIDAR, especially on large telescopes, is the sensitivity to the turbulence profile, allowing turbulent layers with very small C_n^2 values to be measured. This high sensitivity is due to the fact that the spatial scales of the scintillation pattern are small (up to 10 cm), therefore many independent scintillation speckles may be measured in each frame. This results in higher sensitivity than methods that measure the phase aberration directly such as SLODAR, since

the spatial scales involved ($\approx r_0$) are larger.

The theoretical sensitivity of the SCIDAR method is derived assuming that the measured scintillation is dominated by a single layer at height H_0. A scintillation signal in the covariance from a layer at altitude h must be detected against the background scintillation noise from the layer at H_0 as well as detector noise. Following the treatment of Prieur et al. (2001, 2004) and Shepherd et al. (2014), the noise in the covariance can be written as

$$\Delta B_I(r) = \frac{A_1 B(0) + (R/N_\gamma)^2 + 1/N_\gamma}{\sqrt{D^2 f(r)/\lambda H_0}}, \tag{6.7}$$

where the three terms in the numerator represent total scintillation, detector read-out noise and shot noise respectively. R is the average read-out noise per scintillation speckle and N_γ is the average number of photons per scintillation speckle per frame. $f(r)$ denotes the area of overlap of the telescope pupil with a spatial shift of r. This accounts for the different number of scintillation speckles that are observed at different altitudes, since we must observe a speckle in both pupil images in order to measure it in the covariance.

Eq. 6.7 is then converted into the turbulence profile sensitivity $\Delta J(h)$, where $J = C_n^2(h)\,\mathrm{d}h$, by dividing by the scintillation index of a layer at altitude h with $C_n^2 = 1$:

$$\Delta J(h) = \frac{5.23 \times 10^{-2} \lambda^{5/3} h^{-5/6} H_0^{1/2} (A_1 B(0) + (R/N_\gamma)^2 + 1/N_\gamma)}{A_2 D \sqrt{f(h\theta) N_{\text{frames}}}}. \tag{6.8}$$

Here, N_{frames} denotes the number of independent frames that are averaged to form a single auto- or crosscovariance and we have used $r = h\theta$ with θ the double star separation.

Due to the dependence on the dominant layer H_0, this model of the sensitivity of SCIDAR depends on the turbulence profile itself. Additionally, the sensitivity depends on the current target separation θ and brightness N_γ. Therefore single values of $\Delta J(h)$ for a given system do not exist. We can, however, use the Paranal 2018A dataset to estimate the distribution of $\Delta J(h)$ for many turbulence profiles.

In Fig. 6.3, we compare the contributions of the three noise sources from the numerator of Eq. 6.7 for different target magnitudes. Detector shot and read-out noise depend on the target brightness however the scintillation noise does not, meaning that the scintillation noise represents the unavoidable noise floor for the brightest targets.

An important observation is that the scintillation and shot noise terms do not depend on the detector used to image the pupil, since they are dependent only on the profile and the number of photons per scintillation speckle N_γ. The read-out noise term however does depend on the detector through the parameter R. The calculation of R, the average read-out noise per scintillation speckle, must take into account firstly the read-out noise per pixel R_{pxl} of the camera and the the number of pixels per speckle

$$R = R_{\text{pxl}} \sqrt{\frac{\pi r_F^2}{\delta_{\text{pxl}}^2}}, \tag{6.9}$$

where r_F is the Fresnel radius of the dominant layer at $h = H_0$ (Eq. 2.21) and δ_{pxl} is the size of the pixel projected onto the telescope pupil. It is therefore important to minimise the read-out noise and maximise the pixel size of the detector, whilst still adequately sampling scintillation speckles. In Fig. 6.3 we show two cases for the read-out noise as a function of target V-band magnitude V, with $R_{\text{pxl}} = 1e^-$ rms but pixel sizes of 1.8 cm and 0.3 cm.

Shot noise begins to become a significant contribution at around $V = 6$, however the shallow slope means that it does not begin to dominate until around $V = 8$. For larger pixels ($\delta_{\text{pxl}} = 1.8$ cm), the read-out contribution is not significant until around $V = 8$. However, for smaller pixels ($\delta_{\text{pxl}} = 0.3$ cm), the read noise starts to become significant at around $V = 5$.

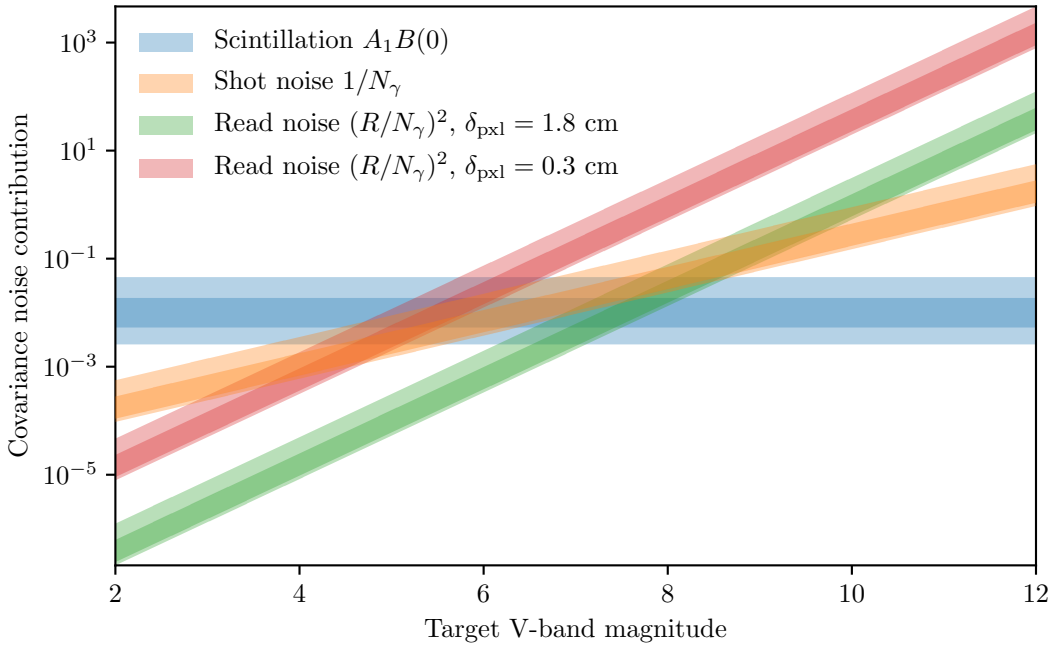

Figure 6.3: Contributions to noise in the covariance for the SCIDAR method. The double star targets are assumed to have the same magnitude ($\Delta m = 0$). Darker and lighter shaded areas represent the 25th - 75th and 5th - 95th percentile of the distribution of values across the Paranal Stereo-SCIDAR 2018A dataset. A detector with quantum efficiency of 100%, read-out noise of 1 e^- rms and exposure time of 1 ms are also assumed.

6.3 pt5m-SCIDAR

The pt5m telscope is a robotic telescope operated on the roof of the WHT at the ORM, La Palma, Canary Islands. It has a primary mirror diameter of 0.5 m and is used mainly for remote observations (Hardy et al., 2015). By means of a single lens and detector placed at the telescope's eyepiece, we may observe negatively conjugated pupil images and hence employ the SCIDAR method to measure the optical turbulence profile for this site.

The configuration of the pt5m-SCIDAR is described in Tab. 6.1. In order to obtain full atmosphere turbulence profiles with a 0.5 m aperture, target stellar separations must be small, of the order of 5 arcseconds. With such small separations it is very difficult to separate the double stars in the focal plane using a wedge as for Stereo-SCIDAR (Shepherd et al., 2014). We must therefore operate in generalised mode

Pupil diameter (m)	0.5
Central obscuration diameter (m)	0.15
SCIDAR configuration	Generalised
Camera	ZWO ASI174MM (CMOS)
Conjugate altitude (km)	- 3
Projected pixel size (mm)	3.0
Camera frame rate (Hz)	∼300
Frames per data packet	500
Data packets per profile	100
λ (assumed) (nm)	500

Table 6.1: Instrument parameters for the pt5m-SCIDAR.

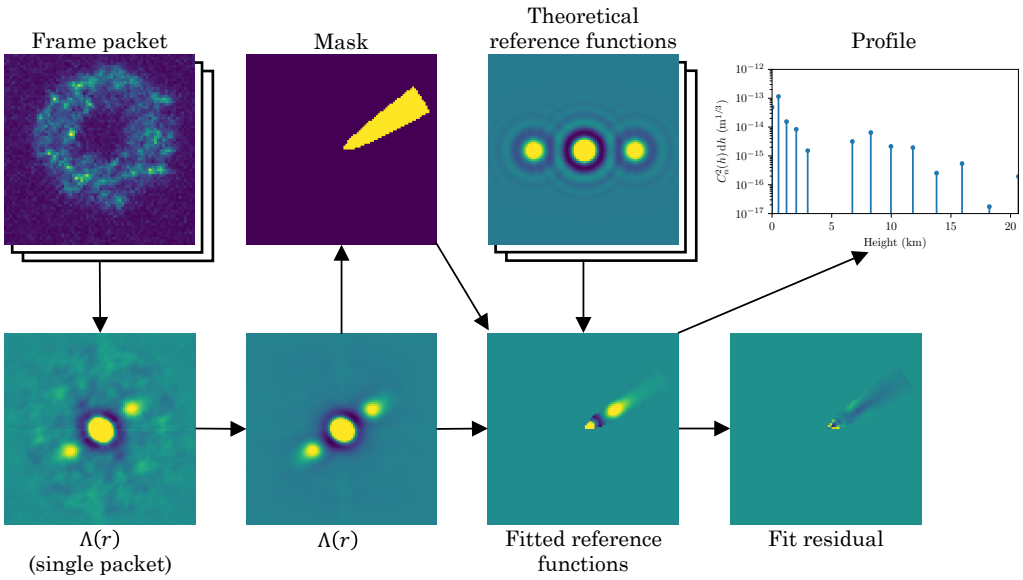

Figure 6.4: Diagram illustrating the data processing pipeline of the pt5m-SCIDAR. The example data used is taken from the night of 17th May 2019.

and accept approximately a factor of 2 loss in sensitivity.

The pt5m-SCIDAR was operated sporadically during observing runs at ORM, La Palma from 2017 — 2019. During these runs, raw pupil images were taken and stored with the processing of this data occuring at a later date. In Fig. 6.4 we illustrate the data processing pipeline. The stages are as follows:

1. $\Lambda(r)$ for each data packet is computed via Eq. 6.6. Before this computation the bias is computed and subtracted from the data packet. If there is a large amount of wind shake, we also perform a shift-alignment procedure on

each frame to try to ensure that the pupil images in the packet are correctly aligned. This procedure does not always succeed, in which case the data is discarded.

2. Temporal averaging over many packets to obtain our final $\Lambda(r)$. This averaging takes into account a maximum time window (here we use 5 minutes) between packets such that we do not average over timescales at which the profile may be changing.

3. The pt5m-SCIDAR does not have a rotator, so the lateral peaks in $\Lambda(r)$ are offset by some angle depending on the position angle of the target double star. We fit to this angle by applying a mask with a square-root profile that matches the width of the scintillation peaks with altitude. By maximising the pixel sum inside this mask we find this rotation whilst at the same time isolating the portion of the autocovariance containing information about the profile and rejecting noise.

4. A set of theoretical reference functions, which are precomputed for the current target and conjugate altitude, are rotated to match the rotation of $\Lambda(r)$ and masked.

5. An non-negative least squares (NNLS) algorithm is used to fit the reference functions to $\Lambda(r)$, resulting in the best fit turbulence profile. The residual of the best fit is also computed.

In the following simulations the same pipeline is used, with the source of data being simulated pupil images.

6.3.1 Effect of diffraction

The conjugation of the analysis plane below the ground in the case of generalised SCIDAR will result in diffraction since the pupil has sharp, defined edges. We show the effect of this diffraction on the pupil of the pt5m telescope in Fig. 6.5.

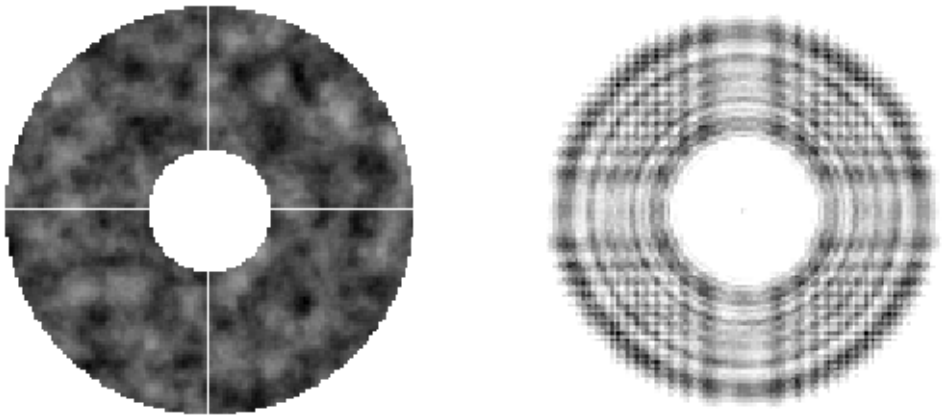

Figure 6.5: Simulated short exposure pupil images showing the effect of diffraction on the pupil of the pt5m telescope. In both cases, the scintillation pattern from a turbulent layer at an altitude of $h = 10$ km is observed. *Left*: Imaging plane conjugate to pupil (ground). *Right*: Imaging plane conjugate to -3 km, showing multiple diffraction rings from both the circular pupil and horizontal/vertical spiders.

The spatial scale of the diffraction effect is, as with scintillation, related to the Fresnel zone size (Eq. 2.21), with a propagation distance of h_{conj}. An imaging plane conjugate to -3 km produces diffraction rings on the scale of approximately 4 cm at $\lambda = 500$ nm. This is small enough to be neglected for traditional large aperture SCIDAR, however it has a strong visual effect for smaller apertures such as the pt5m as seen on the right of Fig. 6.5, where the scintillation pattern is almost completely obscured.

We assess the effect of this diffraction on the recovered scintillation autocovariance $\Lambda(r)$ in Monte Carlo simulation. By applying the pupil mask either at the ground ($h = 0$) or at the analysis plane ($h = h_{\text{conj}}$) we can choose whether to include diffraction effects. Using the pt5m aperture from Fig. 6.5 in a generalised-SCIDAR configuration, we obtain responses from the instrument as illustrated in Fig. 6.6. We can see that for all layer altitudes the responses without diffraction are in good agreement with the theory. When diffraction is included, the effect is altitude dependent. For the ground layer, the amplitude of the covariance peak is slightly larger than both the theory and without diffraction cases. For free atmosphere

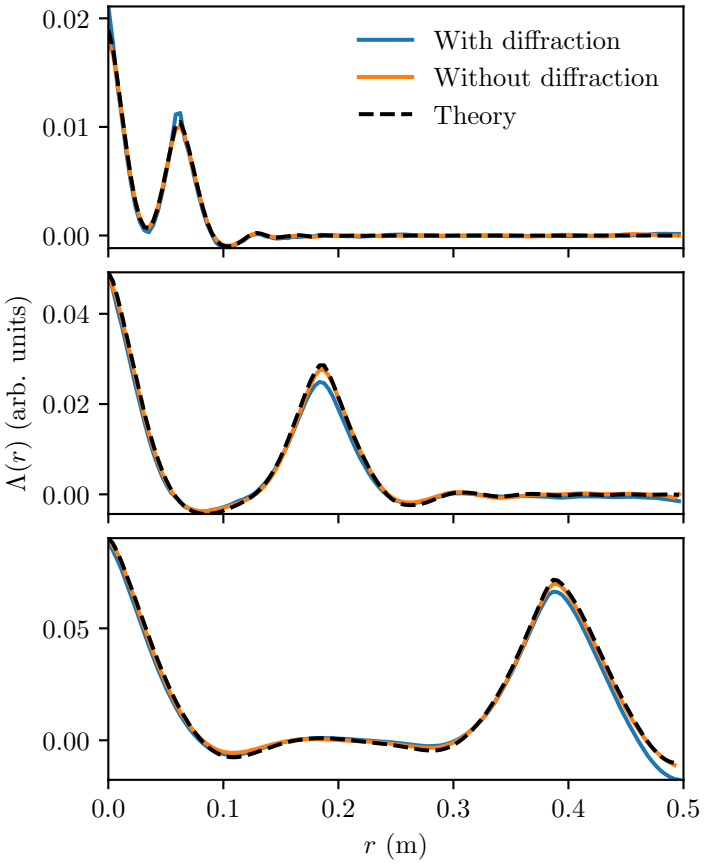

Figure 6.6: 1D cuts of the measured spatial covariance $\Lambda(r)$ as a function of separation r in the telescope pupil. Solid lines are calculated from Monte Carlo simulation of a generalised-SCIDAR configuration on the pt5m telescope observing a double star with separation $\theta = 4.125$ arcseconds and $\Delta m = 0$. From upper to lower panels: single turbulent layers at altitudes of 0, 6.3 and 16.3 km respectively. For each single layer 1000 random phase screens with $r_0 = 32$ cm are used.

layers however, the covariance peak is smaller than expected.

The effect of diffraction on the amplitude of covariance peaks is small, and by fitting the theoretical reference functions to each layer we can estimate the error in $C_n^2(h)\,\mathrm{d}h$ that will result from diffraction. From Fig. 6.7 we can see that for the pt5m telescope this error reaches around 10% with diffraction effects included. The error has an altitude dependency as would be expected from Fig. 6.6, with the ground layer having the smallest error. There is also a smaller error in the case without diffraction which exhibits less altitude dependence, of the order of 5%. We attribute this to small discrepancies between theory and simulation that result in

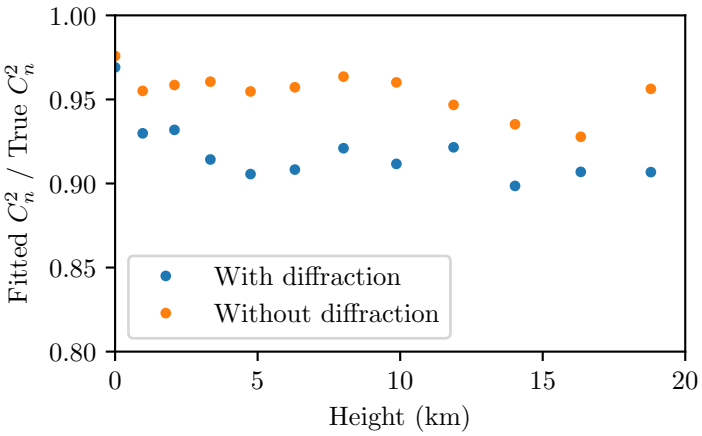

Figure 6.7: Relative error in the C_n^2 fitted to theoretical SCIDAR response functions for the pt5m telescope in a generalised SCIDAR configuration. For each altitude 1000 random phase screens with $r_0 = 32$ cm are used.

errors in the fitting procedure.

This altitude varying error between 5% and 10% in C_n^2 could be calibrated out by applying the inverse correction to all measured profiles. However, as we will see in section 6.3 these errors only translate into small biases in r_0 and θ_0. Therefore we conclude that the diffraction effect, whilst being large upon visual inspection of the pupil images, is small enough to ignore for the pt5m aperture.

6.3.2 Sensitivity vs. larger apertures

Another challenge of the smaller aperture is a loss in sensitivity. The area over which we are averaging scintillation speckles is significantly smaller for the pt5m aperture relative to the ~ 2 m apertures used for conventional SCIDAR. The statistical noise in the covariance will therefore be larger. However, the most important values are not the absolute noise but the signal-to-noise ratio (SNR) $J/\Delta J$, since this determines the ability of the system to detect a layer above the noise floor. We assume that if a layer falls below this noise floor, the strength is recorded as $J(h) = 0$.

We first calculate the SNR of the layers in the 2018A dataset as they were measured by the Stereo-SCIDAR at Paranal, which uses the $D = 1.8$ m AT. For each profile

with dominant layer H_0, we use the real target separation and magnitudes to compute $J/\Delta J$ with all noise terms. We also assume $\delta_{\rm pxl} = 1.8$ cm and $R_{\rm pxl} = 1e^-$ which is consistent with the Andor Luca detector used for these observations. This gives us a distribution of SNR for each altitude bin, which is shown in the upper panel of Fig. 6.8. We are interested in the minimum possible SNR required to measure a layer, so we take the 5th percentile of this distribution at each altitude as a conservative estimate, indicated by the dashed line. This minimium SNR assumes that the system has measured layers which fall below the detection threshold at all altitudes, which may not be true for the strong ground layer. Therefore we ignore the ground layer in our subsequent analysis.

We can now compute similar SNR distributions for the pt5m-SCIDAR, and compare to the cutoff values. Given that the other parameters of the system remain the same (e.g. $N_{\rm frames}$, wavelength, exposure time, conjugate altitude), if the SNR for the pt5m-SCIDAR falls below the cutoff for a particular layer, we can assume that this layer would fall below the noise threshold and would therefore not be measured. These SNR calculations include the fact that the pt5m-SCIDAR operates in generalised mode and therefore loses a factor of 2 in sensitivity compared to the Stereo-SCIDAR.

We assess three cases for the pt5m-SCIDAR. Firstly we consider the case where the read-out noise $R = 0$, which describes the sensitivity limited only by the scintillation and shot noise which are not detector dependent. Secondly the case with $\delta_{\rm pxl} = 1.8$ cm, corresponding to the same detector as the Stereo-SCIDAR, and finally with $\delta_{\rm pxl} = 0.3$ cm, corresponding to the ZWO camera actually used for the pt5m-SCIDAR measurements at ORM. In both cases we assume $R_{\rm pxl} = 1e^-$ therefore the difference in the detectors arises only from the difference in pixel size and resulting increase in read-out noise per scintillation speckle (Eq. 6.9).

We show in the lower panel of Fig. 6.8 the fraction of total layers that maintain a SNR above the cutoff in these cases. For the zero read-out noise case we would expect to measure approximately 80% of layers measured by the Stereo-SCIDAR

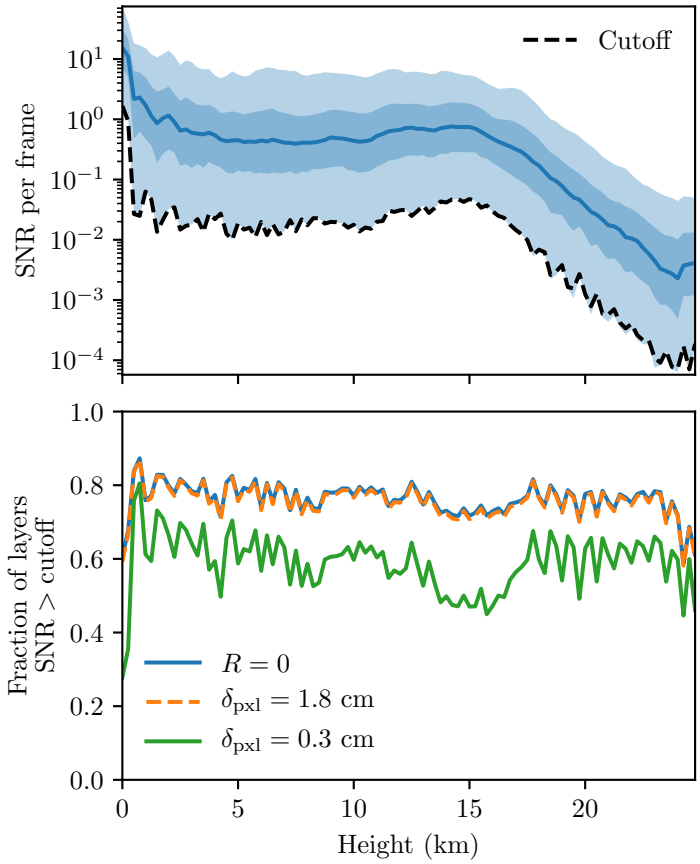

Figure 6.8: Effect of sensitivity loss of pt5m-SCIDAR compared to Stereo-SCIDAR, observing the 2018A dataset. *Upper*: Theoretical SNR per frame of layers measured by the Stereo-SCIDAR on the AT. Cutoff SNR for measuring a layer is denoted by the black dashed line at the 5th percentile of the distribution. *Lower*: Expected fraction of layers measured by the pt5m-SCIDAR measuring the same profiles, assuming the SNR must be above the cutoff.

at all altitudes. This is approximately the same for the larger pixel case, implying that read-out noise does not make any significant contribution to the overall noise. For smaller pixels and therefore larger read-out noise, we expect to observe around 60%. The layers lost will be the weakest in strength.

For the purposes of site testing and tomographic AO simulation we are concerned primarily with the strongest layers. Therefore, the loss to noise of the weakest layers for most of the atmosphere is not considered to be a major problem with this small telescope SCIDAR. To illustrate this we perform a Fourier AO simulation with the same parameters as described in Tab. 4.1. In Fig. 6.9 we show the distribution of

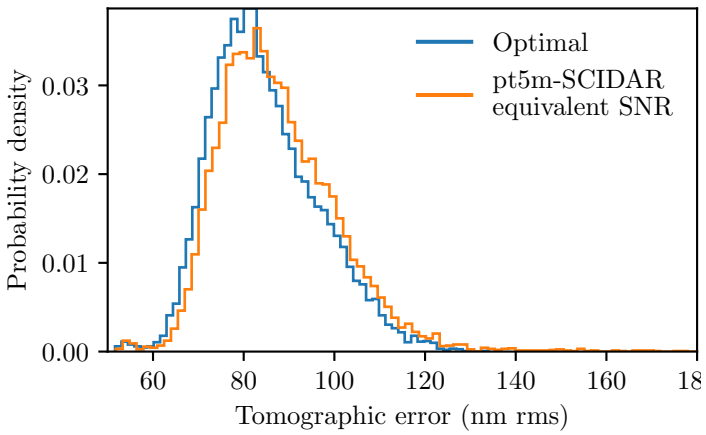

Figure 6.9: Tomographic error distributions obtained from Fourier simulation, in the optimal case where the profile is known perfectly (blue) and when the profile is measured with a SNR equivalent to the pt5m-SCIDAR with $\delta_{\text{pxl}} = 0.3$ cm (orange). The LGS asterism diameter used here is 1 arcminute.

tomographic error that results if the optimisation profile is missing approximately 40% of the weakest layers, corresponding to our worst case in Fig. 6.8.

We can see that the difference between this distribution and the optimal is small, the median increase in tomographic error (Eq. 5.1) being only 10 nm rms or around 1% in terms of the error variance. We therefore posit that the loss in sensitivity moving from large aperture SCIDAR to pt5m-SCIDAR will make only a small difference to the performance of a tomographic AO system and hence the profiles measured by the pt5m-SCIDAR would be equally valid for site testing and monitoring from an ELT tomographic AO perspective.

6.3.3 Simulation with 2018A clusters

Here we test the ability of the pt5m-SCIDAR to recover full turbulence profiles in E2E Monte Carlo simulation. By using the single profile clusters defined in chapter 3, we test the ability of the system to measure diverse profiles with both strong and weak layers at different altitudes. Due to computational limitations we are not able to use the full 100 layer profiles in our simulation, therefore we use 20 layer versions which are compressed using the equivalent layers method (see section 5.3).

We calculate two values to quantify the difference between our simulation and the "truth" (simulation inputs). The bias, defined as

$$\text{bias} = \langle x_A - x_B \rangle, \tag{6.10}$$

where x is the parameter of interest and A and B are the two sources of data. This quantifies any systematic error. Secondly, the root mean square error (RMSE), which is defined as

$$\text{RMSE} = \sqrt{\langle (x_A - x_B)^2 \rangle} \tag{6.11}$$

which describes the variability in measurements. These values are quoted alongside standard errors calculated according to Hughes and Hase (2010).

We assume a target with stellar separation of $\theta = 3.5$ arcseconds and magnitudes of $V = 5.7$ and $V = 6.3$, which corresponds to the average target observed by the Stereo-SCIDAR in the 2018A dataset with the separation again scaled by (1.8/0.5). All other parameters are taken from Tab. 6.1. With these parameters and target, 12 layer profiles are obtained with a maximum altitude of 23.7 km.

Shot noise is included, assuming an overall system throughput (atmospheric transmission + telescope + detector quantum efficiency) of 100%. To maintain generality for all detectors, read-out noise is also neglected. This means that these simulations represent the best possible case in terms of noise for a particular target. For each of the 18 clusters we simulate 1000 random sets of phase screens, which are averaged to produce the autocovariance. The two dimensional fitting procedure described in Fig. 6.4 is used to fit the $C_n^2(h)$ profile for each cluster.

In Fig. 6.10 we compare integrated parameters, seeing and θ_0, of the profiles obtained from the simulation to the original 20 layer input profiles. We can see that in terms of seeing, the simulated pt5m-SCIDAR agrees very well with the input profiles. There is some underestimation for very large (>1.5 arcsecond) seeing values, which is most likely the result of the saturation of scintillation in strong turbulence.

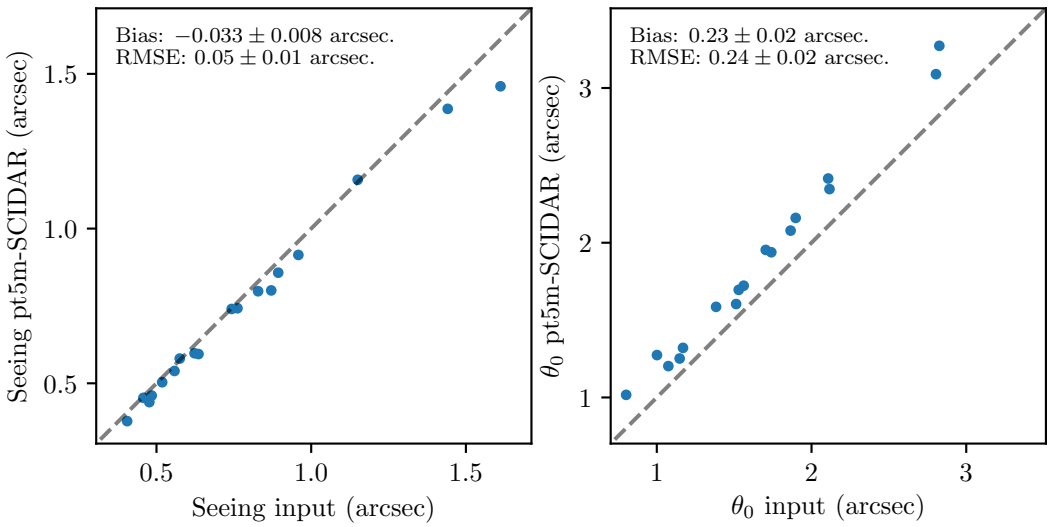

Figure 6.10: Comparison of seeing (left) and θ_0 (right) obtained from a simulation of the pt5m-SCIDAR with the 18 single cluster profiles from chapter 3.

For θ_0 there is a clear small positive bias: larger values are produced by the pt5m-SCIDAR than are being put into the simulation. This may be explained by the diffraction effects described in section 6.3.1, in particular Fig. 6.7, where we show that we expect a bias in the free atmosphere $C_n^2(h)$ of around 10%. This underestimation of the free atmosphere would lead to an overestimation of θ_0. As mentioned in section 6.3.1 this bias could be corrected by applying the inverse correction to $C_n^2(h)$ values produced by the pt5m-SCIDAR. However, since the bias is small we do not apply such a correction here.

By binning the 20 layer input clusters into the bins of the pt5m-SCIDAR, we may also compare the individual $C_n^2(h)\,\mathrm{d}h$ values for each layer. In Fig. 6.11 we can see that most layers from the input profile are correctly measured. Only at values of 10^{-14} $\mathrm{m}^{1/3}$ and lower do we begin to see a larger spread in values, as well as some layers being measured as 0. However, these layers are weak and hence do not result in a significant error for integrated parameters. The layers measured as 0 by the pt5m-SCIDAR make up around 20% of the weakest layers in the input profiles, which is consistent with our expectations from section 6.3.2 for the zero read-out noise case.

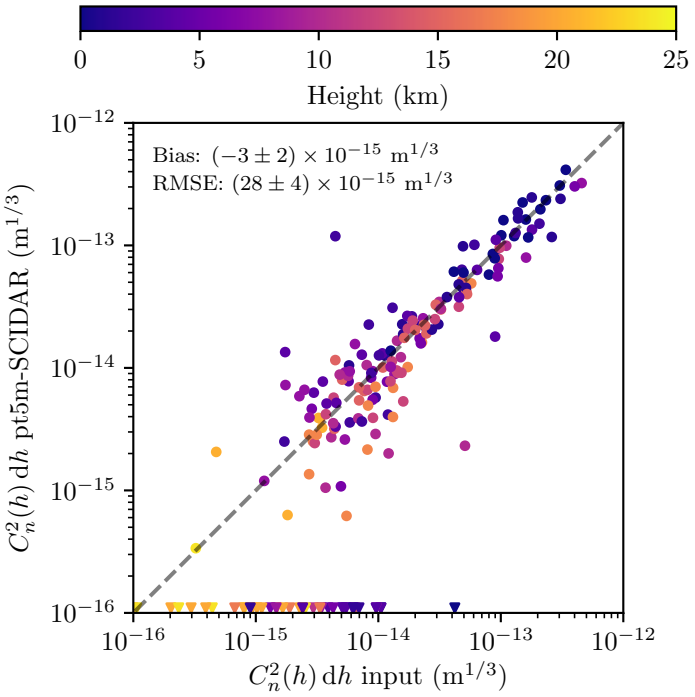

Figure 6.11: Layer-wise comparison of $C_n^2(h)\,\mathrm{d}h$ values obtained from a simulation of the pt5m-SCIDAR with the 18 single cluster profiles from chapter 3. Colour of each point indicates the height of the layer. Triangular points indicate layers where there is a $C_n^2(h)\,\mathrm{d}h > 0$ value in the input profile but a $C_n^2(h)\,\mathrm{d}h = 0$ value measured by the simulated pt5m-SCIDAR.

6.3.4 On-sky data

Despite the operation of the pt5m-SCIDAR during several short observing runs in the period 2017 - 2019, here we only present data from four nights in May and September 2019. This is primarily due to the fact that most of the measurements prior to this are taken in a configuration of the pt5m-SCIDAR with the analysis plane conjugate to only around 1 km below ground. Operating in generalised mode, this conjugation altitude is not sufficient to separate the offset ground layer peaks from the central autocovariance peak. This results in the ground layer being underestimated or in some cases not measured at all.

We also only choose nights for which we can perform a comparison with other instruments. These are the DIMM at the Telescopio Nazionale Galileo (TNG) (Gurtubai et al., 2013), measuring the seeing, and a Stereo-SCIDAR on the $D = 2.5$

Date (YYYMMDD)	Total profiles	TNG DIMM comparison	INT-SCIDAR comparison
20190519	19	18	15
20190520	54	20	35
20190918	42	42	36
20190919	53	53	23
Total	168	133	109

Table 6.2: Total number of measured profiles for each night, as well as the number of profiles valid for comparison with the TNG DIMM and INT-SCIDAR

m Isaac Newton telescope (INT) measuring full atmosphere profiles. The four nights selected allow direct comparison to these two instruments. We select from each night profiles within 5 minutes of one another to compare instruments. The numbers of profiles in each comparison are listed in Tab. 6.2. With this limited data set we may not draw any strong statistical conclusions as to the differences between instruments, however it does provide a first impression of the effectiveness of the pt5m-SCIDAR and small telescope SCIDAR in general.

We show firstly in Fig. 6.12 the comparison of seeing values with the TNG DIMM. For the pt5m-SCIDAR the seeing is calculated from the integral of $C_n^2(h)\,\mathrm{d}h$. Despite the small number of nights, we have measurements ranging from very good to very bad seeing (0.5 - 2 arcseconds). For most nights, the pt5m-SCIDAR has overestimated the seeing relative to the DIMM, as is indicated by a bias of 0.14 ± 0.04 arcseconds. However, for the night with the worst seeing according to the DIMM, the pt5m-SCIDAR measures consistently smaller seeing values.

Since the INT-SCIDAR is also measuring turbulence profiles we may draw a more thorough comparison. In Fig. 6.13 we compare both seeing and θ_0. In the comparison we consider full atmosphere profiles with a maximum altitude greater than 15 km. The seeing comparison is very similar to the TNG DIMM, with the bias and RMSE values agreeing within error. For the θ_0 comparison, we see that pt5m-SCIDAR values are usually within 1 arcsecond of the values measured by the INT-SCIDAR, with a positive bias. The night where lower seeing is measured by the

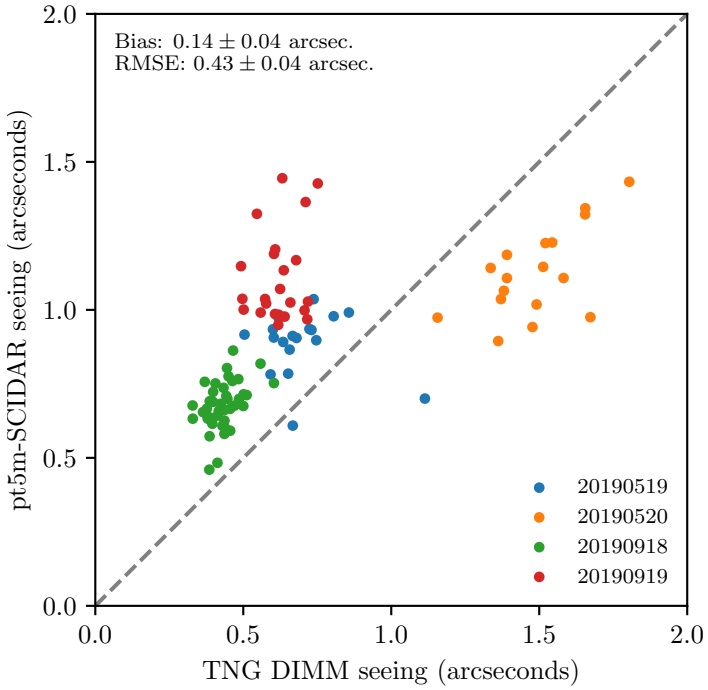

Figure 6.12: Comparison of seeing measured by the DIMM at the TNG to the values found by integrating the pt5m-SCIDAR measurements over altitude. Colours denote measurements taken on different nights.

pt5m-SCIDAR shows some large discrepancies in θ_0, with values up to 10 arcseconds where the INT is measuring only around 3 arcseconds.

We may assess the differences in the measured profiles directly by comparing $C_n^2(h)\,\mathrm{d}h$ values layer-by-layer. As for the simulations in Fig. 6.11, we bin the high resolution INT-SCIDAR profiles into the bins of the pt5m-SCIDAR.

We show the results in Fig. 6.14. It is common for the ground layer to be overestimated by the pt5m-SCIDAR by up to an order of magnitude. This is what produces the positive bias in θ_0. This ground layer discrepancy can potentially be explained as the result of different local turbulence conditions for the two instruments. The INT is a large telescope in a dedicated dome approximately 400 m away from the pt5m, which sits in a small dome on the roof of the WHT. Local disturbances from structures on this roof and the large adjacent WHT dome could produce a significant amount of turbulence which would be added to the ground. This would not be corrected by the dome correction procedure since this takes into

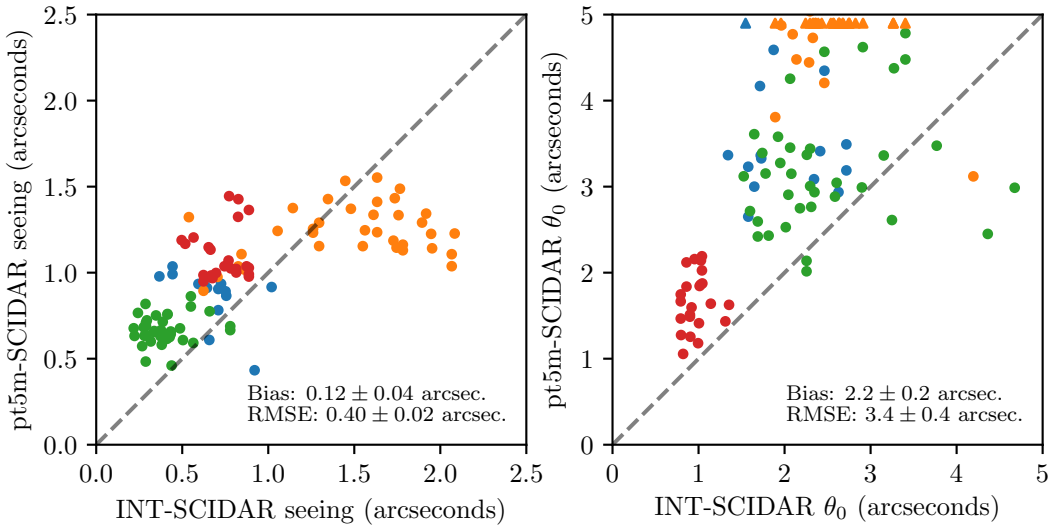

Figure 6.13: Comparison of seeing (left) and θ_0 (right) measured concurrently by the Stereo-SCIDAR on the INT and the pt5m-SCIDAR. Colours represent different nights as in Fig. 6.12. Triangular points in the right panel indicate θ_0 measurements that are in the range 5 - 10 arcseconds that are cropped out of the plot for clarity. These points are still included in the calculations of bias and RMSE.

account only static or slow-moving turbulence within the dome itself.

For the most part the free atmosphere layers are measured by the pt5m-SCIDAR are weaker than the INT-SCIDAR, which also contributes to the large positive bias in θ_0. Since the free atmosphere is not affected by local turbulence the explanation for this bias is more likely the diffraction effect as shown in Fig. 6.7.

As the measured $C_n^2(h)\,\mathrm{d}h$ values become smaller noise becomes a problem. The highest and weakest layers tend to be underestimated or measured as 0. In total, around 50% of the INT-SCIDAR layers are not measured by the pt5m-SCIDAR. This is greater than the theoretical 40% calculated in section 6.3.2, the reason for this discrepancy is most likely in our assumption of 100% throughput and constant $R_{\mathrm{pxl}} = 1e^-$, especially since CMOS detectors such as the ZWO used here are known for variable pixel to pixel read-out noise (see e.g. Basden, 2015).

Finally, in Fig 6.15 we display the sequences of profiles measured by each instrument for the four nights in question. A visual comparison shows good agreement for the

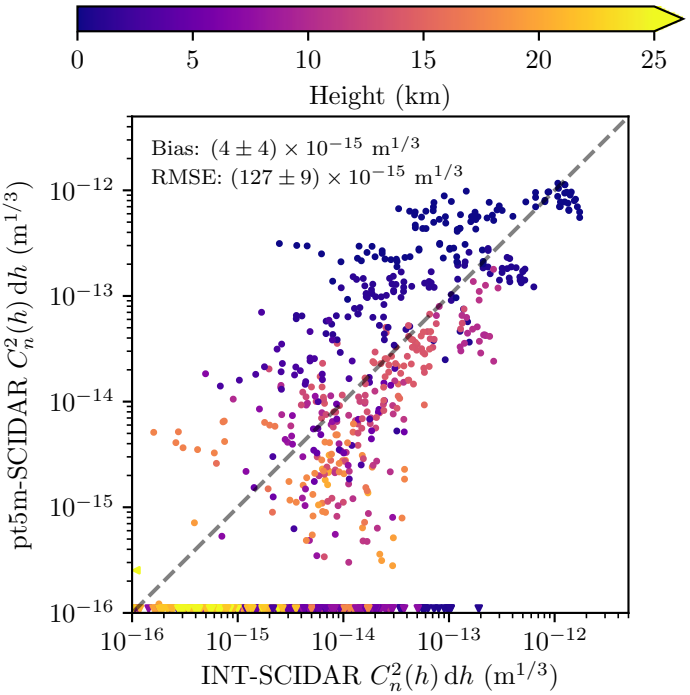

Figure 6.14: Layer-wise comparison of $C_n^2(h)\,\mathrm{d}h$ values measured concurrently by the Stereo-SCIDAR on the INT and the pt5m-SCIDAR. Layers measured as 0 by either instrument are indicated by triangular points.

most part, notwithstanding the loss in spatial and temporal resolution for the pt5m-SCIDAR. The fact that only the strongest layers are measured by the pt5m-SCIDAR is also clear.

6.4 Conclusions

We have investigated the viability of employing the SCIDAR method to measure turbulence profiles with sufficient fidelity for ELT-scale tomographic AO using a relatively small 0.5 m diameter telescope. This has been accomplished using both simulations and real data taken using the pt5m telescope in La Palma.

In simulation, we have shown that diffraction of the small pupil images, whilst having a large visual effect, does not result in a large change of the measured scintillation covariance, and can result in up to 10% underestimation of $C_n^2\,\mathrm{d}h$, depending on altitude.

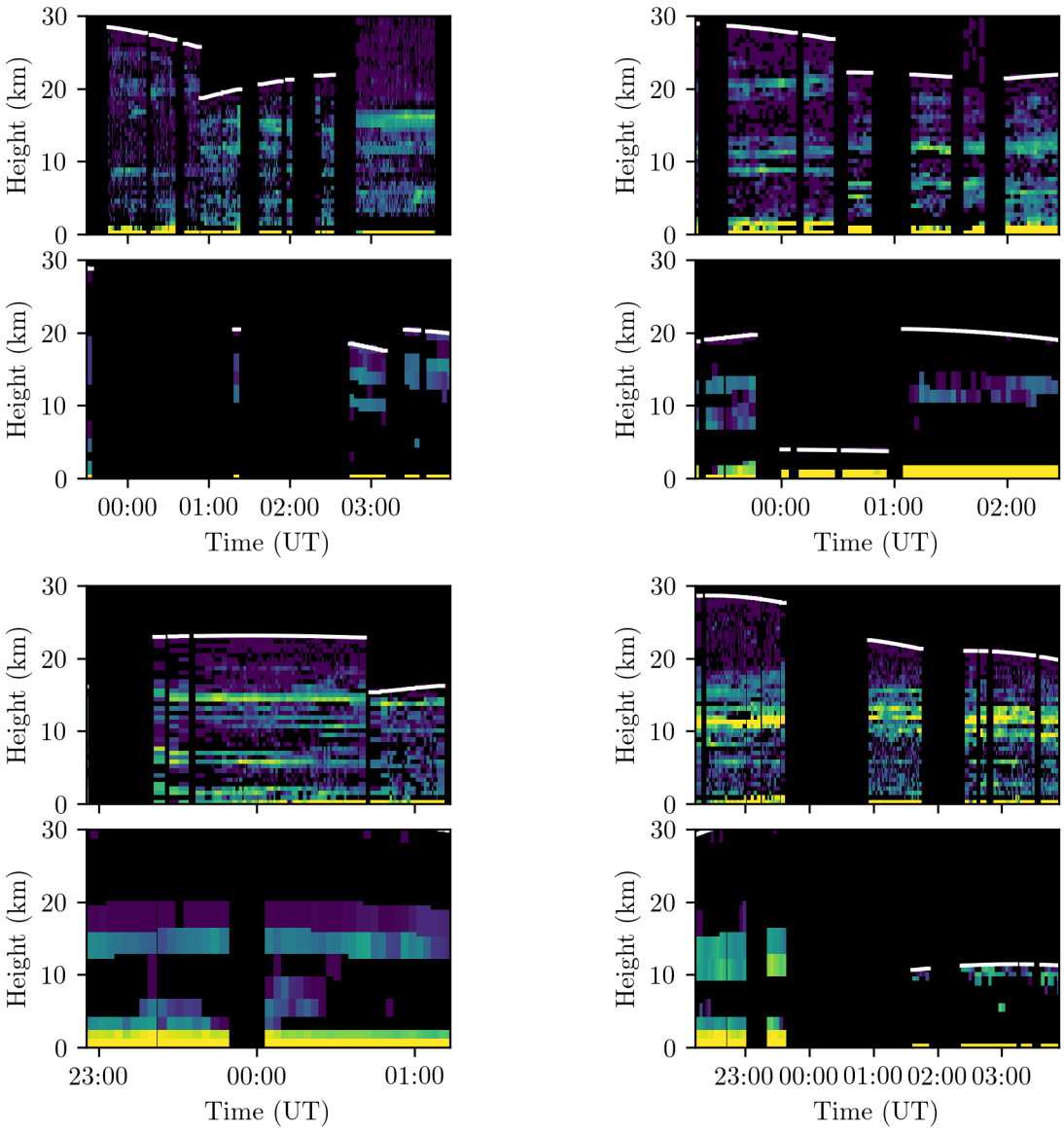

Figure 6.15: Sequences of $C_n^2(h)$ from the INT-SCIDAR (upper sub-panels) and the pt5m-SCIDAR (lower sub-panels) for the four nights used for comparison. Clockwise from upper left: 20190519, 20190520, 20190920, 20190919. White lines (where visible) indicate maximum altitude.

Using the standard theory for the sensitivity of SCIDAR and the 2018A turbulence profile dataset we have shown that at best approximately 20% of the weakest turbulent layers measured by the Stereo-SCIDAR on the AT would not be measured by the pt5m-SCIDAR. Taking into account the significant read-noise contirbutions of small pixels, this fraction increases to around 40%. However, we showed using Fourier AO simulation that even in this worst case the effect of this loss of sensitivity on the tomographic error is small.

Using full Monte Carlo simulation of the pt5m-SCIDAR we test the ability of the system to measure the 18 clustered turbulence profiles defined in chapter 3. We find that for the most part the system performs well in correctly measuring the input profiles. A small positive bias in θ_0 (0.23 ± 0.02 arcseconds) may be explained by the diffraction effect and potentially corrected in post processing. Comparing $C_n^2(h)\,\mathrm{d}h$ values shows that, in agreement with our sensitivity analysis, around 20% of the weakest layers are not measured by the pt5m-SCIDAR.

Finally, on-sky data measured on four nights in May and September 2019 was used to compare the pt5m-SCIDAR to other instruments at ORM. Seeing comparisons with both the TNG DIMM and the INT-SCIDAR showed that the seeing measured by the pt5m-SCIDAR is generally high, which could be attributed to local structures in the vicinity of the pt5m telescope causing additional turbulence. Similar behaviour is seen in comparisons with θ_0 from the INT-SCIDAR, implying that the ground layer measured by the pt5m-SCIDAR is higher. We show this explicitly by comparing $C_n^2(h)\,\mathrm{d}h$ layer-by-layer, where we find that the ground layer is often larger by an order of magnitude. This comparison also indicates that around 50% of the layers measured by the INT-SCIDAR are not measured by the pt5m-SCIDAR, slightly worse than our theoretical estimate. A fuller statistical comparison could be drawn between the pt5m-SCIDAR and the other turbulence measuring instruments with additional data, particularly including a more diverse range of turbulence profiles.

The case for obtaining large databases of relatively high resolution turbulence pro-

files has been shown in previous chapters. If they are to be representative these databases must measure profiles in as many different atmospheric conditions as possible. Currently there is no turbulence monitoring instrument that fulfills both the requirement of continuous robotic operation (e.g. MASS, DIMM, SLODAR) and high resolution turbulence profiles (e.g. Stereo/generalised-SCIDAR). We believe these preliminary results for the pt5m-SCIDAR show the potential of the concept of small telescope SCIDAR to fill this gap.

7

Conclusions

This thesis has been primarily concerned with tomographic AO, and how its performance is related to the optical turbulence profile. For both current generation and next generation ELTs, instruments fed by tomographic AO systems will enable a wealth of new observations and discoveries to be made in the field of astronomy.

The work has focussed on the 2018A Stereo-SCIDAR dataset, consisting of over 10,000 high resolution measurements of the optical turbulence profile from ESO Paranal, Chile. Through analysis of these profiles we have defined new reference profiles for E2E simulation that are more representative for a tomographic system. These were validated in simulation, where we also investigated the sensitivity of ELT-scale tomographic AO to effects such as the temporal evolution of the profile over time. Finally, we presented on-sky results from a new turbulence profiler which would allow the collection of similar large datasets with a small robotic telescope.

7.1 Defining new reference profiles

Since we are currently in the design phase of many tomographic AO systems, it is of paramount importance that the simulations used produce accurate estimates of performance. These E2E simulations are slow, and therefore only a handful

of reference profiles are used. Unlike previous non tomographic AO systems, the optical turbulence profile results in an error (tomographic error) that cannot be computed according to classical turbulence parameters r_0 and θ_0. This means that widely used reference turbulence profiles for many observing sites, which are usually defined according to these parameters, may not be representative for tomographic simulations.

In chapter 3 we presented a new method of obtaining reference turbulence profiles for E2E simulation from a large dataset. By performing a hierarchical clustering procedure we are able to sort the profiles according to their shape, rather than by integrated parameters. In this way the method produces reference profiles that are more representative of the dataset as a whole.

We applied this method to the 2018A Stereo-SCIDAR dataset. This resulted in two sets of 18 profiles that reflected the variability of the profile at Paranal in different ways. We showed that these profiles are still representative of the full dataset in terms of r_0 and θ_0, whilst also exhibiting variability in shape that is not necessarily captured by these parameters. The profiles have been made available to the AO community and have started to see use in E2E simulations.

7.2 Fourier AO simulation with real profiles

In order to assess whether reference profiles, including the clustered profiles from chapter 3, were representative for a tomographic system, we employed a fast analytical Fourier AO simulation. This allowed the computation of the tomographic error for every profile in the 2018A dataset, the distribution of which could then be compared to the values for the reference profiles.

In chapter 4 we showed that, in terms of tomographic error, many reference profiles for Paranal are not representative. Profiles designed to represent median conditions in fact overestimated the median tomographic error by up to 50%. We noted that

all of the profiles that overestimated the tomographic error were averages of many measurements of the profile.

By using examples from the 2018A dataset we showed that the averaging process, which produces smooth continuous turbulence distributions from individual profiles that have strong discrete layers, can lead directly to a higher tomographic error than expected. We therefore concluded that individual profiles selected from a large dataset should be used as reference profiles, as opposed to averages.

In chapter 5 we further employed the Fourier simulation coupled to the 2018A dataset to assess the impact of sub-optimal tomographic reconstruction for the ELT. In real tomographic systems the turbulence profile used in the reconstructor is never a perfect match for the true atmosphere. Firstly, a limited number of discrete layers are used in the tomographic reconstructor to model the profile. We showed that the number of layers required can depend strongly on the shape of the profile, in the worst cases requiring an additional 10 layers to maintain the same tomographic error.

We also examined the error incurred due to temporal evolution of the turbulence profile. We showed that the error increases for the first 20 minutes after reconstructor optimisation before plateauing. This allowed us to recommend a reconstructor update period for ELT tomographic reconstructors of less than 20 minutes. However, within these timescales the profile may still change unpredictably resulting in large increases in tomographic error. To avoid these error spikes, particularly on nights where the profile is variable, an update rate of around 5 minutes or less is required. We also proposed an alternative strategy where the reconstructor optimisation is triggered as soon as the tomographic error reaches a certain threshold. This would allow the reconstructor update rate to vary dynamically with the atmosphere, maintaining optimal tomographic reconstruction whilst minimising requirements for the SRTC system.

7.3 Collecting new large datasets

Analysis performed in chapters 3, 4 and 5 was dependent on the Stereo-SCIDAR 2018A dataset, containing over 10,000 high resolution turbulence profiles. These large datasets of high resolution profiles are rare, as instruments such as the Stereo-SCIDAR are operated on relatively large telescopes ($D \geq 2$ m) that are also used for other observations. These instruments are usually operated in campaign mode, requiring a telescope operator and measure the profile on only a fraction of nights throughout the year.

In chapter 6, we investigated the possiblity of using the SCIDAR method on a smaller $D = 0.5$ m aperture. With this aperture, the turbulence profile may be measured with sufficient fidelity for most ELT tomographic AO applications, while the telescope is small enough that it may be dedicated to full time robotic operations. This would allow the fast and cost effective gathering of turbulence profile data for a site, enabling real-time support for tomographic AO as well as long term site characterisation and monitoring. We choose $D = 0.5$ m since we were able to take on-sky data using the pt5m telescope at ORM, La Palma. This telescope is already used for robotic remote observations and therefore is a good prototype for small telescope SCIDAR.

In simulation we addressed some of the potential problems that are raised by using the SCIDAR technique on a small telescope. We will lose sensitivity to the profile, since the area of the pupil is much smaller. Using the 2018A measurements we showed that, had the pt5m telescope been used in place of the AT at Paranal, only around 20% of the weakest layers would be lost due to noise. We also showed that diffraction of the pupil has a small but measurable effect on the C_n^2 measurements that may be calibrated out if necessary. The sensitivity and diffraction effects were also observed with a full Monte-Carlo simulation of the pt5m-SCIDAR using the 18 single profile clusters from chapter 3.

Finally, we presented on sky data from the pt5m-SCIDAR taken in May and September 2019. For a limited dataset consisting of four nights, we were able to draw concurrent comparison to both the TNG DIMM and a Stereo-SCIDAR operating on the much larger INT. These comparisons showed that the pt5m-SCIDAR tended to estimate larger seeing values, and by comparing each turbulent layer with the INT-SCIDAR we showed that most of this discrepancy was in the ground layer. It is likely that this ground layer difference is due to local turbulence effects arising from structures in the vicinity of the pt5m telescope. This comparison also showed that approximately 50% of layers measured by the INT were not measured by the pt5m, implying that for the targets used the sensitivity of the pt5m-SCIDAR was lower than expected.

Further data is required to reinforce these preliminary results, however we showed that SCIDAR using a small telescope is viable both in theory and on-sky. An instrument such as the pt5m-SCIDAR has the potential to perform site characterisation for ELT-scale tomographic AO, enabling all the analysis from previous chapters, at a small fraction of the cost of larger turbulence profilers.

Bibliography

C. S. Adams and I. G. Hughes. *Optics f2f*. Oxford University Press, dec 2018. ISBN 9780198786788. doi: 10.1093/oso/9780198786788.001.0001. URL http://www.oxfordscholarship.com/view/10.1093/oso/9780198786788.001.0001/oso-9780198786788.

L. C. Andrews and R. L. Phillips. *Laser beam propagation through random media: Second edition*. SPIE, 1000 20th Street, Bellingham, WA 98227-0010 USA, sep 2005. ISBN 9780819478320. doi: 10.1117/3.626196. URL http://ebooks.spiedigitallibrary.org/book.aspx?doi=10.1117/3.626196.

C. Arcidiacono, A. Baruffolo, G. Bregoli, E. Cascone, G. Cosentino, P. Ciliegi, E. Diolaiti, M. Bellazzini, S. Esposito, I. Foppiani, L. Schreiber, P. Feautrier, G. Agapito, L. Busoni, and R. Ragazzoni. MAORY real-time computer preliminary design. In D. Schmidt, L. Schreiber, and L. M. Close, editors, *Adapt. Opt. Syst. VI*, volume 1070343, page 153. SPIE, jul 2018. ISBN 9781510619593. doi: 10.1117/12.2311618. URL https://www.spiedigitallibrary.org/conference-proceedings-of-spie/10703/2311618/MAORY-real-time-computer-preliminary-design/10.1117/12.2311618.full.

R. Avila and S. Cuevas. On the normalization of scintillation autocovariance for generalized SCIDAR. *Opt. Express*, 17(3):1483–1495, aug 2009. ISSN 00358711. doi: 10.1364/OE.17.010926. URL http://arxiv.org/abs/astro-ph/0608595http://dx.doi.org/10.1111/j.1365-2966.2006.10951.x.

R. Avila, J. Vernin, and E. Masciadri. Whole atmospheric-turbulence profiling with generalized scidar. *Appl. Opt.*, 36:7898–7905, 1997. ISSN 0003-6935. doi: 10.1364/AO.36.007898.

R. Avila, F. Ibanez, B. Sanchez, R. M. Michel, J. Vernin, F. Garfias, J. Echevarria, M. Tapia, S. I. Gonzalez, A. Agabi, F. Angeles, R. Conan, L. Parrao, O. N. Harris, W. J. Schuster, F. Martin, M. S. Sarazin, E. Carrasco, M. Azouit, I. Cruz-Gonzales, J. Borgnino, V. G. Orlov, S. Cuevas, L. A. Martinez, L. J. Sanchez, D. X. Cruz, E. Masciadri, D. Hiriart, L. Gutierrez, V. V. Voitsekhovich, R. Costero, and A. Ziad. San Pedro Mártir: astronomical site evaluation. *Second Backaskog Work. Extrem. Large Telesc.*, 5382(July 2004):634, 2005. doi: 10.1117/12.566347.

R. Avila, J. L. Avils, R. W. Wilson, M. Chun, T. Butterley, and E. Carrasco. LOLAS: an optical turbulence profiler in the atmospheric boundary layer with extreme altitude resolution. *MNRAS*, 387(4):1511–1516, jul 2008. ISSN 00358711. doi: 10.1111/j.1365-2966.2008.13386.x. URL `https://academic.oup.com/mnras/article-lookup/doi/10.1111/j.1365-2966.2008.13386.x`.

M. Azouit and J. Vernin. Remote Investigation of Tropospheric Turbulence by Two-Dimensional Analysis of Stellar Scintillation. *J. Atmos. Sci.*, 37(7): 1550–1557, jul 1980. ISSN 0022-4928. doi: 10.1175/1520-0469(1980)037<1550:RIOTTB>2.0.CO;2. URL `http://journals.ametsoc.org/doi/abs/10.1175/1520-0469{%}281980{%}29037{%}3C1550{%}3ARIOTTB{%}3E2.0.CO{%}3B2`.

H. W. Babcock. THE POSSIBILITY OF COMPENSATING ASTRONOMICAL SEEING. *Publ. Astron. Soc. Pacific*, 65(386):229–236, 1953. ISSN 00046280, 15383873. URL `http://www.jstor.org/stable/40672682`.

A. Basden. Analysis of EMCCD and sCMOS readout noise models for Shack-Hartmann wavefront sensor accuracy. pages 1–17, jun 2015. URL `http://arxiv.org/abs/1506.07929`.

A. Basden, T. Butterley, R. Myers, and R. Wilson. Durham extremely large telescope adaptive optics simulation platform. *Appl. Opt.*, 46(7):1089, mar 2007. ISSN 0003-6935. doi: 10.1364/AO.46.001089. URL `https://www.osapublishing.org/abstract.cfm?URI=ao-46-7-1089`.

J. M. Beckers. Increasing the Size of the Isoplanatic Patch with Multiconjugate Adaptive Optics. In M.-H. Ulrich, editor, *Eur. South. Obs. Conf. Work. Proc.*, volume 30, pages 693–703, 1988.

M. Benisty, A. Juhasz, A. Boccaletti, H. Avenhaus, J. Milli, C. Thalmann, C. Dominik, P. Pinilla, E. Buenzli, A. Pohl, J.-L. Beuzit, T. Birnstiel, J. de Boer, M. Bonnefoy, G. Chauvin, V. Christiaens, A. Garufi, C. Grady, T. Henning, N. Huelamo, A. Isella, M. Langlois, F. Ménard, D. Mouillet, J. Olofsson, E. Pantin, C. Pinte, and L. Pueyo. Asymmetric features in the protoplanetary disk MWC 758. *A&A*, 578:L6, jun 2015. ISSN 0004-6361. doi: 10.1051/0004-6361/201526011. URL `http://www.aanda.org/10.1051/0004-6361/201526011`.

T. Butterley, R. W. Wilson, M. Sarazin, C. M. Dubbeldam, J. Osborn, and P. Clark. Characterization of the ground layer of turbulence at Paranal using a robotic SLODAR system. *MNRAS*, 492(1):934–949, feb 2020. ISSN 0035-8711. doi: 10.1093/mnras/stz3498. URL `https://academic.oup.com/mnras/article/492/1/934/5674124`.

R. Conan and C. Correia. Object-oriented Matlab adaptive optics toolbox. In E. Marchetti, L. M. Close, and J.-P. Véran, editors, *Proc. SPIE*, volume 9148, page 91486C, aug 2014. ISBN 9780819496164. doi: 10.1117/12.2054470. URL `http://proceedings.spiedigitallibrary.org/proceeding.aspx?doi=10.1117/12.2054470`.

A. Cortés, B. Neichel, A. Guesalaga, J. Osborn, F. Rigaut, and D. Guzman. Atmospheric turbulence profiling using multiple laser star wavefront sensors. *MNRAS*, 427(3):2089–2099, dec 2012. ISSN 00358711. doi: 10.1111/j.1365-2966.2012.

22076.x. URL https://academic.oup.com/mnras/article-lookup/doi/10.1111/j.1365-2966.2012.22076.x.

W. Dali Ali, A. Ziad, A. Berdja, J. Maire, J. Borgnino, M. Sarazin, G. Lombardi, J. Navarrete, H. Vazquez Ramio, M. Reyes, J. M. Delgado, J. J. Fuensalida, A. Tokovinin, and E. Bustos. Multi-instrument measurement campaign at Paranal in 2007. *A&A*, 524:A73, 2010. ISSN 0004-6361. doi: 10.1051/0004-6361/201015178. URL http://www.aanda.org/10.1051/0004-6361/201015178.

E. Diolaiti, P. Ciliegi, R. Abicca, G. Agapito, C. Arcidiacono, A. Baruffolo, M. Bellazzini, M. Bonaglia, G. Bregoli, O. Brissaud, L. Busoni, P. Feautrier, E. Maiorano, L. Michaud, N. Auricchio, A. Balestra, I. Di Antonio, P. Grani, D. Greggio, S. Rochat, A. Carlotti, E. Cascone, J.-J. Correia, F. Cortecchia, G. Cosentino, V. D'Orazi, M. Dall'Ora, V. De Caprio, A. De Rosa, A. Delboulbe, G. Di Rico, S. Esposito, D. Fantinel, G. Fiorentino, I. Foppiani, E. Giro, L. Gluck, F. B. Hénault, L. Jocou, P. La Penna, S. Lafrasse, M. Lauria, E. P. Le Coarer, M. Le Louarn, M. Lombini, Y. Magnard, F. Mannucci, E. Marchetti, D. Maurel, G. Morgante, T. Moulin, S. Oberti, M. Patti, C. Plantet, L. Podio, A. T. Puglisi, P. Rabou, R. Ragazzoni, M. Riva, M. Aliverti, S. Rochat, F. Roussel, A. Roux, B. Salasnich, P. Saracco, L. Schreiber, M. Spavone, E. Stadler, M.-H. Sztefek, N. Ventura, C. Vérinaud, S. Zaggia, M. Dolci, D. Magrin, E. Moraux, G. Pariani, E. Redaelli, L. Terenzi, and A. Valentini. MAORY for ELT: preliminary design overview. In D. Schmidt, L. Schreiber, and L. M. Close, editors, *Adapt. Opt. Syst. VI*, volume 1070311, page 38. SPIE, jul 2018. ISBN 9781510619593. doi: 10.1117/12.2313672. URL https://www.spiedigitallibrary.org/conference-proceedings-of-spie/10703/2313672/MAORY-for-ELT-preliminary-design-overview/10.1117/12.2313672.full.

N. Doucet, D. Gratadour, H. Ltaief, R. Kriemann, E. Gendron, and D. Keyes. Scalable soft real-time supervisor for tomographic AO. In D. Schmidt, L. Schreiber,

and L. M. Close, editors, *Adapt. Opt. Syst. VI*, number July 2018, page 170. SPIE, jul 2018. ISBN 9781510619593. doi: 10.1117/12.2313273. URL https://www.spiedigitallibrary.org/conference-proceedings-of-spie/10703/2313273/Scalable-soft-real-time-supervisor-for-tomographic-AO/10.1117/12.2313273.full.

B. L. Ellerbroek. Efficient computation of minimum-variance wave-front reconstructors with sparse matrix techniques. *J. Opt. Soc. Am. A*, 19(9):1803, sep 2002. ISSN 1084-7529. doi: 10.1364/JOSAA.19.001803. URL https://www.osapublishing.org/abstract.cfm?URI=josaa-19-9-1803.

B. L. Ellerbroek and D. W. Tyler. Adaptive Optics Sky Coverage Calculations for the Gemini-North Telescope. *Publ. Astron. Soc. Pacific*, 110(744):165–185, feb 1998. ISSN 0004-6280. doi: 10.1086/316120. URL http://iopscience.iop.org/article/10.1086/316120.

S. G. Els, T. Travouillon, M. Schoeck, R. Riddle, W. Skidmore, J. Seguel, E. Bustos, and D. Walker. Thirty Meter Telescope Site Testing VI: Turbulence Profiles. *Publ. Astron. Soc. Pacific*, 121(881):787–796, apr 2009. ISSN 0004-6280. doi: 10.1086/599384. URL http://iopscience.iop.org/article/10.1086/605295http://arxiv.org/abs/0904.1865http://dx.doi.org/10.1086/599384.

S. Esposito, A. Riccardi, E. Pinna, A. T. Puglisi, F. Quirós-Pacheco, C. Arcidiacono, M. Xompero, R. Briguglio, L. Busoni, L. Fini, J. Argomedo, A. Gherardi, G. Agapito, G. Brusa, D. L. Miller, J. C. Guerra Ramon, K. Boutsia, and P. Stefanini. Natural guide star adaptive optics systems at LBT: FLAO commissioning and science operations status. In B. L. Ellerbroek, E. Marchetti, and J.-P. Véran, editors, *Adapt. Opt. Syst. III*, volume 8447, pages 84470U–84470U–11, sep 2012. ISBN 9780819491480. doi: 10.1117/12.927109. URL http://proceedings.spiedigitallibrary.org/proceeding.aspx?articleid=1358890.

S. Esposito, G. Agapito, M. Bonaglia, L. Busoni, T. Fusco, B. Neichel, P. Spano, G. Bono, and J. Vernet. AOF upgrade for VLT UT4: an 8m class HST from ground. In E. Marchetti, L. M. Close, and J.-P. Véran, editors, *Proc. SPIE*, volume 9909 of *0*, page 99093U, jul 2016. ISBN 9781510601970. doi: 10.1117/12.2234737. URL http://proceedings.spiedigitallibrary.org/proceeding.aspx?doi=10.1117/12.2234737.

B. S. Everitt, S. Landau, M. Leese, and D. Stahl. *Cluster Analysis*. John Wiley & Sons, Ltd., 5th edition, 2011. ISBN 978-0-470-74991-3.

O. J. D. Farley, J. Osborn, T. Morris, M. Sarazin, T. Butterley, M. J. Townson, P. Jia, and R. W. Wilson. Representative optical turbulence profiles for ESO Paranal by hierarchical clustering. *MNRAS*, 4037:4030–4037, sep 2018. ISSN 0035-8711. doi: 10.1093/mnras/sty2536. URL https://academic.oup.com/mnras/advance-article/doi/10.1093/mnras/sty2536/5101457.

O. J. D. Farley, J. Osborn, T. Morris, T. Fusco, B. Neichel, C. Correia, and R. W. Wilson. Identifying optical turbulence profiles for realistic tomographic error in adaptive optics. *MNRAS*, 488(1):213–221, sep 2019. ISSN 0035-8711. doi: 10.1093/mnras/stz1669. URL https://academic.oup.com/mnras/article/488/1/213/5520823.

O. J. D. Farley, J. Osborn, T. Morris, T. Fusco, B. Neichel, C. Correia, and R. W. Wilson. Limitations imposed by optical turbulence profile structure and evolution on tomographic reconstruction for the ELT. *MNRAS*, 494(2):2773–2784, may 2020. ISSN 0035-8711. doi: 10.1093/mnras/staa795. URL https://academic.oup.com/mnras/article/494/2/2773/5815102.

D. L. Fried. Limiting Resolution Looking Down Through the Atmosphere. *J. Opt. Soc. Am.*, 56(10):1380, oct 1966. ISSN 0030-3941. doi: 10.1364/JOSA.56.001380. URL https://www.osapublishing.org/abstract.cfm?URI=josa-56-10-1380.

D. L. Fried. Varieties of isoplanatism. In J. C. Wyant, editor, *Proc. SPIE*, volume 75, pages 20–29, jul 1976. doi: 10.1117/12.954733. URL `http://proceedings.spiedigitallibrary.org/proceeding.aspx?articleid=1225689`.

D. L. Fried. Anisoplanatism in adaptive optics. *J. Opt. Soc. Am.*, 72(1):52, jan 1982. ISSN 0030-3941. doi: 10.1364/JOSA.72.000052. URL `https://www.osapublishing.org/abstract.cfm?URI=josa-72-1-52`.

D. L. Fried. Time-delay-induced mean-square error in adaptive optics. *J. Opt. Soc. Am. A*, 7(7):1224, jul 1990. ISSN 1084-7529. doi: 10.1364/JOSAA.7.001224. URL `https://www.osapublishing.org/abstract.cfm?URI=josaa-7-7-1224`.

D. L. Fried. Analysis of the CLEAN algorithm and implications for superresolution. *J. Opt. Soc. Am. A*, 12(5):853, 1995. ISSN 1084-7529. doi: 10.1364/josaa.12.000853.

A. Fuchs, M. Tallon, and J. Vernin. Focusing on a Turbulent Layer: Principle of the "Generalized SCIDAR". *Publ. Astron. Soc. Pacific*, 110(743):86–91, jan 1998. ISSN 0004-6280. doi: 10.1086/316109. URL `http://iopscience.iop.org/article/10.1086/316109`.

T. Fusco and A. Costille. Impact of Cn2 profile structure on wide-field AO performance. *SPIE Astron. Telesc. Instrum.*, (July 2010):77360J—-77360J, 2010. ISSN 0277786X. doi: 10.1117/12.857489.

T. Fusco, J.-M. Conan, V. Michau, L. M. Mugnier, and G. Rousset. Phase estimation for large field of view: application to multiconjugate adaptive optics. *SPIE's Int. Symp. Opt. Sci. Eng. Instrum.*, 3763(July):125–133, 1999. ISSN 0277786X. doi: 10.1117/12.363606.

T. Fusco, J.-M. Conan, G. Rousset, L. M. Mugnier, and V. Michau. Optimal wave-front reconstruction strategies for multiconjugate adaptive optics. *J. Opt. Soc. Am. A*, 18(10):2527, oct 2001. ISSN 1084-7529. doi: 10.

1364/JOSAA.18.002527. URL https://www.osapublishing.org/abstract.cfm?URI=josaa-18-10-2527.

B. García-Lorenzo and J. J. Fuensalida. Statistical structure of the atmospheric optical turbulence at Teide Observatory from recalibrated generalized SCIDAR data. *MNRAS*, 410(2):934–945, jan 2011. ISSN 00358711. doi: 10.1111/j.1365-2966.2010.17492.x. URL https://academic.oup.com/mnras/article-lookup/doi/10.1111/j.1365-2966.2010.17492.x.

E. Gendron, C. Morel, J. Osborn, O. Martin, D. Gratadour, F. Vidal, M. Le Louarn, and G. Rousset. Robustness of tomographic reconstructors versus real atmospheric profiles in the ELT perspective. Number Dm, page 91484N, aug 2014. ISBN 9780819496164. doi: 10.1117/12.2055809. URL http://proceedings.spiedigitallibrary.org/proceeding.aspx?doi=10.1117/12.2055809.

L. Gilles and B. L. Ellerbroek. Split atmospheric tomography using laser and natural guide stars. *J. Opt. Soc. Am. A*, 25(10):2427, oct 2008. ISSN 1084-7529. doi: 10.1364/JOSAA.25.002427. URL https://www.osapublishing.org/abstract.cfm?URI=josaa-25-10-2427.

L. Gilles and B. L. Ellerbroek. Real-time turbulence profiling with a pair of laser guide star Shack–Hartmann wavefront sensors for wide-field adaptive optics systems on large to extremely large telescopes. *J. Opt. Soc. Am. A*, 27 (11):A76, nov 2010. ISSN 1084-7529. doi: 10.1364/JOSAA.27.000A76. URL https://www.osapublishing.org/abstract.cfm?URI=josaa-27-11-A76.

L. Gilles, L. Wang, and B. Ellerbroek. Wavefront error budget development for the Thirty Meter Telescope laser guide star adaptive optics system. volume 7015, page 701520, jul 2008. ISBN 9780819472250. doi: 10.1117/12.786971. URL http://proceedings.spiedigitallibrary.org/proceeding.aspx?articleid=1336681http://proceedings.spiedigitallibrary.org/proceeding.aspx?doi=10.1117/12.786971.

S. Gillessen, F. Eisenhauer, S. Trippe, T. Alexander, R. Genzel, F. Martins, and T. Ott. MONITORING STELLAR ORBITS AROUND THE MASSIVE BLACK HOLE IN THE GALACTIC CENTER. *ApJ*, 692 (2):1075–1109, feb 2009. ISSN 0004-637X. doi: 10.1088/0004-637X/692/2/1075. URL http://stacks.iop.org/0004-637X/692/i=2/a=1075?key=crossref.964d8bd98cab29742a0e1e712658e4b1.

D. Gratadour, M. Puech, C. Vérinaud, P. Kestener, M. Gray, C. Petit, J. Brulé, Y. Clénet, F. Ferreira, E. Gendron, M. Lainé, A. Sevin, G. Rousset, F. Hammer, I. Jégouzo, M. Paillous, S. Taburet, Y. Yang, J.-L. Beuzit, A. Carlotti, M. Westphal, B. Epinat, M. Ferrari, T. Gautrais, J. C. Lambert, B. Neichel, and S. Rodionov. COMPASS: an efficient, scalable and versatile numerical platform for the development of ELT AO systems. In E. Marchetti, L. M. Close, and J.-P. Véran, editors, *Adapt. Opt. Syst. IV*, volume 9148, page 91486O, aug 2014. ISBN 9780819496164. doi: 10.1117/12.2056358. URL http://proceedings.spiedigitallibrary.org/proceeding.aspx?doi=10.1117/12.2056358.

D. Gratadour, J. Osborn, H. Deneux, R. Biasi, D. Perret, A. Sevin, T. J. Morris, E. J. Younger, C. Rouaud, J.-T. M. Buey, D. Pretet, J. Lemaitre, P. Palazzari, C. Patauner, M. J. Townson, D. Geng, L. Staykov, A. G. Basden, D. Pescoller, M. Andrighettoni, J. Bernard, M. Lainé, F. Ferreira, and N. Doucet. Prototyping AO RTC using emerging high performance computing technologies with the Green Flash project. In D. Schmidt, L. Schreiber, and L. M. Close, editors, *Adapt. Opt. Syst. VI*, volume 1070318, page 45. SPIE, jul 2018. ISBN 9781510619593. doi: 10.1117/12.2312686. URL https://www.spiedigitallibrary.org/conference-proceedings-of-spie/10703/2312686/Prototyping-AO-RTC-using-emerging-high-performance-computing-technologies-with/10.1117/12.2312686.full.

A. G. Gurtubai, A. della Valle, E. Molinari, S. Ortolani, J. S. Juan, A. F. Fioren-

zano, and V. Zitelli. TNG DIMM working on Roque de los Muchachos. *MNRAS*, 429(1):506–515, 2013. ISSN 00358711. doi: 10.1093/mnras/sts354.

J. W. Hardy. *Adaptive Optics for Astronomical Telescopes*. Oxford University Press, 1998. doi: 10.1063/1.883053.

L. K. Hardy, T. Butterley, V. S. Dhillon, S. P. Littlefair, and R. W. Wilson. pt5m – a 0.5 m robotic telescope on La Palma. *MNRAS*, 454(4):4316–4325, dec 2015. ISSN 0035-8711. doi: 10.1093/mnras/stv2279. URL `https://academic.oup.com/mnras/article-lookup/doi/10.1093/mnras/stv2279`.

J. A. Hartigan. *Clustering Algorithms*. John Wiley & Sons, Inc., 1975. ISBN 0-471-35645-X.

D. L. Hartmann. Chapter 6 - atmospheric general circulation and climate. In D. L. Hartmann, editor, *Global Physical Climatology (Second Edition)*, pages 159 – 193. Elsevier, Boston, second edition edition, 2016. ISBN 978-0-12-328531-7. doi: https://doi.org/10.1016/B978-0-12-328531-7.00006-2. URL `http://www.sciencedirect.com/science/article/pii/B9780123285317000062`.

G. Herriot, D. Andersen, J. Atwood, C. Boyer, P. Byrnes, K. Caputa, B. Ellerbroek, L. Gilles, A. Hill, Z. Ljusic, J. Pazder, M. Rosensteiner, M. Smith, P. Spano, K. Szeto, J.-P. Véran, I. Wevers, L. Wang, and R. Wooff. NFIRAOS: first facility AO system for the Thirty Meter Telescope. In E. Marchetti, L. M. Close, and J.-P. Véran, editors, *Proc. SPIE*, volume 9148, page 914810, jul 2014. ISBN 9780819496164. doi: 10.1117/12.2055525. URL `http://proceedings.spiedigitallibrary.org/proceeding.aspx?doi=10.1117/12.2055525`.

E. Hubble. A relation between distance and radial velocity among extra-galactic nebulae. *Proc. Natl. Acad. Sci.*, 15(3):168–173, mar 1929. ISSN 0027-8424. doi: 10.1073/pnas.15.3.168. URL `http://www.pnas.org/cgi/doi/10.1073/pnas.15.3.168`.

I. G. Hughes and T. P. A. Hase. *Measurements and their Uncertainties*. Oxford University Press, 2010.

D. R. Jenkins, A. Basden, and R. M. Myers. ELT-scale adaptive optics real-time control with the Intel Xeon Phi Many Integrated Core Architecture. *MNRAS*, 478(3):3149–3158, aug 2018. ISSN 0035-8711. doi: 10.1093/mnras/sty1310. URL `https://academic.oup.com/mnras/article/478/3/3149/4999636`.

L. Jolissaint, J.-P. Véran, and R. Conan. Analytical modeling of adaptive optics: foundations of the phase spatial power spectrum approach. *J. Opt. Soc. Am. A*, 23(2):382, feb 2006. ISSN 1084-7529. doi: 10.1364/JOSAA.23.000382. URL `https://www.osapublishing.org/abstract.cfm?URI=josaa-23-2-382`.

N. Jovanovic, O. Guyon, J. Lozi, T. Currie, J. Hagelberg, B. Norris, G. Singh, P. Pathak, D. Doughty, S. Goebel, J. Males, J. Kuhn, E. Serabyn, P. Tuthill, G. Schworer, F. Martinache, T. Kudo, H. Kawahara, T. Kotani, M. Ireland, T. Feger, A. Rains, J. Bento, C. Schwab, D. Coutts, N. Cvetojevic, S. Gross, A. Arriola, T. Lagadec, J. Kasdin, T. Groff, B. Mazin, Y. Minowa, N. Takato, M. Tamura, H. Takami, and M. Hayashi. The SCExAO high contrast imager: transitioning from commissioning to science. In E. Marchetti, L. M. Close, and J.-P. Véran, editors, *Adapt. Opt. Syst. V*, volume 9909, page 99090W, jul 2016. ISBN 9781510601970. doi: 10.1117/12.2234294. URL `http://proceedings.spiedigitallibrary.org/proceeding.aspx?doi=10.1117/12.2234294`.

L. Kaufman and P. J. Rousseeuw. *Finding Groups in Data: An Introduction to Cluster Analysis*. John Wiley & Sons, Inc., 2005. ISBN 0-47 1-73578-7.

A. N. Kolmogorov. The local structure of turbulence in incompressible viscous fluid for very large Reynolds numberst. *Proc. R. Soc.*, 434(1890):9–13, 1991. ISSN 13645021. doi: 10.1098/rspa.1991.0075. URL `http://rspa.royalsocietypublishing.org/cgi/doi/10.1098/rspa.1991.0075`.

V. Kornilov. Angular correlation of the stellar scintillation on large telescopes. *MNRAS*, 417(2):1105–1113, jun 2012. ISSN 00358711. doi: 10.1111/j.1365-2966.2011.19329.x. URL http://arxiv.org/abs/1206.2545http://dx.doi.org/10.1111/j.1365-2966.2011.19329.xhttp://mnras.oxfordjournals.org/cgi/doi/10.1111/j.1365-2966.2011.19329.x.

V. Kornilov, A. A. Tokovinin, O. Vozyakova, A. Zaitsev, N. Shatsky, S. F. Potanin, and M. S. Sarazin. MASS: a monitor of the vertical turbulence distribution. *Proc. SPIE*, 4839:837–845, 2003. ISSN 0277786X. doi: 10.1117/12.457982. URL http://proceedings.spiedigitallibrary.org/proceeding.aspx?articleid=873652.

D. J. Laidlaw, J. Osborn, T. J. Morris, A. G. Basden, O. Beltramo-Martin, T. Butterley, E. Gendron, A. P. Reeves, G. Rousset, M. J. Townson, and R. W. Wilson. Optimizing the accuracy and efficiency of optical turbulence profiling using adaptive optics telemetry for extremely large telescopes. *MNRAS*, 483 (4):4341–4353, mar 2019. ISSN 0035-8711. doi: 10.1093/mnras/sty3285. URL https://academic.oup.com/mnras/article/483/4/4341/5228754.

M. Le Louarn, C. Verinaud, V. Korkiakoski, and E. Fedrigo. Parallel simulation tools for AO on ELTs. In *Adv. Adapt. Opt.*, volume 5490, page 705, oct 2004. doi: 10.1117/12.551088. URL http://proceedings.spiedigitallibrary.org/proceeding.aspx?doi=10.1117/12.551088.

O. Martin, É. Gendron, G. Rousset, and F. Vidal. Temporal convergence of phase spatial covariance matrix measurements in tomographic adaptive optics. In B. L. Ellerbroek, E. Marchetti, and J.-P. Véran, editors, *Adapt. Opt. Syst. III*, volume 8447, pages 84472A–84472A–14, sep 2012. ISBN 9780819491480. doi: 10.1117/12.924845. URL http://proceedings.spiedigitallibrary.org/proceeding.aspx?articleid=1358937.

O. A. Martin, É. Gendron, G. Rousset, D. Gratadour, F. Vidal, T. J. Morris, A. G. Basden, R. M. Myers, C. M. Correia, and D. Henry. Wave-front error breakdown

in laser guide star multi-object adaptive optics validated on-sky by Canary. *A&A*, 598:A37, feb 2017. ISSN 0004-6361. doi: 10.1051/0004-6361/201629271. URL http://www.aanda.org/10.1051/0004-6361/201629271.

T. Morris, A. Basden, T. Buey, F. Chemla, J.-M. Conan, E. Fitzsimons, T. Fusco, E. Gendron, F. Hammer, P. Jagourel, C. Morel, R. Myers, B. Neichel, C. Petit, M. Rodrigues, and G. Rousset. Adaptive optics for MOSAIC: design and performance of the wide(st)-field AO system for the E-ELT. In E. Marchetti, L. M. Close, and J.-P. Véran, editors, *Adapt. Opt. Syst. V*, volume 9909, page 99091I, jul 2016. ISBN 9781510601970. doi: 10.1117/12.2232411. URL http://proceedings.spiedigitallibrary.org/proceeding.aspx?doi=10.1117/12.2232411.

D. Müllner. Modern hierarchical, agglomerative clustering algorithms. *ArXiv e-prints*, sep 2011. URL http://arxiv.org/abs/1109.2378.

B. Neichel, T. Fusco, and J.-M. Conan. Tomographic reconstruction for wide-field adaptive optics systems: Fourier domain analysis and fundamental limitations. *J. Opt. Soc. Am. A*, 26(1):219, jan 2009. ISSN 1084-7529. doi: 10.1364/JOSAA.26.000219. URL http://arxiv.org/abs/0811.2369{%}0Ahttp://dx.doi.org/10.1364/JOSAA.26.000219http://arxiv.org/abs/0811.2369http://dx.doi.org/10.1364/JOSAA.26.000219https://www.osapublishing.org/abstract.cfm?URI=josaa-26-1-219.

B. Neichel, F. Rigaut, F. Vidal, M. A. van Dam, V. Garrel, E. R. Carrasco, P. Pessev, C. Winge, M. Boccas, C. D'Orgeville, G. Arriagada, A. Serio, V. Fesquet, W. N. Rambold, J. Lührs, C. Moreno, G. Gausachs, R. L. Galvez, V. Montes, T. B. Vucina, E. Marin, C. Urrutia, A. Lopez, S. J. Diggs, C. Marchant, A. W. Ebbers, C. Trujillo, M. Bec, G. Trancho, P. McGregor, P. J. Young, F. Colazo, and M. L. Edwards. Gemini multiconjugate adaptive optics system review – II. Commissioning, operation and overall performance. *MNRAS*, 440(2):1002–1019, may 2014. ISSN 0035-8711. doi:

10.1093/mnras/stu403. URL http://arxiv.org/abs/1402.6906http://dx.doi.org/10.1093/mnras/stu403http://academic.oup.com/mnras/article/440/2/1002/1032104/Gemini-multiconjugate-adaptive-optics-system.

B. Neichel, T. Fusco, J.-F. Sauvage, C. Correia, K. Dohlen, K. El-Hadi, L. Blanco, N. Schwartz, F. Clarke, N. A. Thatte, M. Tecza, J. Paufique, J. Vernet, M. Le Louarn, P. Hammersley, J.-L. Gach, S. Pascal, P. Vola, C. Petit, J.-M. Conan, A. Carlotti, C. Vérinaud, H. Schnetler, I. Bryson, T. Morris, R. Myers, E. Hugot, A. M. Gallie, and D. M. Henry. The adaptive optics modes for HARMONI: from Classical to Laser Assisted Tomographic AO. volume 990909, page 990909, jul 2016. ISBN 9781510601970. doi: 10.1117/12.2231681. URL http://proceedings.spiedigitallibrary.org/proceeding.aspx?doi=10.1117/12.2231681.

I. Newton. *Opticks, or a treatise of the reflections, refractions, inflections and colours of light*. William Innys, 1730. URL http://books.google.com/books?id=XXu4AkRVBBoC.

R. J. Noll. Zernike polynomials and atmospheric turbulence*. *J. Opt. Soc. Am.*, 66 (3):207, mar 1976. ISSN 0030-3941. doi: 10.1364/JOSA.66.000207. URL https://www.osapublishing.org/abstract.cfm?URI=josa-66-3-207{%}5Cnhttp://www.osapublishing.org/viewmedia.cfm?uri=josa-66-3-207{&}seq=0{&}html=true{%}5Cnhttps://www.osapublishing.org/josa/abstract.cfm?uri=josa-66-3-207https://www.osapublishing.org/abstract.cfm?UR.

J. Osborn, R. W. Wilson, M. Sarazin, T. Butterley, A. Chacón, F. Derie, O. J. D. Farley, X. Haubois, D. Laidlaw, M. LeLouarn, E. Masciadri, J. Milli, J. Navarrete, and M. J. Townson. Optical turbulence profiling with Stereo-SCIDAR for VLT and ELT. *MNRAS*, 478(1):825–834, jul 2018. ISSN 0035-8711. doi: 10.1093/mnras/sty1070. URL https://academic.oup.com/mnras/article/478/1/825/4987879.

J. Prieur, R. Avila, G. Daigne, and J. Vernin. Automatic Determination of Wind Profiles with Generalized SCIDAR. *Pasp*, 116(Umr 5572):778–789, 2004. ISSN 00046280. doi: 10.1086/423161.

J.-L. Prieur, G. Daigne, and R. Avila. SCIDAR measurements at Pic du Midi. *A&A*, 371(1):366–377, may 2001. ISSN 0004-6361. doi: 10.1051/0004-6361:20010279. URL `http://arxiv.org/abs/0901.0974http://dx.doi.org/10.1051/0004-6361:200811415http://www.aanda.org/10.1051/0004-6361:20010279http://www.ncbi.nlm.nih.gov/pubmed/9010224`.

R. Racine and B. L. Ellerbroek. <title>Profiles of nighttime turbulence above Mauna Kea and isoplanatism extension in adaptive optics</title>. In R. K. Tyson and R. Q. Fugate, editors, *Adapt. Opt. Syst. Appl.*, volume 2534, pages 248–257, aug 1995. doi: 10.1117/12.217743. URL `http://proceedings.spiedigitallibrary.org/proceeding.aspx?articleid=1004971`.

R. Ragazzoni. Pupil plane wavefront sensing with an oscillating prism. *J. Mod. Opt.*, 43(2):289–293, feb 1996. ISSN 0950-0340. doi: 10.1080/09500349608232742. URL `http://www.tandfonline.com/doi/abs/10.1080/09500349608232742`.

A. Reeves. Soapy: an adaptive optics simulation written purely in Python for rapid concept development. In E. Marchetti, L. M. Close, and J.-P. Véran, editors, *Proc. SPIE*, volume 9909, page 99097F, jul 2016. ISBN 9781510601970. doi: 10.1117/12.2232438. URL `http://proceedings.spiedigitallibrary.org/proceeding.aspx?doi=10.1117/12.2232438`.

F. Rigaut. Ground-Conjugate Wide Field Adaptive Optics for the {ELT}s. In *Eur. South. Obs. Astrophys. Symp.*, volume 58, page 11, 2002. ISBN 3923524617.

F. Rigaut and B. Neichel. Multiconjugate Adaptive Optics for Astronomy. *Annu. Rev. Astron. Astrophys.*, 56(1):277–314, sep 2018. ISSN 0066-4146. doi: 10.

1146/annurev-astro-091916-055320. URL https://www.annualreviews.org/doi/10.1146/annurev-astro-091916-055320.

F. Rigaut and M. van Dam. Simulating Astronomical Adaptive Optics Systems Using Yao. *AO4ELT3*, (May):26–31, 2013. doi: 10.12839/AO4ELT3.13173.

F. Rigaut, J.-P. Veran, and O. Lai. An analytical model for Shack-Hartmann-based adaptive optics systems. *Proc. SPIE*, 3353(September 1998):1038, 1998. ISSN 0277786X. doi: 10.1117/12.321649.

F. J. Rigaut, B. L. Ellerbroek, and R. Flicker. Principles, Limitations and Performance of Multi-Conjugate Adaptive Optics. In P. L. Wizinowich, editor, *Proc. SPIE*, number 4007, pages 1022–1031, jul 2000. doi: 10.1117/12.390311. URL http://proceedings.spiedigitallibrary.org/proceeding.aspx?articleid=898858.

F. Roddier. V The Effects of Atmospheric Turbulence in Optical Astronomy. In *Prog. Opt.*, volume 19, pages 281–376. 1981. ISBN 9780444854445. doi: 10.1016/S0079-6638(08)70204-X. URL http://linkinghub.elsevier.com/retrieve/pii/S007966380870204X.

T. S. Ross. Limitations and applicability of the Maréchal approximation. *Appl. Opt.*, 48(10):1812, apr 2009. ISSN 0003-6935. doi: 10.1364/AO.48.001812. URL https://www.osapublishing.org/abstract.cfm?URI=ao-48-10-1812.

G. Rousset, J. Fontanella, P. Kern, P. Gigan, and F. Rigaut. First diffraction-limited astronomical images with adaptive optics. *A&A*, 230(2):L29–L32, apr 1990.

M. Sarazin and F. Roddier. The ESO differential image motion monitor. *A&A*, 227:294–300, 1990. ISSN 0004-6361. URL http://adsabs.harvard.edu/full/1990A{&}A...227..294S.

M. Sarazin, M. L. Louarn, J. Ascenso, G. Lombardi, and J. Navarrete. Defining Reference Turbulence Profiles for E-Elt Ao Performance Simulations. In *AO4ELT3*, number May, 2013. ISBN 9788890887604. doi: 10.12839/AO4ELT3.13383.

M. S. Sarazin, J. Osborn, J. Navarrete, J. Milli, M. Le Louarn, F. J. Dérie, R. W. Wilson, and A. Chacon. Preliminary results from the Stereo-SCIDAR at the VLT Observatory: extraction of reference atmospheric turbulence profiles for E-ELT adaptive optics instrument performance simulations. In K. U. Stein and S. Gladysz, editors, *Proc. SPIE*, volume 10425, pages 104250B–10. SPIE, sep 2017. ISBN 9781510613140. doi: 10.1117/12.2279675. URL `https://www.spiedigitallibrary.org/conference-proceedings-of-spie/10425/2279675/Preliminary-results-from-the-Stereo-SCIDAR-at-the-VLT-Observatory/10.1117/12.2279675.full`.

D. Saxenhuber, G. Auzinger, M. L. Louarn, and T. Helin. Comparison of methods for the reduction of reconstructed layers in atmospheric tomography. *Appl. Opt.*, 56(10):2621, 2017. ISSN 0003-6935. doi: 10.1364/AO.56.002621. URL `https://www.osapublishing.org/abstract.cfm?URI=ao-56-10-2621`.

J. D. Schmidt. *Numerical Simulation of Optical Wave Propagation with Examples in MATLAB*. SPIE, 1000 20th Street, Bellingham, WA 98227-0010 USA, jul 2010. ISBN 9780819483263. doi: 10.1117/3.866274. URL `http://www.amazon.com/Numerical-Simulation-Propagation-Examples-Monograph/dp/0819483265http://ebooks.spiedigitallibrary.org/book.aspx?doi=10.1117/3.866274`.

M. Schöck, S. Els, R. Riddle, W. Skidmore, T. Travouillon, R. Blum, E. Bustos, G. Chanan, S. G. Djorgovski, P. Gillett, B. Gregory, J. Nelson, A. Otárola, J. Seguel, J. Vasquez, A. Walker, D. Walker, and L. Wang. Thirty Meter Telescope Site Testing I: Overview. *Publ. Astron. Soc. Pacific*, 121(878):384–395, apr

2009. ISSN 0004-6280. doi: 10.1086/599287. URL http://iopscience.iop.org/article/10.1086/599287.

H. W. Shepherd, J. Osborn, R. W. Wilson, T. Butterley, R. Avila, V. S. Dhillon, and T. J. Morris. Stereo-SCIDAR: optical turbulence profiling with high sensitivity using a modified SCIDAR instrument. *MNRAS*, 437(4):3568–3577, feb 2014. ISSN 0035-8711. doi: 10.1093/mnras/stt2150. URL https://academic.oup.com/mnras/article-lookup/doi/10.1093/mnras/stt2150.

G. Sidorov, A. Gelbukh, H. Gómez-Adorno, and D. Pinto. Soft Similarity and Soft Cosine Measure: Similarity of Features in Vector Space Model. *Comput. y Sist.*, 18(3):491–504, sep 2014. ISSN 1405-5546. doi: 10.13053/cys-18-3-2043. URL http://cys.cic.ipn.mx/ojs/index.php/CyS/article/view/2043.

W. Skidmore, I. Dell'Antonio, M. Fukugawa, A. Goswami, L. Hao, D. Jewitt, G. Laughlin, C. Steidel, P. Hickson, L. Simard, M. Schöck, T. Treu, J. Cohen, G. C. Anupama, M. Dickinson, F. Harrison, T. Kodama, J. R. Lu, B. Macintosh, M. Malkan, S. Mao, N. Narita, T. Sekiguchi, A. Subramaniam, M. Tanaka, F. Tian, M. A'Hearn, M. Akiyama, B. Ali, W. Aoki, M. Bagchi, A. Barth, V. Bhalerao, M. Bradac, J. Bullock, A. J. Burgasser, S. Chapman, R.-R. Chary, M. Chiba, M. Cooper, A. Cooray, I. Crossfield, T. Currie, M. Das, G. C. Dewangan, R. de Grijs, T. Do, S. Dong, J. Evslin, T. Fang, X. Fang, C. Fassnacht, L. Fletcher, E. Gaidos, R. Gal, A. Ghez, M. Giavalisco, C. A. Grady, T. Greathouse, R. Gogoi, P. Guhathakurta, L. Ho, P. Hasan, G. J. Herczeg, M. Honda, M. Imanishi, H. Inami, M. Iye, J. Kalirai, U. S. Kamath, S. Kane, N. Kashikawa, M. Kasliwal, V. Kasliwal, E. Kirby, Q. M. Konopacky, S. Lepine, D. Li, J. Li, J. Liu, M. C. Liu, E. Lopez-Rodriguez, J. Lotz, P. Lubin, L. Macri, K. Maeda, F. Marchis, C. Marois, A. Marscher, C. Martin, T. Matsuo, C. Max, A. McConnachie, S. McGough, C. Melis, L. Meyer, M. Mumma, T. Muto, T. Nagao, J. R. Najita, J. Navarro, M. Pierce, J. X. Prochaska, M. Oguri, D. K. Ojha, Y. K. Okamoto, G. Orton, A. Otarola, M. Ouchi, C. Packham, D. L. Padgett,

S. B. Pandey, C. Pilachowsky, K. M. Pontoppidan, J. Primack, S. Puthiyaveettil, E. Ramirez-Ruiz, N. Reddy, M. Rich, M. J. Richter, J. Schombert, A. A. Sen, J. Shi, K. Sheth, R. Srianand, J. C. Tan, M. Tanaka, A. Tanner, N. Tominaga, D. Tytler, V. U, L. Wang, X. Wang, Y. Wang, G. Wilson, S. Wright, C. Wu, X. Wu, R. Xu, T. Yamada, B. Yang, G. Zhao, and H. Zhao. Thirty Meter Telescope Detailed Science Case: 2015. *Res. Astron. Astrophys.*, 14(1):433–455, may 2015. ISSN 16744527. doi: 10.1088/1674-4527/15/12/001. URL `http://arxiv.org/abs/1505.01195http://dx.doi.org/10.1088/1674-4527/15/12/001`.

V. I. Tatarski. *Wave Propagation in a Turbulent Medium.* McGraw-Hill Book Company, Inc., 1961. ISBN 9780486135168.

G. I. Taylor. The spectrum of turbulence. *Proc. R. Soc. London. Ser. A-Mathematical Phys. Sci.*, 164(919):476–490, 1938.

A. Tokovinin. Measurement of seeing and the atmospheric time constant by differential scintillations. *Appl. Opt.*, 41(6):957, feb 2002. ISSN 0003-6935. doi: 10.1364/AO.41.000957. URL `https://www.osapublishing.org/abstract.cfm?URI=ao-41-6-957`.

A. Tokovinin and E. Viard. Limiting precision of tomographic phase estimation. *J. Opt. Soc. Am. A*, 18(4):873, apr 2001. ISSN 1084-7529. doi: 10.1364/JOSAA.18.000873. URL `https://www.osapublishing.org/abstract.cfm?URI=josaa-18-4-873`.

G. Trancho, B. Espeland, A. Bouchez, R. Conan, P. Hinz, and M. van Dam. GMT AO system requirements and error budgets in the preliminary design phase. In B. L. Ellerbroek, E. Marchetti, and J.-P. Véran, editors, *Adapt. Opt. Syst. III*, volume 8447, pages 84475G–84475G–17, sep 2012. ISBN 9780819491480. doi: 10.1117/12.925245. URL `http://proceedings.spiedigitallibrary.org/proceeding.aspx?articleid=1359035`.

G. T. van Belle, A. B. Meinel, and M. P. Meinel. The scaling relationship between telescope cost and aperture size for very large telescopes. In J. M. Oschmann, Jr., editor, *Ground-based Telesc.*, volume 5489, page 563, sep 2004. doi: 10.1117/12.552181. URL `http://proceedings.spiedigitallibrary.org/proceeding.aspx?doi=10.1117/12.552181`.

E. Vernet, M. Cayrel, N. Hubin, M. Mueller, R. Biasi, D. Gallieni, and M. Tintori. Specifications and design of the E-ELT M4 adaptive unit. In B. L. Ellerbroek, E. Marchetti, and J.-P. Véran, editors, *Adapt. Opt. Syst. III*, volume 8447, pages 844761–844761–8, sep 2012. ISBN 9780819491480. doi: 10.1117/12.925133. URL `http://proceedings.spiedigitallibrary.org/proceeding.aspx?articleid=1359054`.

J. Vernin and C. Munoz-Tunon. Optical seeing at La Palma Observatory. 2: Intensive site testing campaign at the Nordic Optical Telescope. *A&A*, 284:311–318, 1994. URL `http://adsabs.harvard.edu/abs/1994A{&}A...284..311V`.

J. Vernin and F. Roddier. Experimental Determination of Two-Dimensional Spatiotemporal Power Spectra of Stellar Light Scintillaton. Evidence for a Multilayer Structure of the Air Turbulence in the Upper Troposphere. *J Opt Soc Am*, 63 (3):270–273, 1973. ISSN 0030-3941. doi: 10.1364/josa.63.000270.

J. Vernin, C. Muñoz-Tuñón, M. Sarazin, H. Vazquez Ramió, A. M. Varela, H. Trinquet, J. Miguel Delgado, J. Jiménez Fuensalida, M. Reyes, A. Benhida, Z. Benkhaldoun, D. García Lambas, Y. Hach, M. Lazrek, G. Lombardi, J. Navarrete, P. Recabarren, V. Renzi, M. Sabil, and R. Vrech. European Extremely Large Telescope Site Characterization I: Overview. *Publ. Astron. Soc. Pacific*, 123(909):1334–1346, nov 2011. ISSN 00046280. doi: 10.1086/662995. URL `http://iopscience.iop.org/article/10.1086/662995`.

F. Vidal, E. Gendron, and G. Rousset. Tomography approach for multi-object adaptive optics. *J. Opt. Soc. Am. A*, 27(11):A253, nov 2010. ISSN 1084-

7529. doi: 10.1364/JOSAA.27.00A253. URL https://www.osapublishing.org/abstract.cfm?URI=josaa-27-11-A253.

R. W. Wilson. SLODAR: measuring optical turbulence altitude with a Shack-Hartmann wavefront sensor. *MNRAS*, 337(1):103–108, nov 2002. ISSN 00358711. doi: 10.1046/j.1365-8711.2002.05847.x. URL https://academic.oup.com/mnras/article-lookup/doi/10.1046/j.1365-8711.2002.05847.x.

A. Ziad, R. Conan, A. Tokovinin, F. Martin, and J. Borgnino. From the grating scale monitor to the generalized seeing monitor. *Appl. Opt.*, 39(30): 5415, oct 2000. ISSN 0003-6935. doi: 10.1364/AO.39.005415. URL https://www.osapublishing.org/abstract.cfm?URI=ao-39-30-5415.

A. Ziad, M. Schöck, G. A. Chanan, M. Troy, R. Dekany, B. F. Lane, J. Borgnino, and F. Martin. Comparison of measurements of the outer scale of turbulence by three different techniques. *Appl. Opt.*, 43(11):2316–2324, 2004. ISSN 15394522. doi: 10.1364/AO.43.002316.

Colophon

This thesis is based on a template developed by Matthew Townson and Andrew Reeves. It was typeset with LaTeX 2_ε. It was created using the *memoir* package, maintained by Lars Madsen, with the *veelo* chapter style. The font used is Latin Modern, derived from fonts designed by Donald E. Kunith.